



The  
University  
Of  
Sheffield.

## **Exciton-Polaritons in BODIPY-filled Microcavities**

**By:**

**Kyriacos Georgiou**

A thesis submitted in partial fulfilment of the requirements for the degree of  
Doctor of Philosophy

The University of Sheffield  
Faculty of Science  
Department of Physics and Astronomy

Supervised by Professor David G. Lidzey

October 2018



*Dedicated to my family*



## Acknowledgements

Over the past 4 years I have had the pleasure of working in a group with many amazing people, without whom I could not have finished this thesis or had a great time doing so.

Firstly, I would like to thank my family for supporting all my decisions and being there for me all this time.

A big thanks to the people in the group whom I shared an office with: Rahul Jayaprakash, Dave Coles, Andrew Musser, Harriet Coulthard, Onkar Game, Naoum Vaenas and Kirsty McGhee. I was also lucky to spend time with the rest of the group members: Yiwei, Theo, Mike, Ben, Tom, James, Joel, Claire and other newer members, making my time in Sheffield really fun. I would like to thank Jass and Pepe from the theory group for the endless coffee breaks we had together in Hicks and for being such amazing friends.

I can't thank enough Rahul for being such a good friend. I had so much fun with you my friend, in the office, in the lab, in our flat and at all the trips we went together.

I really appreciate the help from all the collaborators: Alexis Askitopoulos and especially Pavlos Lagoudakis in Moscow and Southampton; Sai Kiran in St Andrews; Tersilla Virgili, Marco Cavazzini and Francesco Galeoti in Milan; Paolo Michetti in Dresden.

Finally, a big thank you to my supervisor David Lidzey for giving me the opportunity to work in his amazing group and guiding me throughout my PhD. I could not have wished for a better supervisor.



## Abstract

This thesis concerns the fabrication and study of strongly coupled organic microcavities containing a series of different boron-dipyrromethene (BODIPY) fluorescent dyes dispersed in an optically inert polystyrene matrix.

The photophysics of the different BODIPY dyes are first studied and it is shown that they are promising materials for polariton condensation. DBR-DBR microcavities containing thin films of dye/polystyrene blends are then investigated under angular white-light reflectivity and CW laser excitation; measurements that show that they can enter the strong coupling regime. Polaritons in such high quality factor structures are shown to undergo a phase transition when excited with a high density pulsed excitation, forming a polariton condensate. Power dependent and interferometry measurements are used to identify the condensation threshold and the spatial coherence length of the polariton condensate.

Lower Q-factor microcavities, comprised of two silver mirrors are fabricated, containing two different BODIPY dyes. Energy transfer between the molecules is engineered using two different processes; (1) direct short-range dipole-dipole coupling between the molecules, and (2) polariton-mediated energy transfer. We assess the efficiency of the energy transfer by quantifying the polariton population density along each polariton branch following laser excitation. It is concluded that short-range (<3 nm) energy transfer induced by dipole-dipole coupling is more efficient compared to long-range (60 nm) polariton-mediated energy transfer, although the long-range process is estimated to transfer up to 87% of states to the lower-polariton branch.

The generation of anti-Stokes polariton fluorescence is studied in low Q-factor metallic cavities following resonant excitation at the bottom of the lower polariton branch. Here, it is concluded that thermal energy in the system provides the excess of energy needed for emission of photons having higher energy than that of the initial laser excitation. Using temperature dependent and time resolved measurements it is concluded that polaritons return to the exciton reservoir by optically pumping a molecule in a vibrationally excited ground state. The exciton created then emits fluorescence that populates polariton states with an energy higher than the laser energy

resulting in anti-Stokes polariton fluorescence. We believe such systems will be of significant interest in exploring laser-cooling phenomena in solid-state systems.

## Publications

Grant, R. T. *et al.* Efficient Radiative Pumping of Polaritons in a Strongly Coupled Microcavity by a Fluorescent Molecular Dye. *Adv. Opt. Mater.* **4**, 1615 (2016).

**Georgiou K.** and Cookson T. *et al.* A Yellow Polariton Condensate in a Dye Filled Microcavity. *Adv. Opt. Mater.* **5**, 1700203 (2017).

Musser, A. J., Rajendran, S. K., **Georgiou, K.** *et al.* Intermolecular states in organic dye dispersions: excimers vs. aggregates. *J. Mater. Chem. C* **5**, 8380–8389 (2017).

**Georgiou K.** *et al.* Control over energy transfer between fluorescent BODIPY dyes in a strongly coupled microcavity. *ACS Photonics* **5**, 258-266 (2018).

**Georgiou K.** *et al.* Generation of anti-Stokes fluorescence in a strongly coupled organic semiconductor microcavity. *ACS Photonics* **5**, 4343-4351 (2018).

Jayaprakash R., **Georgiou K.** *et al.* Hybrid organic-inorganic polariton LED. *Manuscript under review.*



## Conferences and Workshops

2<sup>nd</sup> Russian-British workshop for young scientists: Advanced Polaritonics and Photonics, Suzdal, Russia, March 2015.

Workshop on Condensates of Light, Buckinghamshire, UK, January 2016.

**Kyriacos Georgiou**, Richard T. Grant, Tersilla Virgilli, Francesco Galleotti, Zhen Shen, Caspar Clark, David G. Lidzey. ‘Strongly coupled microcavities containing different fluorescent molecular BODIPY-core structures.’ ICSCE8, Edinburgh, UK, April 2016.

**Kyriacos Georgiou**, Richard T. Grant, Tersilla Virgilli, Francesco Galleotti, Zhen Shen, Caspar Clark, David G. Lidzey. ‘Hybridization of Frenkel-excitons through strong coupling.’ Research away day, Sheffield, UK, July 2016.

**Kyriacos Georgiou**, Rahul Jayaprakash, Alexis Askitopoulos, Tersilla Virgilli, Francesco Galleotti, Zhen Shen, Pavlos Lagoudakis, David G. Lidzey. ‘Laser cooling of organic hybrid microcavities.’ EOSAM, Berlin, Germany, September 2016.

**Kyriacos Georgiou**, Rahul Jayaprakash, Alexis Askitopoulos, Tersilla Virgilli, Francesco Galleotti, Zhen Shen, Pavlos Lagoudakis, David G. Lidzey. ‘Laser cooling of organic hybrid microcavities.’ Science of the future, Kazan, Russia, September 2016.

**Kyriacos Georgiou**, Rahul Jayaprakash, Alexis Askitopoulos, David M. Coles, Marco Cavazzini, Pavlos Lagoudakis, David G. Lidzey. ‘Anti-Stokes emission in a strongly coupled organic semiconductor microcavity.’ UK Semiconductors, Sheffield, UK, July 2017.

International School on Polaritonics and Photovoltaics, Sicily, Italy, August 2017.



# Contents

Acknowledgements .....	iii
Abstract .....	v
Publications .....	vii
Conferences and Workshops .....	ix
Chapter 1. Introduction.....	1
1.1. Thesis outline.....	3
1.2. Alternative thesis format .....	5
1.3. References .....	6
Chapter 2. Theory of microcavity organic exciton-polaritons .....	9
2.1. Organic materials .....	9
2.1.1. Organic semiconductors.....	10
2.1.2. Optical absorption, vibrational relaxation and emission .....	14
2.2. Optical microcavities and cavity photons .....	19
2.2.1. Confined photons .....	19
2.2.2. Cavity mirrors .....	23
2.3. Exciton-polaritons .....	27
2.4. Polariton condensates and lasers .....	34
2.5. Strong coupling in planar microcavities: A historical review.....	39
2.5.1. Polariton lasing .....	42
2.5.2. New effects in organic microcavities .....	44
2.5.3. The importance of the exciton reservoir .....	44
2.6. References .....	49
Chapter 3. Exploring the photophysics of BODIPY-core materials as microcavity active layers.....	57
3.1. Introduction.....	57
3.2. Photoluminescence quantum yield .....	59
3.3. Photo-oxidation.....	60
3.4. Amplified spontaneous emission.....	62
3.5. Strong coupling in BODIPY-filled microcavities.....	70
3.6. Analysis of PL distribution.....	75
3.7. Conclusions .....	78
3.8. References .....	80
Chapter 4. A yellow polariton condensate in a dye filled microcavity.....	83

4.1. Motivation of work .....	83
4.2. Author contributions.....	84
4.3. Publication .....	84
<b>Chapter 5. Control over energy transfer between fluorescent BODIPY dyes in a strongly coupled microcavity .....</b>	<b>91</b>
5.1. Motivation of work .....	91
5.2. Author contributions.....	92
5.3. Publication .....	92
5.4. Supporting Information .....	102
<b>Chapter 6. Generation of anti-Stokes fluorescence in a strongly coupled organic semiconductor microcavity.....</b>	<b>105</b>
6.1. Motivation of work .....	105
6.2. Author contributions.....	106
6.3. Publication .....	106
6.4. Supporting Information .....	116
<b>Chapter 7. Conclusions and future work .....</b>	<b>123</b>
7.1. Conclusions .....	123
7.2. Future work .....	125

## Chapter 1. Introduction

Each and every photon that enters the Earth's atmosphere interacts with matter through absorption or Rayleigh scattering with atoms and molecules. Blue photons are scattered more than red by particles in the atmosphere, and hence the sky appears blue. Light-matter interaction was studied by Newton more than three centuries ago when he used prisms to separate white light into its components.<sup>1</sup> Since then, humans have manipulated light in many ways through light-matter interactions; ranging from fabrication of optical elements used in photonic experiments to contact lenses for vision correction. For this reason is very important to understand light-matter interaction. For instance, Raman spectroscopy utilises the ability of photons to scatter with matter to observe rotational, vibrational and other low frequency modes that helps us identify the chemical composition and structure of a sample.<sup>2</sup> Photons, being "messengers" from the universe, allow astronomers to observe spectral lines in a star's emission and analyse its constituents. Very recently, it was announced that laser light will be used to provide momentum to light-weight robotic spacecrafts that will be sent to the outer space, accelerating them to a speed as fast as one fifth of the speed of light in order to study the nearest stars to our solar system.<sup>3</sup>

At small length-scales, nanostructures can provide confinement of a photon's electromagnetic field. Usually, this is achieved by placing two highly reflective mirrors in close proximity, having a separation distance on the order of a micrometre or sub-micrometre. Such structures are termed microcavities. If a semiconducting material is placed in a microcavity in the vicinity of the confined electric field, with a transition resonant with the energy of the field, light (photons) and matter (matter excitations) start to interact with each other. This light-matter interaction can be described by two regimes. In the so-called weak coupling regime, Fermi's Golden Rule is valid and the interaction can be described by perturbation theory. In the case of a reversible exchange of energy between light and matter (where the energy exchange rate is faster than the semiconductor exciton dephasing rate and the rate at which photons escape from the microcavity), the strong coupling regime is realised. In this regime, Fermi's Golden Rule does not hold and new hybrid bosonic half-light half-matter eigenstates, termed cavity-polaritons, are formed.

Cavity-polaritons are a coherent superposition of excitons and photons and have properties of both.<sup>4</sup> This matter component allows polaritons to interact with excitons, phonons and with other polaritons at high densities. However, polaritons have a very light mass ( $10^{-5}$  the mass of the free electron) because of their photonic character. This also leads to a short finite lifetime in the range of tens of fs to hundreds of ps. Polaritons are bidimensional quasi-particles, described by their energy and in-plane momentum. They have a distinctive near parabolic dispersion with an energy minimum at zero wavevector, and manifest themselves with a normal mode splitting at the energy where their constituent photon mode and excitons are degenerate.

Strong coupling in planar microcavities was demonstrated for the first time more than 25 years ago utilising inorganic quantum wells (QWs) at cryogenic temperatures,<sup>4</sup> and using organic semiconductors at room temperature a few years later.<sup>5</sup> Since then, great advancements have been made using polaritons in inorganic,<sup>6-14</sup> organic<sup>15,16,25,17-24</sup> and hybrid structures.<sup>26,27</sup>

## 1.1. Thesis outline

In Chapter 2, organic materials are introduced and the bonding between carbon atoms is used to explain how organic materials inherit their semiconducting properties. Next, the physics of confined photons in planar microcavities is discussed in detail with a focus on their interaction with organic semiconductor excitons. The weak and strong coupling regimes are explained and the physics of organic polaritons is introduced. It is shown how the half-light half-matter nature of polaritons can be used to study condensation, lasing and other interesting physical phenomena at room temperature. A historical review of important achievements in strongly coupled microcavities is then presented with a focus on organic semiconductor microcavities.

The experimental Chapters in this thesis are based on published work undertaken by the author during the 4 year period of his PhD. Chapter 3 is a conventional thesis chapter composed of the author's published and unpublished work. Alternative format Chapters 4-6 are comprised of three papers as they appear online in their published format or in the appropriate format needed during submission for publication.

In Chapter 3, a comprehensive study of the photophysics of boron dipyrromethene (BODIPY) materials is presented. It is explained why such fluorescent dyes are favourable for application as the active layers in strongly coupled microcavities. The demonstration of strong coupling is then achieved in a series of microcavities filled with 5 different BODIPY derivatives. A standard two-level coupled oscillator model is used to describe the coupling between photons and excitons in such cavities.

The low effective mass of organic-polaritons is a property inherited from their photonic component, and in combination with the large binding energy of Frenkel excitons, makes them a useful platform in which to study condensation and lasing at room temperature. In Chapter 4, a high quality BODIPY-filled strongly coupled microcavity is studied under intense optical excitation. At high pulsed excitation densities, a phase transition occurs and a polariton condensate in the yellow region of the spectrum is realised at room temperature. This "yellow polariton condensate" is manifested by a laser-like emission, an emission blueshift and a linewidth reduction above threshold. Interferometry measurements are then used to show that the condensate has a high degree of spatial coherence.

Chapter 5 describes how two different BODIPY dyes can be placed inside a microcavity in order to study the efficiency of energy transfer between the materials. This is achieved by probing the emission and population density of the different polariton branches. Two structural configurations are used; one which allows the coupling between the dipoles of the two different materials resulting in short-range energy transfer, the other induced by their hybridisation with the same confined optical mode (so-called polariton-mediated long-range energy transfer). It is concluded that the polariton-mediated energy transfer is not as efficient as the short-range energy transfer, which is based on Förster resonant energy transfer and has an efficiency close to unity.

Chapter 6 details how resonant excitation of the bottom of the lower polariton branch (LPB) of a BODIPY-filled strongly coupled microcavity is used to generate anti-Stokes fluorescence (ASF) of polaritons along the LPB. Time resolved and temperature dependent photoluminescence measurements on films and cavities suggest that polaritons are injected in the bottom of the LPB upon laser excitation. These then optically pump a molecule that is initially in a vibrationally excited ground state. An excess of energy in the reservoir (provided by the thermal energy of the system), is then used to allow polariton states to be populated at higher energy than the energy of the laser excitation. This ASF process in cavities seems to be more efficient than ASF in control thin films. We conclude that this enhancement in ASF occurs as Stokes emission is suppressed due to the fact that such modes exist at an energy below the cut-off energy of the cavity mode where the density of states is near-zero.

## **1.2. Alternative thesis format**

The published papers incorporated in this thesis, form a coherent body of work and therefore, it was decided that the thesis should be presented in an alternative format consisting of published papers instead of conventional thesis chapters.

In the first paper (Chapter 4), a polariton condensate is realised in a material system where the fluorescent molecules are dispersed in an optically inert polymer matrix. This allows the dye/polymer concentration ratio to be tuned. In addition, there are many different molecules that can be dispersed in polymers, spanning wavelengths from the UV to the IR, opening the possibility of achieving polariton lasing at spectral regions where lasing is not readily achieved (i.e. the yellow-orange region). A key component of reaching a condensation threshold is to efficiently populate the bottom of the lower polariton branch. Combining different materials in the same structure, as discussed in the paper of Chapter 5, can be used to control the energy transfer between molecules and efficiently populate the lower energy state.

Organic materials have vibrational and rotational modes that are usually not taken into account when constructing microscopic models of polariton condensation. Although recent theoretical work has focused in this direction, there is very little in the way of underpinning experimental evidence to support theory. Finally, in Chapter 6, we demonstrate how rovibrational modes can interact with polaritons and how they can exchange energy leading to the generation of anti-Stokes fluorescence.

### 1.3. References

1. Newton, I. A Letter of Mr. Isaac Newton, Professor of the Mathematicks in the University of Cambridge; Containing His New Theory about Light and Colors: Sent by the Author to the Publisher from Cambridge, Febr. 6. 1671/72; In Order to be Communicated to the R. Socie. *Philos. Trans. R. Soc. London* **6**, 445–460 (1671).
2. Raman, C. V. & Krishnan, K. S. A New Type of Secondary Radiation. *Nature* **121**, 501–502 (1928).
3. Marx, G. Interstellar Vehicle Propelled By Terrestrial Laser Beam. *Nature* **211**, 22–23 (1966).
4. Weisbuch, C., Nishioka, M., Ishikawa, A. & Arakawa, Y. Observation of the coupled exciton-photon mode splitting in a semiconductor quantum microcavity. *Phys. Rev. Lett.* **69**, 3314–3317 (1992).
5. D. G. Lidzey *et al.* Strong exciton-photon coupling in an organic semiconductor microcavity. *Lett. to Nat.* **395**, 53–55 (1998).
6. Imamoğlu, A., Ram, R., Pau, S. & Yamamoto, Y. Nonequilibrium condensates and lasers without inversion: Exciton-polariton lasers. *Phys. Rev. A* **53**, 4250–4253 (1996).
7. Baumberg, J. J. *et al.* Parametric oscillation in a vertical microcavity: A polariton condensate or micro-optical parametric oscillation. *Phys. Rev. B - Condens. Matter Mater. Phys.* **62**, 247–250 (2000).
8. Kasprzak, J. *et al.* Bose-Einstein condensation of exciton polaritons. *Nature* **443**, 409–414 (2006).
9. Lagoudakis, K. G. *et al.* Quantized vortices in an exciton-polariton condensate. *Nat. Phys.* **4**, 706–710 (2008).
10. Lagoudakis, K. G. *et al.* Observation of Half-Quantum Vortices in an Exciton-Polariton Condensate. *Science (80-. )*. **326**, 974–976 (2009).
11. Schneider, C. *et al.* An electrically pumped polariton laser. *Nature* **497**, 348–

352 (2013).

12. Bhattacharya, P. *et al.* Room temperature electrically injected polariton laser. *Phys. Rev. Lett.* **112**, 29–31 (2014).
13. Tsintzos, S. I., Pelekanos, N. T., Konstantinidis, G., Hatzopoulos, Z. & Savvidis, P. G. A GaAs polariton light-emitting diode operating near room temperature. *Nature* **453**, 372–375 (2008).
14. Christopoulos, S. *et al.* Room-temperature polariton lasing in semiconductor microcavities. *Phys. Rev. Lett.* **98**, 1–4 (2007).
15. Lerario, G. *et al.* High-speed flow of interacting organic polaritons. *Light Sci. Appl.* **6**, e16212 (2017).
16. Lidzey, D. G. *et al.* Room Temperature Polariton Emission from Strongly Coupled Organic Semiconductor Microcavities. *Phys. Rev. Lett.* **82**, 3316–3319 (1999).
17. Lidzey, D. G. Photon-Mediated Hybridization of Frenkel Excitons in Organic Semiconductor Microcavities. *Science (80-. )*. **288**, 1620–1623 (2000).
18. Kéna-cohen, S. & Forrest, S. R. Room-temperature polariton lasing in an organic single-crystal microcavity. *Nat. Photonics* **4**, 371–375 (2010).
19. Plumhof, J. D., Stoeferle, T., Mai, L., Scherf, U. & Mahrt, R. F. Room-Temperature Bose-Einstein Condensation of cavity exciton-polariton in a polymer. *Nat. Mater.* **13**, 247–252 (2014).
20. Daskalakis, K. S., Maier, S. a, Murray, R. & Kéna-cohen, S. Nonlinear interactions in an organic polariton condensate. *Nat. Mater.* **13**, 271–278 (2014).
21. Coles, D. M. *et al.* Polariton-mediated energy transfer between organic dyes in a strongly coupled optical microcavity. *Nat. Mater.* **13**, 712–719 (2014).
22. Cookson, T. *et al.* A Yellow Polariton Condensate in a Dye Filled Microcavity. *Adv. Opt. Mater.* **5**, 1700203 (2017).
23. Coles, D. M. *et al.* Strong coupling between chlorosomes of photosynthetic

- bacteria and a confined optical cavity mode. *Nat. Commun.* **5**, 5561 (2014).
24. Coles, D. *et al.* A Nanophotonic Structure Containing Living Photosynthetic Bacteria. *Small* **13**, 1701777 (2017).
  25. Lerario, G. *et al.* Room-temperature superfluidity in a polariton condensate. *Nat. Phys.* **13**, 837–841 (2017).
  26. Paschos, G. G. *et al.* Hybrid organic-inorganic polariton laser. *Sci. Rep.* **7**, 11377 (2017).
  27. Höfner, M., Sadofev, S., Kobin, B., Hecht, S. & Henneberger, F. Hybrid polaritons in a resonant inorganic/organic semiconductor microcavity. *Appl. Phys. Lett.* **107**, 22–25 (2015).

## **Chapter 2. Theory of microcavity organic exciton-polaritons**

Chapter 2 aims to give an insight into the physics of organic semiconductors, optical microcavities and organic exciton-polaritons. As will be discussed, these are a useful platform for studying fundamental and intriguing physical phenomena.

### **2.1. Organic materials**

There is no unambiguous definition of organic materials, but it is generally accepted that they are compounds rich in carbon and hydrogen, and sometimes contain nitrogen and oxygen. They are found in nature but can also be synthesised in the form of small molecules, monomers, oligomers and polymers. Changing the number of atoms and molecular configurations as well as the bonds between atoms can create an infinite number of combinations with each combination corresponding to a new organic material. Therefore, the optical and electronic properties of organic materials can be tailored depending on their application.

In the past century, the inorganic semiconductor industry has led the development of modern technologies used in consumer electronics and optoelectronics. Silicon-based devices have been used to harvest the energy of sunlight for electricity generation and control the current flow in electronic circuits.<sup>1,2</sup> However, such inorganic semiconducting materials and devices have some disadvantages compared to their organic counterparts. For example, the growth of silicon is a difficult process, requiring the use of expensive and time-consuming techniques, making it unsuitable for what it is called “disposable electronics”. On the other hand, solution-processed organic materials can be easily mass-produced at low cost, making them a strong candidate to replace mature silicon-based technologies. Organic optoelectronics have been expanding rapidly in the last couple of decades, with progress led by display technologies with devices using organic light emitting diodes (OLEDs)<sup>3,4</sup> becoming widely available.

### 2.1.1. Organic semiconductors

Inorganic materials owe their semiconducting properties to the periodic structure of the crystalline solid, which results in the formation of the valence band (VB) and conduction band (CB). These two bands are separated by an energy termed the band gap of the semiconductor. If a material has a band gap greater than around 4 eV, it is considered to be an insulator. If the two bands overlap resulting in zero band gap energy, the material is classed as a conductor (metal). In the case of semiconductors, the band gap energy lies somewhere between that of a metal and an insulator. Organic materials can form crystals but are often found in a non-crystalline form. However, they have a band gap similar to that found in inorganic semiconductors, with their semiconducting properties arising from the bonding of atoms.

Electrons in atoms are confined in discrete energy states called orbitals, which are described by solutions of the Schrödinger equation. These can be characterised by different quantum numbers; the principal quantum number,  $n$ , takes values  $n = 1, 2, 3, \dots$  etc.,. The size of the orbitals determines the size of the atoms; i.e. the larger the principal quantum number, the larger the orbital, and this consequently increases the size of the atom. The angular momentum quantum number of the orbital,  $l$ , can take values of  $l = 0, 1, 2, 3, \dots$  etc., or using the nomenclature  $l = s, p, d, f, \dots$  etc., respectively, and it is responsible for the shape of the orbital. The magnetic quantum number,  $m_l$ , takes integer values between  $-l$  and  $+l$ , and defines the orientation of the orbital. For instance, for a given value of  $n$ , there is only one permitted orientation for  $s$  orbitals ( $l = m_l = 0$ ) which has a spherical shape. Dumbbell-shaped  $p$  orbitals have three allowed orientations which are perpendicular to one another and are denoted as  $p_x$ ,  $p_y$  and  $p_z$ . When orbitals of the same phase overlap with one another, they form bonding orbitals. Sharing electrons in bonding orbitals bind the atoms together causing the overall energy of the system to reduce. Overlapping orbitals with different phase result in the formation of so called anti-bonding orbitals where the atoms repel one another and the total energy of the system is higher than that of individual atoms. The overlap of orbitals can be “end-on” or “side-on”. End-on bonding (anti-bonding) results in a  $\sigma$ -bond ( $\sigma^*$ -bond), whilst side-on bonding (anti-bonding) results in a  $\pi$ -bond ( $\pi^*$ -bond). The latter are weaker bonds and tend to be delocalized over one or more atoms or molecules. In more complicated systems, the concept of hybridisation

must be introduced in order to describe the bonding of atoms. In the following paragraphs, the bonding process between carbon atoms is used to explain the concept of hybridisation.

Carbon atoms have 6 electrons of which 4 are valence electrons that can take part in bonding. Carbon-based materials are bound together through covalent bonds by sharing electrons and tend to fill their outermost orbitals in order to minimise their energy. In its ground state, the electronic structure of a neutral and isolated carbon atom is  $1s^2 2s^2 2p^2$ . The inner shell of the atom of carbon is filled ( $1s^2$ ) with two electrons with opposite spin as required by Pauli's Exclusion Principle, so they can be ignored when discussing the bonding of carbon atoms. However, when carbon atoms are involved in the formation of covalent bonds with other atoms, an electron from the  $2s$  shell is promoted to the  $2p_z$  orbital creating the electronic configuration  $1s^2 2s^1 2p^3$ . The remaining  $2s$  electron can hybridise with one, two or even all three  $2p$  electrons forming hybridised orbitals. The three different combinations can give rise to (i) two hybrid  $sp$  with two remaining  $2p$  orbitals, (ii) three hybrid  $sp^2$  with one remaining  $2p$  orbital and (iii) four hybrid  $sp^3$  orbitals, respectively.<sup>5</sup> In  $sp$  hybridisation the hybrid orbitals are at  $180^\circ$  to each other with the two remaining  $2p$  orbitals being perpendicular to the hybrid  $sp$  orbital. In  $sp^2$  hybridisation, the three hybrid orbitals lie on the same plane at an angle of  $120^\circ$  to one another with the one remaining  $2p$  orbital being perpendicular to the hybrid orbital plane. In the case of  $sp^3$ , the four hybrid orbitals lie in a tetrahedral configuration separated by an angle of  $109.5^\circ$ . The hybridisation process including the electronic configurations along with the orbital orientation is summarised in Figure 2.1.

In the case where two  $sp$  hybridised atoms bond together, one  $sp$  hybrid orbital from the first atom overlaps with one  $sp$  hybrid orbital from the second atom, forming a  $\sigma$ -bond. The two remaining  $2p$  orbitals of each atom (which lay at a perpendicular orientation to the direction of the  $\sigma$ -bond) form two  $\pi$ -bonds. Therefore,  $sp$  hybridised atoms bond together through a so-called triple bond consisting of one  $\sigma$ -bond and two  $\pi$ -bonds. The remaining  $sp$  hybrid orbital that is not involved in the bonding process is free to bond to other atoms.

When two  $sp^2$  hybrid atoms bond to one another, a  $\sigma$ -bond is formed between two  $sp^2$  hybrid orbitals. The one remaining  $2p$  orbital from each atom overlaps to form a  $\pi$ -

bond, resulting in a double bond that is composed of one  $\sigma$ -bond and one  $\pi$ -bond. Again, the two remaining  $sp^2$  hybrid orbitals are available to form bonds with other atoms.

In the case where two  $sp^3$  hybridised atoms bond together, one of the four  $sp^3$  hybrid orbitals from each atom overlaps to form a  $\sigma$ -bond. The remaining three  $sp^3$  hybrid orbitals from each atom are then available to form bonds with other atoms.

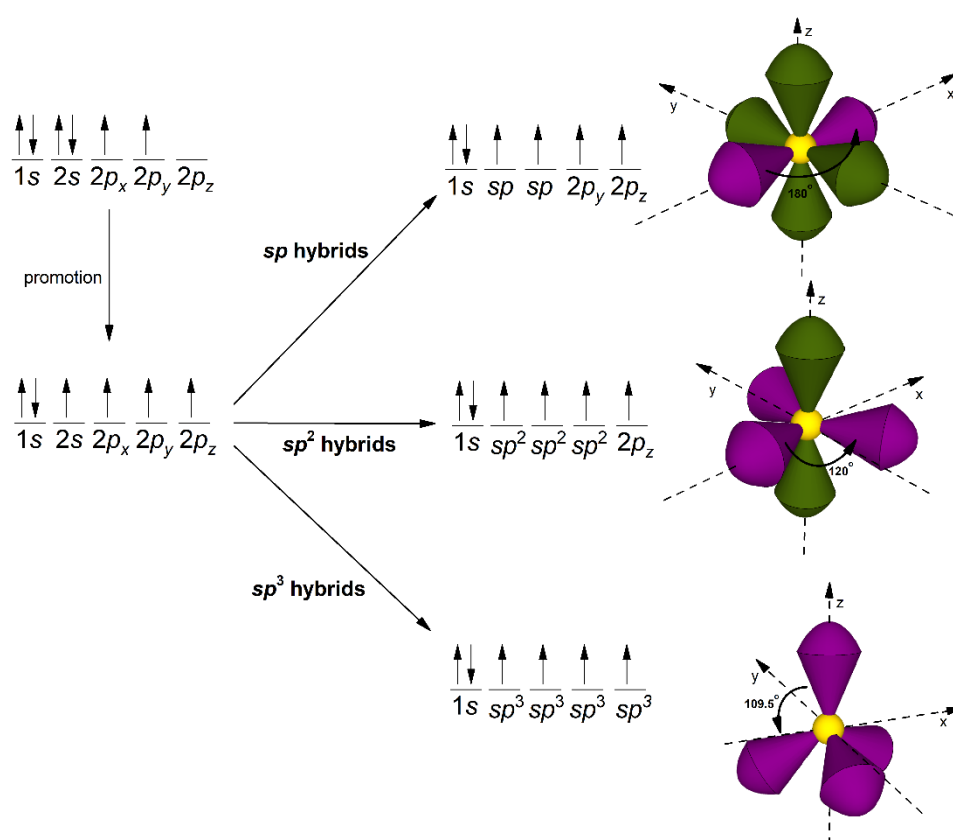


**Figure 2.1.** The hybridization process starting with the promotion of a 2s electron to 2p<sub>z</sub>. The three possible hybrid orbital electronic configurations are shown along with the orientations of the hybrid orbitals.

As can be understood from the description of bonding between hybridised atoms, strong  $\sigma$ -bonds result from the end-on overlap between hybridised orbitals, whilst the

unhybridised  $2p$  orbitals are responsible for weaker and more delocalized  $\pi$ -bonds. A very good example is the benzene ring, which consists of six  $sp^2$  hybridised carbon atoms. The six carbon atoms are bound to each other, forming six  $\sigma$ -bonds through end-on overlapping of  $sp^2$  orbitals of neighboring atoms. Each carbon atom contributes two out of three  $sp^2$  hybrid orbitals to form  $\sigma$ -bonds with two neighboring carbon atoms, while the remaining  $sp^2$  orbital of each carbon atom overlapping to form a  $\sigma$ -bond with the spherical  $1s$  orbital of hydrogen. The  $2p$  unhybridised orbitals of the six atoms are responsible for the formation of three  $\pi$ -bonds (in the lowest energy configuration). Therefore, the benzene ring has three single ( $\sigma$ -bonds) and three double bonds (consisting of one  $\sigma$ -bond and one  $\pi$ -bond) appearing in an alternating arrangement. Systems having alternating single and multiple bonds as a result of connected  $p$ -orbitals are known as conjugated systems, which generally are characterised by lower molecular energy and increased stability. The electrons of the  $\pi$ -bonds are delocalized over a large area above and below the hexagonal plane of benzene and since there are six out of plane  $2p$  orbitals, there will be six possible molecular orbitals (MOs).

Figure 2.2 shows the six possible molecular orbitals of the benzene ring with three bonding orbitals (lower energy MOs), and three anti-bonding orbitals (higher energy MOs). Each of the six  $2p$  orbitals contains one electron and according to Pauli's Exclusion Principle, two electrons with opposite spin can occupy each molecular orbital. Therefore the three lowest energy MOs are filled with six electrons (two electrons with opposite spin each) whilst the three highest energy MOs remain empty as shown in Figure 2.2. The highest occupied molecular orbital (HOMO) and the lowest unoccupied molecular orbital (LUMO) in benzene consist of two energetically degenerate orbitals. An electron from the HOMO level can be promoted to the LUMO level following the absorption of a sufficient amount of energy (corresponding to the band gap energy). The promotion of an electron from the HOMO to LUMO leaves behind a positively charged hole. The electron-hole pair is a bound state called an exciton. The similarity of HOMO and LUMO levels in an organic semiconductor to the VB and CB band in inorganic semiconductors is clear, and qualitatively explains how organic materials obtain their semiconducting properties.

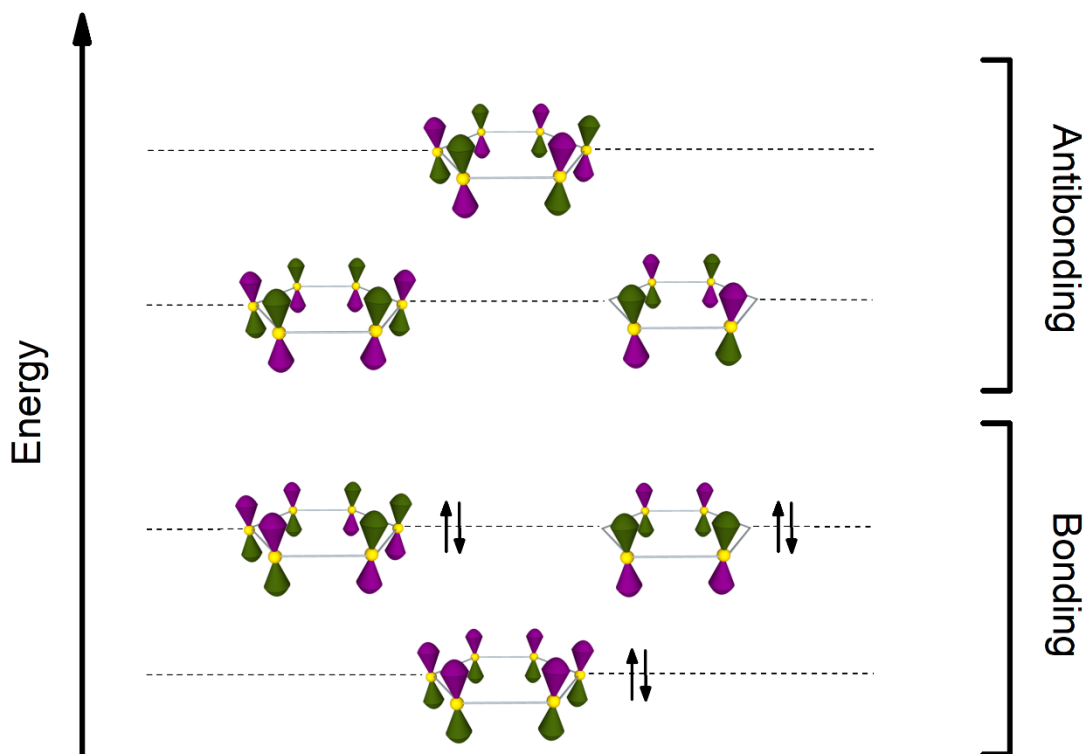


**Figure 2.2.** The six allowed molecular orbitals of benzene along with the  $\pi$ -bond configurations and the electron populations of the molecular ground state.

### 2.1.2. Optical absorption, vibrational relaxation and emission

Absorption of light by a medium usually occurs when a photon transfers its energy to a bound electron in a ground state and excites it to an excited state. For example, in a molecular system, a photon is absorbed by an electron in the HOMO and transfers it to the LUMO. This transition is only possible if the energy of the photon,  $E_\gamma$ , is resonant or close to resonant with the energy levels of the material as shown in Equation 2.1, assuming the two energy levels being  $E_{HOMO}$  and  $E_{LUMO}$

$$E_\gamma = h\nu = \frac{hc}{\lambda} = E_{LUMO} - E_{HOMO} \quad (2.1)$$

Here,  $h$  is Planck's constant,  $\nu$  is the photon frequency,  $c$  is the speed of light and  $\lambda$  the wavelength of the photon.

The probability of a photon being absorbed by a molecule is greater when the photon energy corresponds to an electronic transition. This probability for a photon of wavelength  $\lambda$  is defined by the absorption cross section,  $\sigma(\lambda)$ , which has units of area. The absorption coefficient,  $\alpha(\lambda)$ , for  $N$  molecules per unit volume, can be defined as the product of  $N$  and  $\sigma(\lambda)$  and it is expressed as an inverse length. In other words,  $\alpha(\lambda)$  is the fraction of the power of a light beam absorbed per unit length when traveling in an absorbing medium.<sup>6</sup> If the optical intensity of the propagating beam is initially  $I_0$ , after traveling a distance  $z$  it is  $I_z$ , then for a distance  $dz$ , the reduction in intensity  $dI$  (assuming no scattering) is given by

$$dI = -I\alpha dz \quad (2.2)$$

Integration of Equation (2.2) gives rise to the Beer-Lambert law as shown in Equation (2.3)

$$I_z = I_0 e^{-\alpha z} \quad (2.3)$$

The transmission of the beam,  $T$ , is defined as the ratio between the attenuated and unattenuated optical intensity

$$T = \frac{I_z}{I_0} = e^{-\alpha z} \quad (2.4)$$

Equation 2.5 shows that the optical density (O.D.) of a medium, also known as the absorbance,  $A$ , is the negative base 10 logarithm of  $T$  and can be related to the absorption coefficient through Equation 2.6.<sup>6</sup>

$$A = -\log_{10} T = -\log_{10} \frac{I_z}{I_o} \quad (2.5)$$

$$A = \frac{-\alpha z}{-\log_e 10} = 0.43\alpha z \quad (2.6)$$

A molecule can be visualised as a system where the atoms correspond to point masses and the bonds between them to springs. Such a system exists in its lowest energy when the bond (spring) is at its equilibrium length. Any stretching or compression of the bond results in an increase of the system's energy. The energy of the system with respect to the separation of the atoms is represented by the Morse potential which is very similar to the harmonic oscillator potential (Figure 2.3). This atom-bond system can oscillate with allowed, discrete frequencies which manifest themselves as vibrational energy levels within the Morse potential as shown in Figure 2.3. At room temperature, an electron can usually be found at the lowest vibronic energy level,  $v_o$ , of the HOMO. Generally, the different orbitals represent different energy levels with the HOMO (ground state) and LUMO (first excited state) denoted using  $S_0$  and  $S_1$ , respectively, where  $S$  stands for singlet (spin-paired states in a multi-electron system). Higher energy orbitals are denoted with a consecutively increasing subscript. Following the absorption of a photon, an electron from the HOMO level is excited to the LUMO. The Frank-Condon principle states that the probability of the transition of an electron from the HOMO to a particular vibronic level in the LUMO depends on the vibronic wavefunction overlap of the initial and final states as shown in Figure 2.3. Greater overlap results in a greater probability for the particular electronic transition to take place, with this principle applying to all photon-mediated electronic transitions. Electronic transitions are spin conservative and therefore promotion of an electron from the singlet molecular ground state must be to a singlet excited state. The promoted electron leaves behind a positively-charged hole and the two can be bound together through Coulomb attraction and form a neutrally-charged bound state, known as an exciton. In organic materials the Frenkel-like excitons have a large binding energy (0.1-1 eV), unlike the binding energy of Wannier-Mott excitons (a few meV) in inorganic materials which suffer screening due to high dielectric constants and are usually unstable at room temperature.

Upon excitation to an excited electronic and vibronic state, the electron relaxes to the lowest vibronic level of the excited electronic state,  $S_{1v_0}$ . From there, it can drop from LUMO  $S_{1v_0}$  to the HOMO  $S_{0v_n}$ , with  $v_n$  being determined by the Frank-Condon principle. The electron will eventually recombine with the hole (exciton decay). This recombination can be radiative resulting in the emission of a photon of lower energy than that of the absorbed photon, known as fluorescence (Figure 2.3). The energy difference between the absorbed and the emitted photon is equal to the loss of energy during the vibrational relaxation of the system. The strength of the emission transition is equal to the strength of the absorption transition due to symmetry considerations. In the case of the maximum absorption  $S_{0v_0} - S_{1v_0}$  and maximum emission  $S_{1v_0} - S_{0v_0}$ , there is an energy shift between the two transitions which is called the Stokes shift even without vibrational relaxation. This loss of energy is dissipated in the system as heat and it is caused by interactions of the molecule with its surrounding medium and rotation of the molecular dipole in order to minimise its energy with surrounding dipoles. In an ideal system, the fluorescence can be considered as a mirror image of the absorption as shown in Figure 2.4.

There is a small probability that an electron in the LUMO level, instead of radiatively decaying back to HOMO through fluorescence, can be transferred to the first triplet state,  $T_1$  (triplet denoted as  $T$ ); a process called intersystem crossing (see Figure 2.3). In order to pass from  $S_1$  to  $T_1$ , an electron will need to flip its spin in order to be parallel with the spin of the ground state electron in  $S_0$ . Intersystem crossing occurs through spin-orbit coupling or through interaction with neighbouring molecules. After intersystem crossing, a transition from  $T_1$  to  $S_0$  is less probable as it is a spin-forbidden transition and occurs over longer timescales (milliseconds to minutes). The radiative decay from triplet to singlet is known as phosphorescence (Figure 2.3). It is possible that the electron could be transferred back to  $S_1$  and then decay through delayed fluorescence.

Relaxation from an excited electronic state to the ground state can also occur through non-radiative decay pathways. There are instances where the higher-lying vibronic energy levels of the ground state overlap with the lower vibronic energy levels of the first excited state. In this case, vibrational relaxation from an excited electronic and

vibronic state to the zero vibronic level of the ground state can occur, with all energy being dissipated in the system as thermal energy.

The fluorescence efficiency of a material is defined by its fluorescence quantum yield, ( $\Phi$ ). This is the ratio between the number of emitted and absorbed photons by a material.

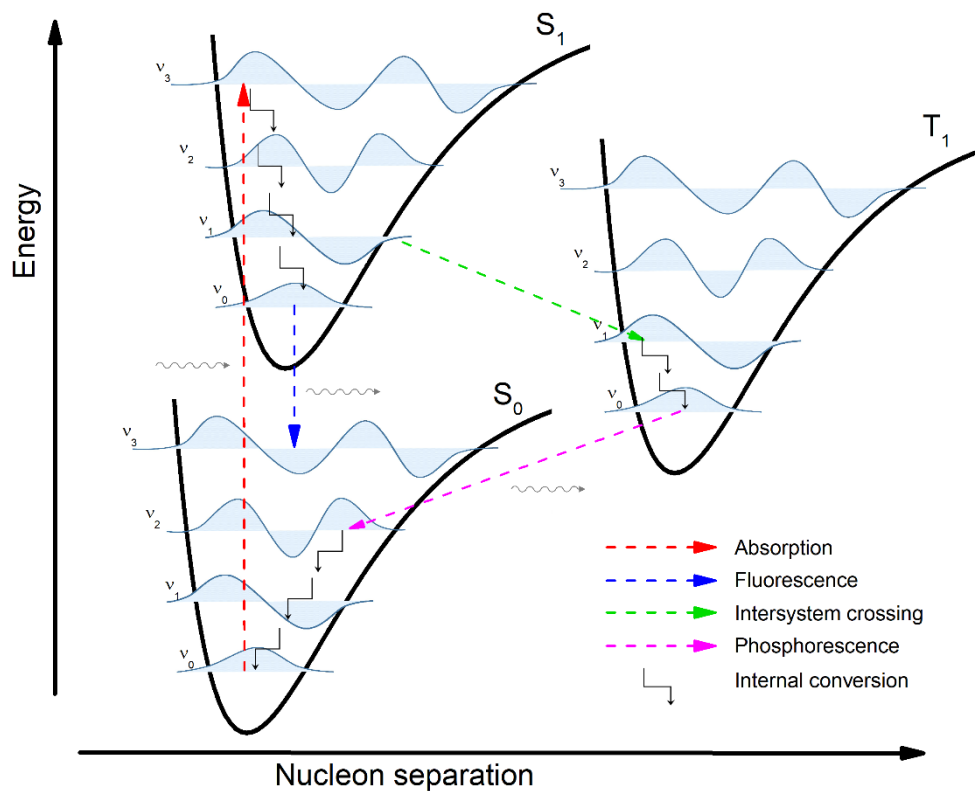


**Figure 2.3.** The dashed lines indicate transitions in the system - absorption and emission (fluorescence and phosphorescence) along with intersystem crossing. The solid lines show the non-radiative internal relaxation process.

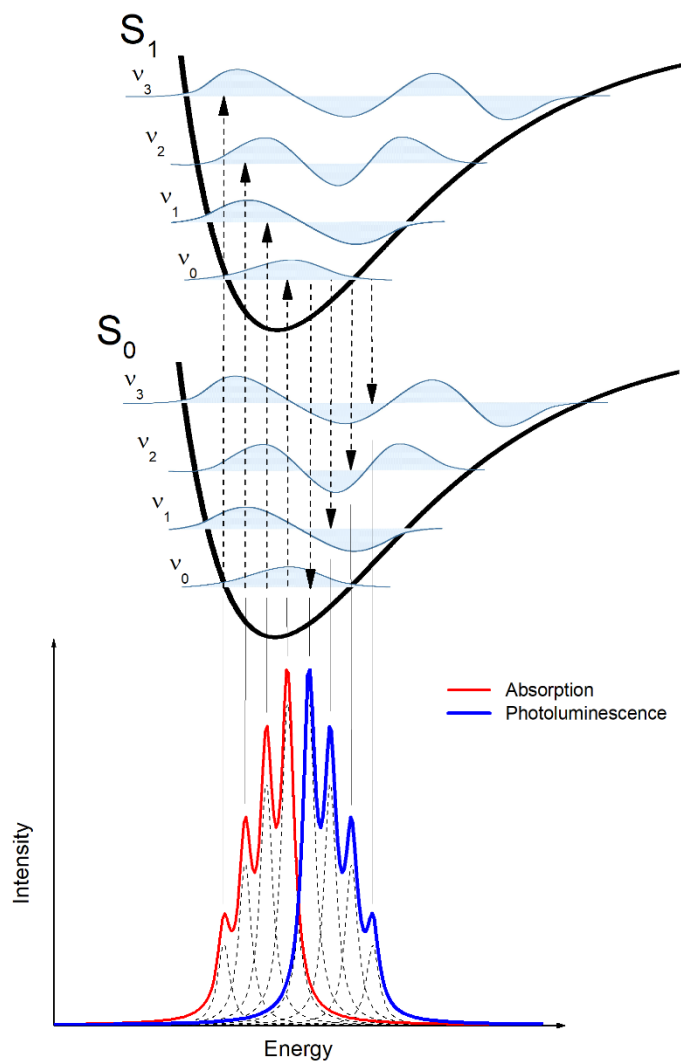


**Figure 2.4.** The Frank – Condon principle results in the characteristic absorption and emission spectra of a molecule being mirror images and shifted in energy.

## 2.2. Optical microcavities and cavity photons

### 2.2.1. Confined photons

A key requirement for the development of systems that can enter the strong coupling regime is to confine photons in a manner that allow their interaction with a semiconducting material. Microcavities are optical resonators that provide confinement of light through constructive interference in the form of standing waves, and have a size on the order of the wavelength of the confined photons. Depending on

the material system and application, different structures can be used to create confinement in one or more dimensions. This thesis concerns experiments where light was confined in one dimension, therefore the discussion will be limited to Fabry-Perot resonators. Fabry-Perot resonators are comprised by two planar, highly reflective surfaces that are separated by a distance  $d_c$  as shown in Figure 2.5. This distance determines the photon wavelength  $\lambda_c$  that is confined between the mirrors, and can be described by the following expression

$$\lambda_c = \frac{2\eta_c d_c}{q} \cos \theta_{int} \quad (2.7)$$

Here,  $\eta_c$  is the effective refractive index of the medium between the mirrors at the resonant wavelength of the cavity,  $q$  is the cavity order, which takes integer values  $q = 1, 2, 3, 4, \dots$  etc. and  $\theta_{int}$  is the angle of propagation within the cavity with respect to the normal incidence of the cavity surface.

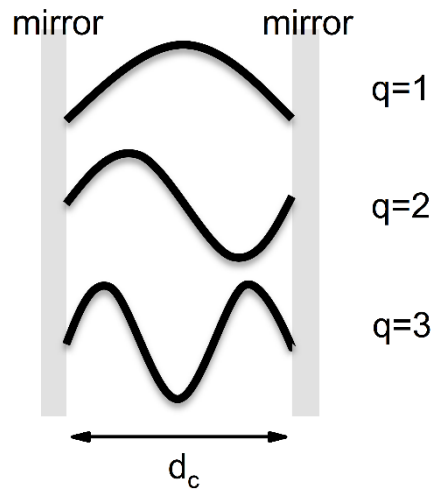


**Figure 2.5.** Schematic of two planar mirrors separated by distance  $d_c$  and confined optical modes of cavity order  $q=1,2,3$ .

In Fabry-Perot resonators, the confinement of photons occurs in a direction perpendicular to the cavity surface. The total wavevector of the confined photons  $k_o$  can be written as

$$k_o = \frac{2\pi}{\lambda_c} \quad (2.8)$$

and combining (2.7) and (2.8), it can be expressed as

$$k_o = \frac{q\pi}{\eta_c d_c} \frac{1}{\cos \theta_{int}} \quad (2.9)$$

The total wavevector can be resolved in its two components  $k_o^2 = k_{\perp}^2 + k_{\parallel}^2$ ; the perpendicular  $k_{\perp}$  and the parallel  $k_{\parallel}$  component as shown in Figure 2.6. In order to obtain constructive interference after one total round-trip between the two mirrors, we can define the wavevector perpendicular to the surface of the cavity using  $k_{\perp} = k_o \cos \theta_{int}$ <sup>7</sup>, and we can write

$$k_{\perp} = \frac{q\pi}{\eta_c d_c} \quad (2.10)$$

For  $\theta_{int} \neq 0$  an additional component, which corresponds to a wavevector parallel to the cavity surface  $k_{\parallel} = k_o \sin \theta_{int}$ , must be taken into account (Figure 2.6). This is expressed as

$$k_{\parallel} = \frac{q\pi}{\eta_c d_c} \tan \theta_{int} \quad (2.11)$$

As it can be seen from Figure 2.6 and Equations 2.10 and 2.11,  $k_{\perp}$  remains fixed with  $\theta_{int}$  while  $k_{\parallel}$  increases with increasing angle, causing the total wavevector to increase with angle too. Equation 2.12 expresses the energy of the cavity mode  $E_c$ , which is proportional to  $k_o$  and increases with angle as follows

$$E_c = \frac{hck_o}{2\pi} = \frac{hcq}{2\eta_c d_c \cos \theta_{int}} = E_o (1 - \sin^2 \theta_{int})^{-\frac{1}{2}} \quad (2.12)$$

All measurements are generally performed with respect to the external viewing angle  $\theta_{ext}$ , therefore by applying Snell's law  $\eta_1 \sin \theta_1 = \eta_2 \sin \theta_2$ , Equation 2.12 can be expressed as a function of  $\theta_{ext}$ . Assuming that the medium outside the cavity is air with a refractive index of  $\eta_{air} = 1$ , the energy of the cavity mode can be written as shown in Equation 2.13

$$E_c = E_o \left(1 - \frac{\sin^2 \theta_{ext}}{\eta_c^2}\right)^{-\frac{1}{2}} \quad (2.13)$$

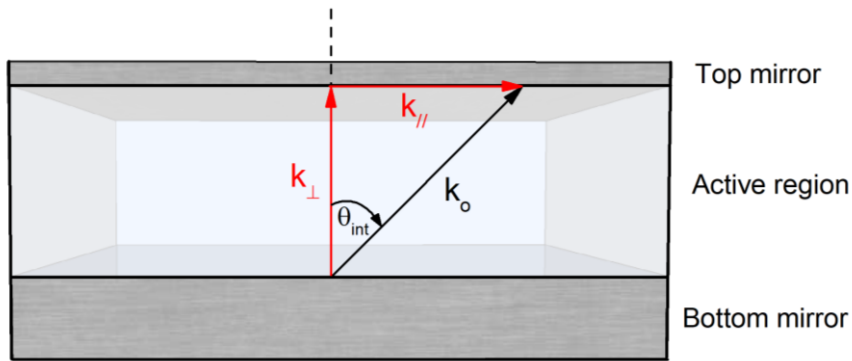


**Figure 2.6.** Schematic of a microcavity showing the total wavevector  $k_o$  along with its perpendicular  $k_{\perp}$  and parallel  $k_{\parallel}$  components at an internal angle  $\theta_{int}$ .

### 2.2.2. Cavity mirrors

The ‘quality’ (vide infra) of the two mirrors defines the quality of the confinement of light in a cavity. An ideal cavity is one that has no absorption or scattering losses and the ‘quality’ is solely dependent on the reflectivity  $R_i$  of the mirrors. The higher the reflectivity of the mirrors, the longer the confinement time of photons within the cavity. The finesse  $\mathcal{F}$  of a cavity is a measure of the ‘quality’ of the cavity and it can be expressed using the reflectivity values  $R_1$  and  $R_2$  of the two mirrors as shown using Equation 2.14.

$$\mathcal{F} = \frac{\pi(R_1 R_2)^{1/4}}{1 - (R_1 R_2)^{1/2}} \quad (2.14)$$

As it can be seen from Equation 2.14, the finesse of a cavity is limited by the mirror with the lowest reflectivity value. Another measure of the quality of a particular cavity mode is the quality factor or  $Q$  factor. The  $Q$  factor can be described by the ratio of  $\lambda_c$  to the full width at half maximum (FWHM) of the mode,  $\Delta\lambda_c$ , at the central wavelength  $\lambda_c$  of the cavity, as well as in terms of energy  $E$  and angular frequency  $\omega$ , as follows

$$Q = \frac{\lambda_c}{\Delta\lambda_c} = \frac{E}{\Delta E} = \frac{\omega}{\Delta\omega} \quad (2.15)$$

Two different optical microcavity configurations can provide confinement of photons for relatively prolonged periods of time, ensuring that the interaction between excitons and photons can occur within the strong or weak coupling regime. In the first configuration, each reflective surface is composed of a metallic layer. The second utilises the total internal reflection at the boundaries of two different dielectric materials. This is termed a distributed Bragg reflector (DBR) and can have very high optical reflectivity.<sup>7</sup>

Metallic mirrors can be used as the two reflective surfaces in Fabry-Perot resonators. A metallic mirror can be thermally evaporated, a process that is easy and allows control of the reflectivity of the mirror via thickness tuning. The reflectivity values of metallic mirrors can be very high at certain wavelengths, however, metallic mirrors suffer losses due to absorption. The reflectivity of silver, aluminium and gold mirrors can be predicted using the refractive index ( $\eta$ ) and extinction coefficient ( $\kappa$ ) in Fresnel equations<sup>8</sup>, and plotted in Figure 2.7.

A DBR is a planar periodically patterned microstructure consisting of alternating layers with each layer having a thickness on the scale of the resonant wavelength. The thickness of each alternating dielectric layer is  $\lambda/4\eta$  where  $\lambda$  is called the Bragg wavelength, and is the desired value for the central wavelength of the DBR high reflectivity region (stopband) and  $\eta$  is the refractive index of the material. DBRs, unlike their metallic counterparts, can provide high reflectivity values with very low losses. Dielectric materials, having a large bandgap compared to conducting metallic materials, are used to provide reflectivity values of >99% and at the same time eliminate losses related to absorption.

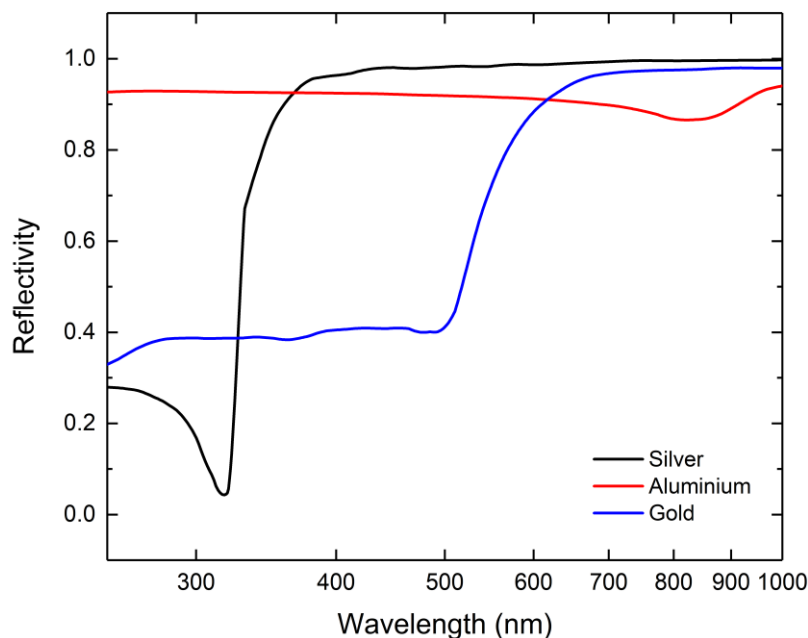


**Figure 2.7.** Reflectivity of silver (black), aluminium (red) and gold (blue) predicted using Fresnel equations and the measured values of the refractive index and extinction coefficient of the materials.<sup>8</sup>

Another advantage of DBRs over metallic mirrors is that their reflectivity can be tailored to match the needs of an experiment by altering the number,  $N$ , of alternating layer pairs, the refractive index contrast,  $\Delta\eta$ , of the two dielectric materials as well as the thickness of each of these layers. Figure 2.8 shows how each material or structural parameter can affect the reflectivity of a DBR using the transfer matrix method (TMM). TMM is described in detail by Hecht.<sup>8</sup> In part (a), the thickness of each layer of the dielectric material is tuned to shift the Bragg wavelength and the stopband of the DBR. Part (b) shows how the number of alternating layer pairs, varied between 2 (low reflectivity) and 12 pairs (high reflectivity), can increase the reflectivity of the DBRs. Figure 2.8 (c) shows the effect of the refractive index contrast between the two dielectric materials when it is tuned from 1.14 up to 1.92, with higher contrast creating a wider DBR stopband. Finally, in part (d), all three values that can be used to control the optical properties of a DBR are summarised.

The reflectivity of a DBR stopband has an angular dependence. In Figure 2.9, a TMM model is used to simulate the angular dependence of transverse electric (TE – where the electric field is perpendicular to the plane of incidence) and transverse magnetic (TM – where the magnetic field is perpendicular to the plane of incidence) reflectivity spectra from a DBR microcavity for angles tuned between  $0^\circ$  and  $70^\circ$ . In the TMM model, the two reflectors comprised of 10 (bottom mirror) and 8 (top mirror) pairs of alternating layers with a refractive index contrast  $\Delta\eta = 1.41$ . The spacing between the two mirrors is assumed to be filled by an optically inert polymer with an effective refractive index of  $\eta_c = 1.59$  in order to create a  $\lambda/2$  cavity with a cavity mode wavelength at normal incidence around the Bragg wavelength of the DBR. Figure 2.10 shows experimental data of the angular dependent reflectivity (between  $10^\circ$  and  $70^\circ$ ) from a cavity having very similar values of  $\Delta\eta$ ,  $\eta_c$  and cavity length to those used in the TMM of Figure 2.9. In both simulated and experimental data, the near-parabolic dispersion of the photon mode described by Equation 2.13 is clearly visible. Figure 2.11 shows a schematic of the DBR microcavity used in the TMM model of Figure 2.9 and the structure used for the reflectivity experiments of Figure 2.10.

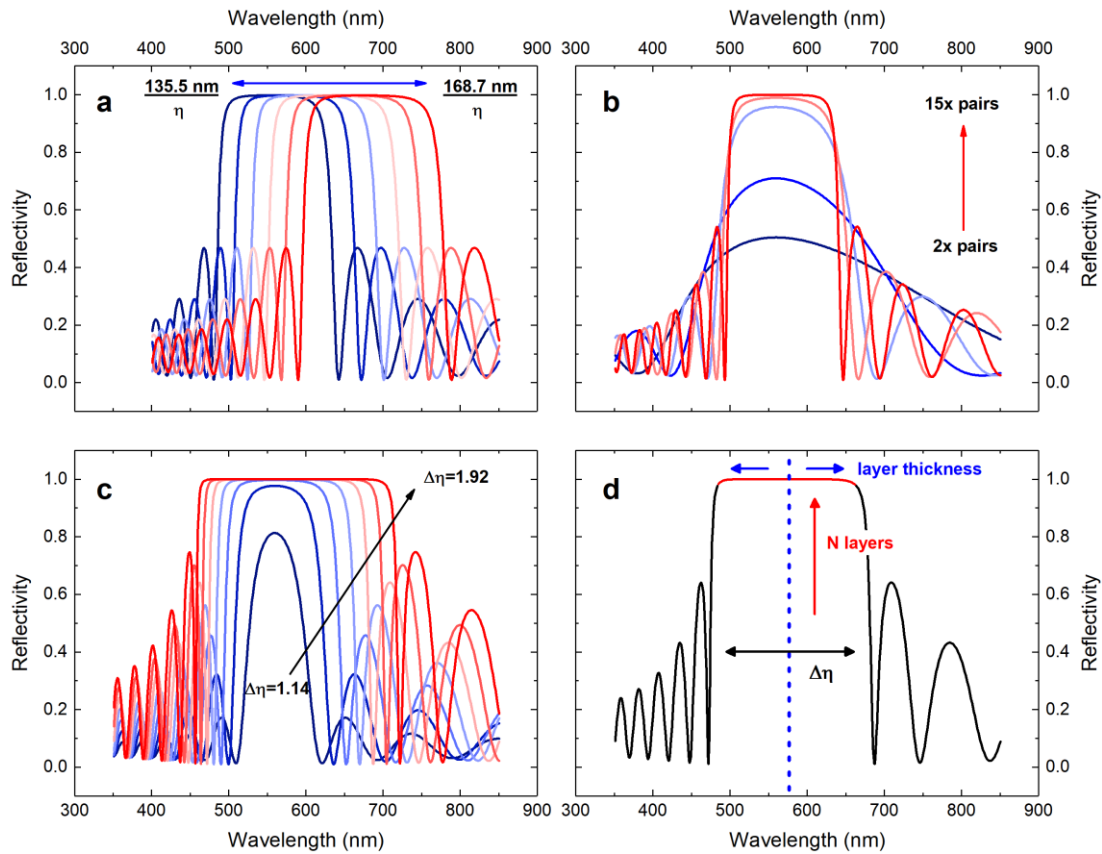


**Figure 2.8.** Simulated reflectivity of a DBR at normal incidence using the TMM for different (a) alternating layer thicknesses, (b) number of alternating layer pairs and (c) alternating layer refractive index contrast. (d) Summary of the design parameters and how they affect the optical properties of the DBR.

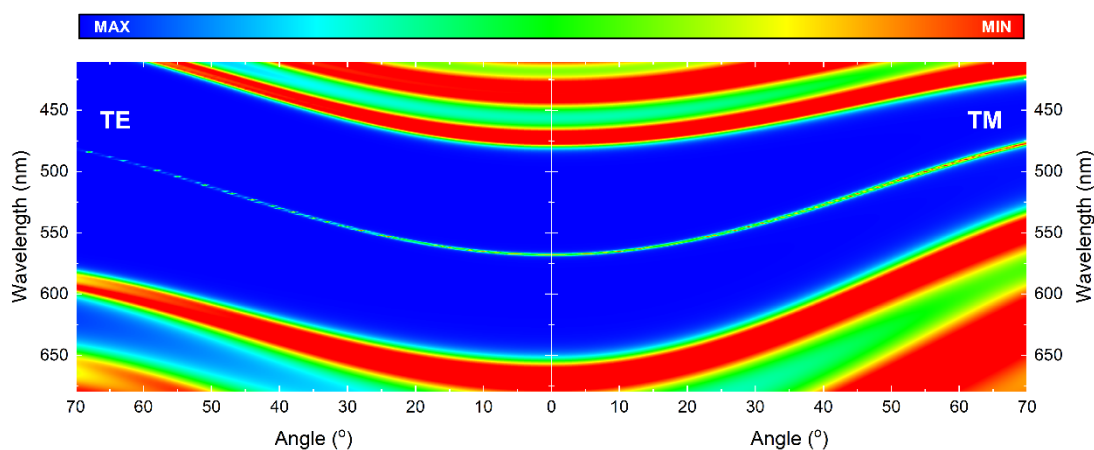


**Figure 2.9.** Simulation of the TE and TM angular reflectivity of a microcavity using the TMM. The min and max intensity of the color scale ranges between 0.1 and 1, respectively. The modelled microcavity consists of 10 pairs of alternating layers (bottom mirror), an optically inert layer of effective refractive index of 1.59 and 8 pairs of alternating layers (top mirror).

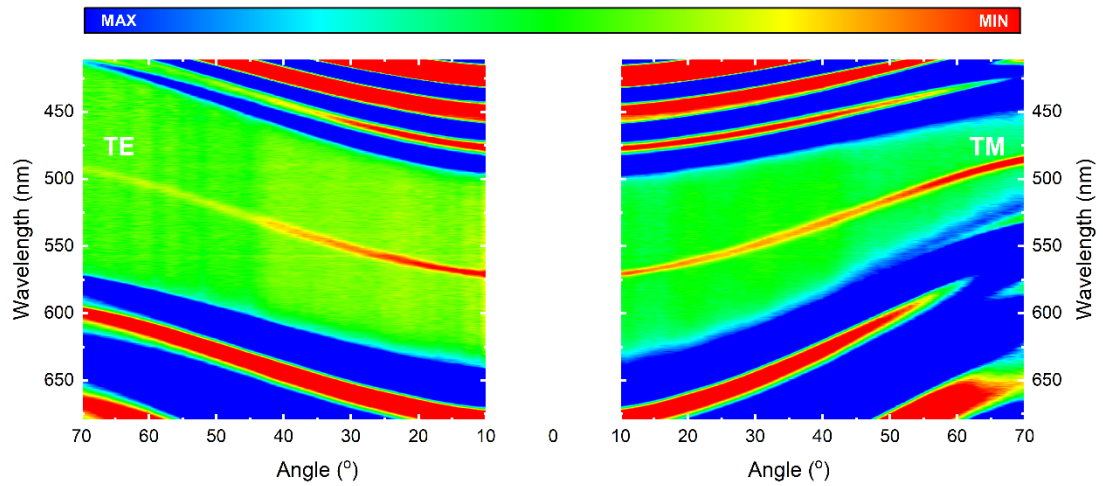


**Figure 2.10.** Experimental TE and TM angular reflectivity measurement of a microcavity. The min and max intensity of the color scale ranges between 0.6 and 1, respectively. The microcavity consists of 10 pairs of alternating layers of  $\text{SiO}_2/\text{Nb}_2\text{O}_5$  (bottom mirror), a thin layer of the optically inert polymer Polystyrene having a refractive index of around 1.59 and 8 pairs of alternating layers of  $\text{SiO}_2/\text{Nb}_2\text{O}_5$  (top mirror).

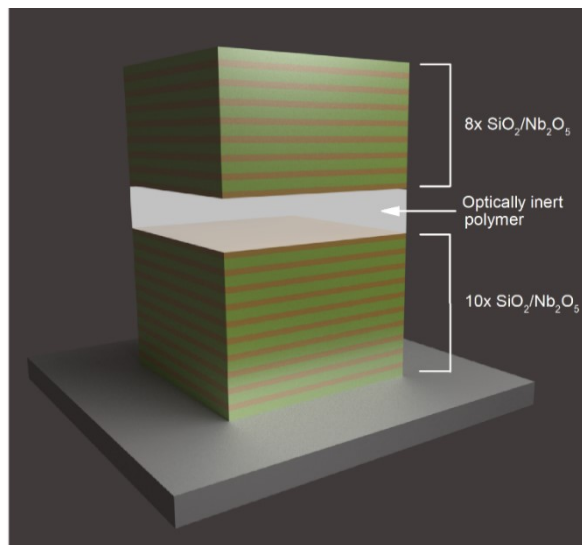


**Figure 2.11.** Schematic of the DBR microcavity used in the TMM model of Figure 2.9 and the experiments of the white light reflectivity of Figure 2.10.

### 2.3. Exciton-polaritons

The physics of planar microcavities and the confinement of photons were introduced in the previous section. Semiconducting materials can be placed between the two

mirrors of a microcavity structure. Light-matter interaction can occur if the electronic transition of the semiconductor is resonant with the energy of the confined photons. There are three parameters that define the strength of light-matter interaction, (i) the rate at which the cavity photons escape the cavity,  $k$ , (ii) the dephasing rate of excitons,  $\gamma$ , and (iii) the exciton-photon coupling constant,  $g_o$ . If  $g_o \ll (k, \gamma)$ , where  $(k, \gamma)$  represents the maximum rate values for  $k$  and  $\gamma$ , the weak coupling regime is realised where the emission of a photon by an exciton is an irreversible process.<sup>9</sup> In weakly coupled cavities, the effect of the cavity is small and therefore the light-matter interaction can be described by perturbation theory. The photon field is modified by the microcavity, which can then enhance spontaneous emission rates through the so-called Purcell effect.<sup>10</sup> This enhancement stems from the fact that the cavity, being resonant with the excitonic transition, enhances the photon density of states at that wavelength. A photon density of final states factor appears in Fermi's Golden Rule as shown in Equation 2.16, where  $\Gamma_{i \rightarrow f}$  is the transition probability of the initial state  $i$  to the final state  $f$ ,  $M_{i \rightarrow f}$  is the matrix element for the transition and  $\rho_f$  is the density of final states. This consequently enhances the radiative emission rate.<sup>7</sup>

$$\Gamma_{i \rightarrow f} = \frac{2\pi}{\hbar} |M_{i \rightarrow f}|^2 \rho_f \quad (2.16)$$

By enhancing the reflectivity of the cavity mirrors (minimising the values of  $k$  and  $\gamma$ ) and by selecting the right semiconducting material (increasing  $g_o$ ) allows us to obtain the requirement for strong coupling, which is  $g_o \gg (k, \gamma)$ .<sup>9</sup> In the strong coupling regime, the emission of a photon by an exciton becomes reversible leading to an oscillatory exchange of energy between light and matter. The energy exchange frequency is called the Rabi frequency,  $\Omega_{Rabi}$ , which describes the light-matter coupling strength. In the strong coupling regime, perturbation theory is not sufficient to describe exciton-photon interactions. Photons and excitons can not be described individually and a new hybrid bosonic quasi-particle, the cavity-polariton, is introduced, which is a linear coherent superposition of the two constituent components.<sup>11</sup>

Cavity-polaritons, hereafter referred to as polaritons, carry properties of both photons and excitons. Polaritons are usually referred to as half-light half-matter quasi-particles and are described by new eigenstates. The exchange of energy between light and matter, although being quantum mechanical in nature, can be described using a classical two-level coupled oscillator. In Equation 2.17,  $E_C$  and  $E_X$  are the energies of the cavity photons and the excitons, respectively, while  $\Lambda$  is their mutual interaction potential. The polynomial Equations 2.18 and 2.19 can be solved using the quadratic formula to give the eigenvalues of the system, where  $I$  is a 2x2 identity matrix. The allowed polariton energy values,  $E$ , can be determined by solving Equation 2.19, the solutions of which are defined in Equation 2.20.

$$A = \begin{bmatrix} E_C & \Lambda \\ \Lambda & E_X \end{bmatrix} \quad (2.17)$$

$$\det(A - EI) = \begin{bmatrix} E_C - E & \Lambda \\ \Lambda & E_X - E \end{bmatrix} \quad (2.18)$$

$$(E_C - E)(E_X - E) - \Lambda^2 = 0 \quad (2.19)$$

$$E = \frac{E_C + E_X}{2} \pm \frac{1}{2} \sqrt{(E_C - E_X)^2 + 4\Lambda^2} \quad (2.20)$$

As it can be seen from Equation 2.20, there are two possible solutions corresponding to two different polariton energies. The cavity photon energy,  $E_C$ , carries an angular dependence as shown by Equation 2.13 and hence the two polariton energies will also have an angular dependence which allows their separation into two branches; the lower polariton branch (LPB) and the upper polariton branch (UPB). The energy difference at normal incidence,  $E_C - E_X$ , is called the photon-exciton detuning,  $\delta$ . In the case of zero photon-exciton detuning, where  $\delta = 0$ , the photon and exciton energies are degenerate at normal incidence and the separation of the LPB and UPB

has the smallest possible value known as the Rabi splitting energy,  $\hbar\Omega_{Rabi}$ . The Rabi splitting energy can be calculated using Equation 2.20, following the requirement  $\delta = E_C - E_X = 0$ , and it is described by Equation 2.21.

$$\hbar\Omega_{Rabi} = 2\Lambda \quad (2.21)$$

In the case where  $\delta < 0$ , known as negative detuning, the photon and exciton energies are degenerate at a higher angle,  $\theta_{res}$ , where the energy difference between the LPB and UPB takes its minimum value corresponding to the Rabi splitting energy. There is a third case, where the photon energy is higher than the exciton energy (positive detuning,  $\delta > 0$ ) with no crossing point between them. The LPB, UPB, photon ( $C$ ), and exciton ( $X$ ) energies are shown in Figure 2.12 (a-c) for three possible detunings.

Polariton branches have an angle dependent photon-exciton mixing fraction that is contained in the eigenvector of  $A$ . The squares of the two mixing coefficients, also known as Hopfield coefficients, give the photonic  $|\alpha_C|^2$  and excitonic  $|\alpha_X|^2$  weightings of the polaritons in the LPB and UPB at each angle. An expansion of Equation 2.22 gives Equations 2.23 and 2.24, which can be solved for  $|\alpha_C|^2$  and  $|\alpha_X|^2$  (Equation 2.25 and 2.26) by taking into account the constraint  $|\alpha_C|^2 + |\alpha_X|^2 = 1$  and eliminating the interaction potential  $\Lambda$  using Equation 2.20.

$$\begin{bmatrix} E_C & \Lambda \\ \Lambda & E_X \end{bmatrix} \begin{bmatrix} \alpha_C \\ \alpha_X \end{bmatrix} = E \begin{bmatrix} \alpha_C \\ \alpha_X \end{bmatrix} \quad (2.22)$$

$$|\alpha_C|E_C + |\alpha_X|\Lambda = |\alpha_C|E \quad (2.23)$$

$$|\alpha_C|\Lambda + |\alpha_X|E_X = |\alpha_X|E \quad (2.24)$$

$$|\alpha_C|^2 = \frac{E_X - E}{E_C + E_X - 2E} \quad (2.25)$$

$$|\alpha_X|^2 = 1 - |\alpha_C|^2 \quad (2.26)$$

In Figure 2.12, parts (d-f) show the Hopfield coefficients of the LPB corresponding to the three different detunings presented in parts (a-c). The Hopfield coefficients of the UPB can be readily extracted by simply switching those of the LPB; namely  $|\alpha_{C,LPB}|^2 = |\alpha_{X,UPB}|^2$  and  $|\alpha_{X,LPB}|^2 = |\alpha_{C,UPB}|^2$ . Generally, strong coupling is manifested through a characteristic anticrossing of the two polariton branches at the resonant angle,  $\theta_{res}$ , at which the photon and exciton energies are degenerate. At  $\theta_{res}$  the polaritons in the LPB and UPB comprised of 50% photon and 50% exciton.

We can generalize the physics of strong coupling between a photonic mode and an electronic transition to a coupling to more than one excitation. For example in the case where two different materials are placed between two mirrors, having electronic transitions which are both resonant with the energy of the confined electric field.<sup>12</sup> Another example is when an organic material has, apart from an electronic transition, a vibronic transition. In this case both excitations can strongly couple if they are resonant with the photonic mode.<sup>13</sup> When describing coupling between a photonic mode ( $C$ ) and two excitations ( $X_1$  and  $X_2$ ), we use a three-level coupled classical oscillator model as shown in Equation 2.27.

$$\begin{bmatrix} E_C & \Lambda_1 & \Lambda_2 \\ \Lambda_1 & E_{X1} & 0 \\ \Lambda_2 & 0 & E_{X2} \end{bmatrix} \begin{bmatrix} \alpha_C \\ \alpha_{X1} \\ \alpha_{X2} \end{bmatrix} = E \begin{bmatrix} \alpha_C \\ \alpha_{X1} \\ \alpha_{X2} \end{bmatrix} \quad (2.27)$$

The system has three unique solutions corresponding to three different polariton branches. Aside from the LPB and UPB, a new branch is now present, termed the middle polariton branch (MPB). The eigenvectors of the system give the Hopfield coefficients of LPB, MPB and UPB. Figure 2.13 (a-f) shows strong coupling between

the photon mode and the two electronic transitions and the characteristic anticrossing between the polariton branches as well as the mixing between the three constituents of the LPB.

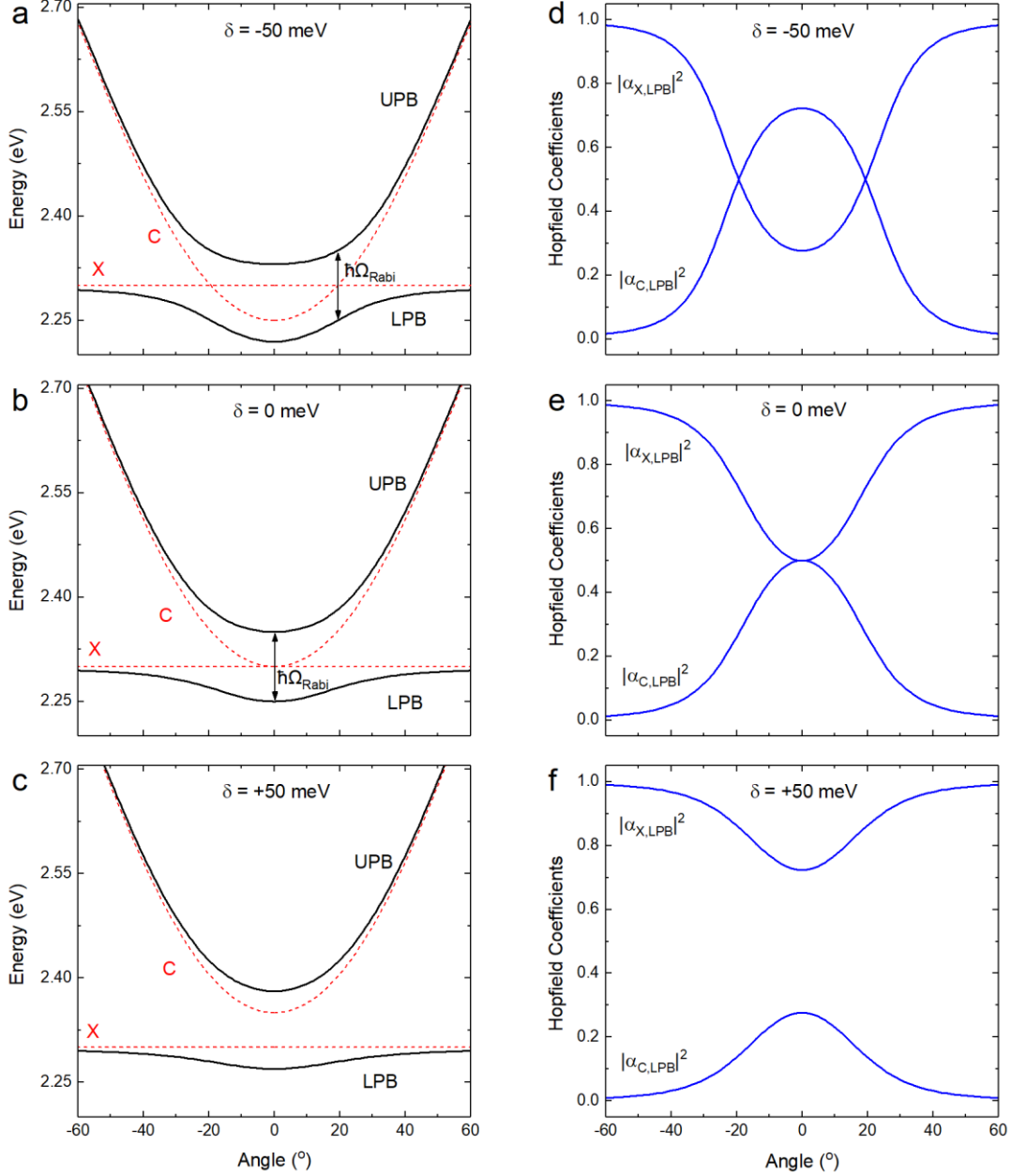


**Figure 2.12.** Lower polariton branch (LPB) and upper polariton branch (UPB) energies (black lines) along with photon (C) and exciton (X) energies (red dashed lines) with angle for a cavity with (a) negative detuning  $\delta=-50$  meV, (b) zero detuning  $\delta=0$  meV and (c) positive detuning  $\delta=+50$  meV. Hopfield coefficients of the LPB describing the photonic  $|\alpha_{\text{C,LPB}}|^2$  and the excitonic  $|\alpha_{\text{X,LPB}}|^2$  fractions of the branch at different angles for (d)  $\delta=-50$  meV, (e)  $\delta=0$  meV and (f)  $\delta=+50$  meV.

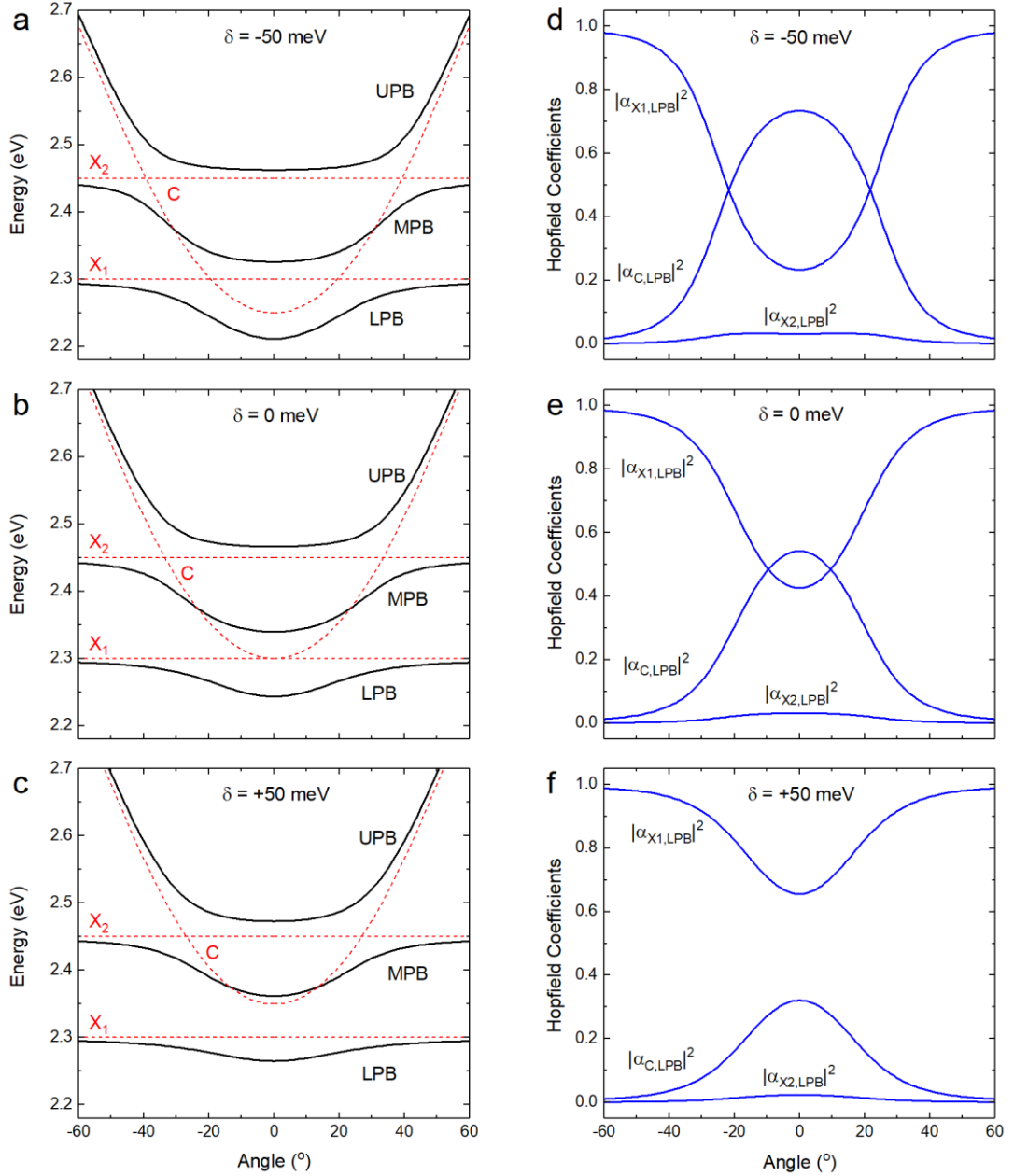


**Figure 2.13.** Lower polariton branch (LPB), middle polariton branch (MPB) and upper polariton branch (UPB) energies (black lines) along with photon (C) and exciton (X) energies (red dashed lines) with angle for a cavity with (a) negative detuning  $\delta=-50$  meV, (b) zero detuning  $\delta=0$  meV and (c) positive detuning  $\delta=+50$  meV. Hopfield coefficients of the LPB describing the photonic  $|\alpha_{C,LPB}|^2$  and the two electronic  $|\alpha_{X1,LPB}|^2$ ,  $|\alpha_{X2,LPB}|^2$  fractions of the branch at different angles for (d)  $\delta=-50$  meV, (e)  $\delta=0$  meV and (f)  $\delta=+50$  meV.

Generally, the classical coupled oscillator model can be used to describe the coupling between an infinite number of oscillators involved in the cavity as shown in Equation 2.28. Different structure designs allow one excitation to couple to two interacting

photonic modes in the case of coupled cavities<sup>14</sup> or very thick cavities containing many high order cavity modes resonant with an excitation.<sup>15</sup>

$$\begin{bmatrix} E_1 & \cdots & \Lambda_{n-1} \\ \vdots & \ddots & \vdots \\ \Lambda_{n-1} & \cdots & E_n \end{bmatrix} \begin{bmatrix} \alpha_1 \\ \vdots \\ \alpha_n \end{bmatrix} = E \begin{bmatrix} \alpha_1 \\ \vdots \\ \alpha_n \end{bmatrix} \quad (2.28)$$

## 2.4. Polariton condensates and lasers

Lasers are devices emitting coherent monochromatic light induced by stimulated emission of photons from atoms or molecules. They find applications in every aspect of life, i.e. CD/DVD players at home, local fast communications networks and medicine. They usually utilise inorganic semiconductors that are either (i) embedded between two reflectors in the configuration of vertical-cavity surface emitting lasers (VCSELs) or (ii) periodically structured as a diffraction grating in the configuration of a distributed feedback (DFB) laser. Both types of lasers create a cheap and low-energy consumption device for all sorts of applications, particularly in photonics. The basic principle of operation is that of population inversion, namely the number of electrons that exist in the conduction band must be larger than the number of electrons in the valence band. Spontaneous emission of a photon will then induce stimulated emission of other photons having the same phase and energy, which leads to light amplification (see Figure 2.14). Each of the three processes shown in Figure 2.14 (absorption, spontaneous emission and stimulated emission) are related to the so-called Einstein coefficients. The Einstein A coefficient is related to the rate of spontaneous emission and the Einstein B coefficients are related to the rate of absorption and stimulated emission. A population inversion (Figure 2.14 (b)) can be obtained by optical or electrical injection; however, this prerequisite can result in conventional lasers having a large operational threshold. As is discussed below, polariton lasers have the advantage over conventional photon lasers as they do not require a population inversion, and thus the injection density needed to reach lasing threshold can be two orders of magnitude lower.<sup>16</sup>

The condensation of bosonic particles is based on their indistinguishability. This means that, unlike fermions which are restricted by Pauli's exclusion principle, bosons can arbitrarily occupy the same quantum state. When the occupation of the lowest bosonic quantum state exceeds unity, a final state bosonic stimulation occurs which is a key feature of condensation (see Figure 2.15). As a result of Bose-Einstein statistics, the rate by which bosons scatter to a final state containing  $N$  particles is  $N+1$ . Polaritons, being bosonic quasi-particles, can thus occupy the same quantum state at the bottom of their dispersion at zero in-plane momentum which forms a trap in momentum space. If sufficient polaritons scatter to this momentum trap, they can be described using a single wavefunction and form a macroscopic quantum condensate, also known as a non-equilibrium polariton Bose-Einstein Condensate (BEC). The luminescence from this polariton decay via photon emission is a form of lasing, as the spontaneously emitted photons all carry the same energy, phase and momentum as the condensate.

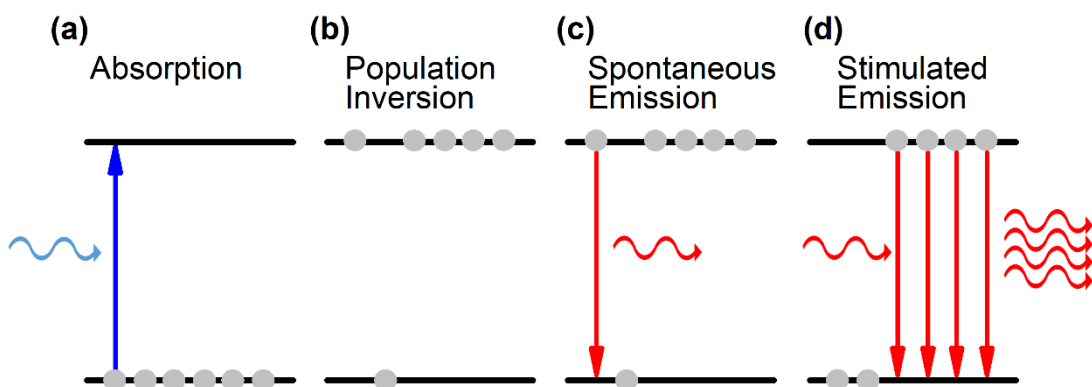


**Figure 2.14.** Photon lasing process. (a) Absorption of a photon and promotion of an electron from the ground state to the excited state. (b) Population inversion where the number of electrons in the excited state is larger than the number of electrons in the ground state. (c) Spontaneous emission of a photon following the decay of the electron from the excited state to the ground state. (d) The spontaneous emission of a photon induces stimulated emission of other photons having the same phase and energy.

Each and every particle has a wave associated with it. The so-called de Broglie wavelength of a particle,  $\lambda_{dB}$ , is related to its momentum,  $p$ , as defined in Equation 2.29. The thermal wavelength of a particle in a gas is therefore given by Equation 2.30,

considering that the momentum of a particle at the peak of the Maxwell-Boltzmann distribution is  $\sqrt{(2mK_B T)}$ , where  $K_B$  is the Boltzmann constant and  $T$  is the temperature of the gas.

$$\lambda_{dB} = \frac{h}{p} \quad (2.29)$$

$$\lambda_{dB} = \sqrt{\frac{2\pi\hbar^2}{mK_B T}} \quad (2.30)$$

As it can be seen from Equation 2.30, the de Broglie wavelength of such particles is inversely proportional to both their mass and temperature. At high temperatures, the particles in a gas have much kinetic energy and therefore elastically scatter from one another. When the temperature is reduced below a critical temperature,  $T_c$ , the kinetic energy is small and the thermal de Broglie wavelength becomes comparable to the distance between neighbouring particles, causing their wavefunctions to overlap. The particles then undergo a phase transition where they all occupy the same macroscopic quantum state and are described by a single wavefunction forming a BEC (see Figure 2.16). The critical temperature at which condensation occurs,  $T_c$ , can be calculated by considering the condensation particle density,  $n\lambda_{dB}^3 = 2.612$ .

$$T_c = \frac{2\pi\hbar^2}{mK_B} \left[ \frac{n}{2.612} \right]^{\frac{2}{3}} \quad (2.31)$$

From Equation 2.31, it is clear that in order to increase the critical temperature of condensation, the mass of the particles should be reduced and at the same time, their density should be maximized. Polaritons inherit their light mass (many orders of magnitude lighter than atoms and electrons) from their photonic component and therefore it is obvious that they can undergo condensation at much higher temperatures compared to ultra-cold atomic gases. An important further difference between cold

atomic-gas condensates and polariton condensates is that the latter are intrinsically non-equilibrium systems due to very short polariton lifetimes. Polariton condensates can be described theoretically using mean field theory. In particular, a generalized Gross-Pitaevskii equation (GPE) describing the macroscopic wave function including loss and amplification terms is often used to model such non-equilibrium systems.<sup>17</sup> To account for the non-equilibrium nature of such condensates it is also necessary to include dissipation and pumping terms that are coupled to a rate equation that describes the incoherent reservoir that populates the polariton states.<sup>17</sup>

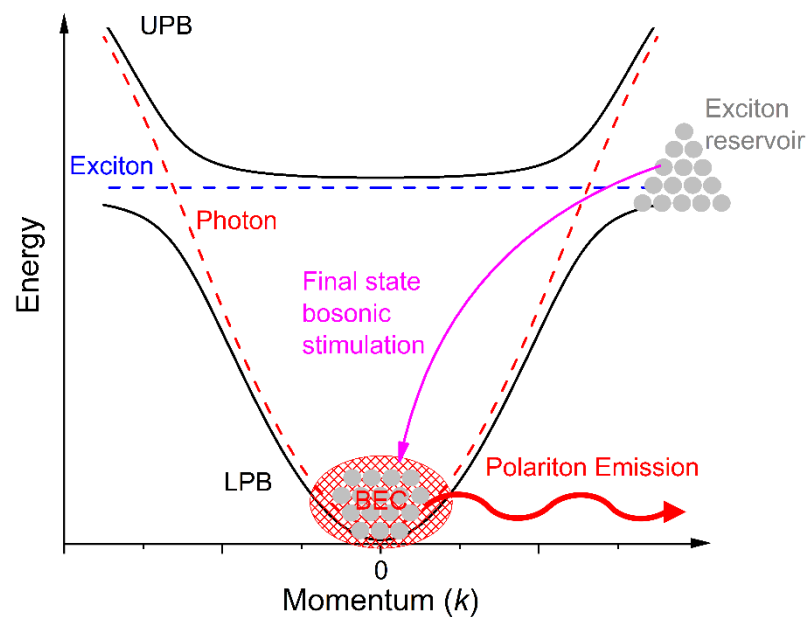


**Figure 2.15.** Exciton-polariton condensation process. When the occupation of the lowest bosonic state ( $k = 0$ ) exceeds unity, final state bosonic stimulation occurs (magenta line). A polariton BEC is formed at the energy trap ( $k = 0$ ).

Both atomic gas BECs and polariton condensates exhibit high degree of spatial coherence, which is a signature of a macroscopically occupied quantum state. The most common way to evaluate the first order spatial coherence of a polariton condensate is by interferometric measurements. A modified Michelson's interferometer equipped with a retroreflector is usually used for these measurements. Above condensation threshold, mirror-symmetric points possess a phase that have a fixed relation, resulting in a high degree of spatial coherence. A typical image of an

interferometric measurement using a modified Michelson's interferometer in the mirror-retroreflector configuration is shown in Figure 2.17. In both parts (a) and (b) it can be seen that the visibility of the fringes is high. The coherence length of the condensate can be estimated by fitting a cross-section through the image with a modulated Gaussian function as will be discussed in more detail in Chapter 4. Part (b) demonstrates the spontaneous formation of a pair of vortices in the condensate. Here, the two forklike dislocations, seen in the fringes, are symmetrically located around the retroreflector axis.<sup>18</sup> Such vortices form spontaneously when there is a rapid transition from incoherent to coherent phases and are pinned onto defects in the sample.<sup>19</sup>

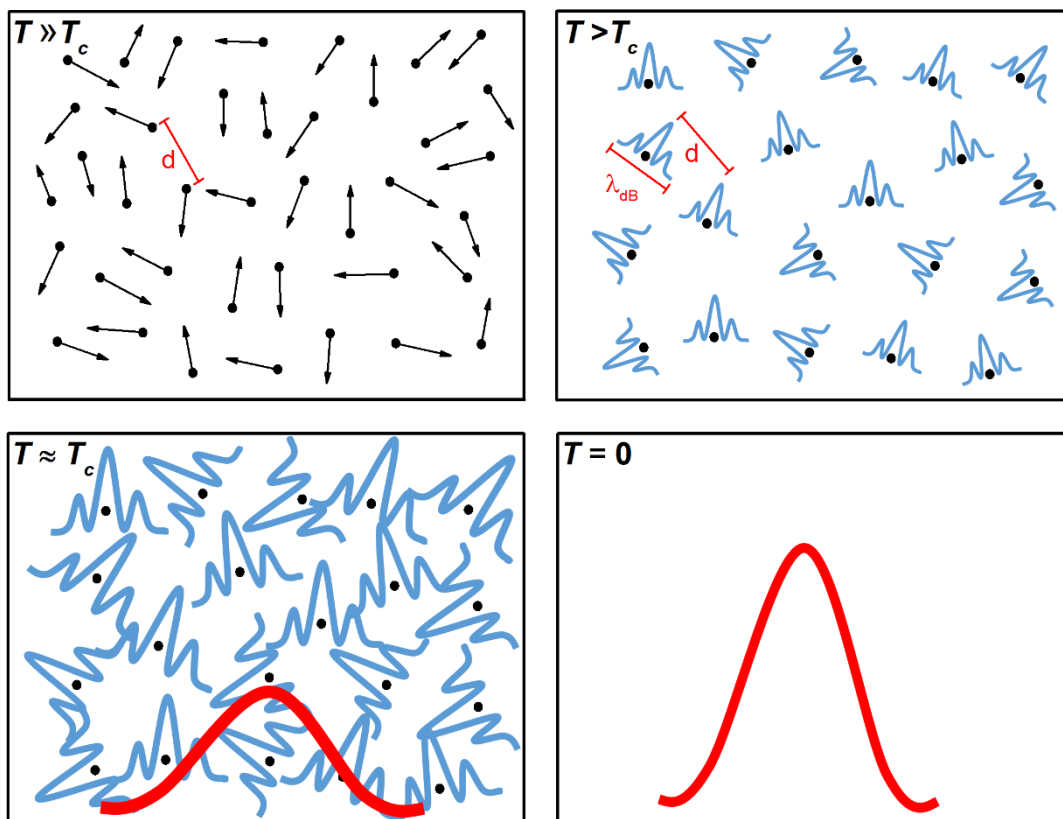


**Figure 2.16.** Particles in a gas. At high  $T$ , where  $T \gg T_c$ , the distance between neighboring particles is large and the particles have a large amount of kinetic energy which leads to elastic scattering. At low  $T$ , where  $T > T_c$ , the particle de Broglie wavelength becomes comparable to the inter-particle distances and particles can be described as wavepackets. When  $T = T_c$ , the particle wavefunctions start to overlap and condensation occurs. At  $T = 0$ , all particles are described by a single wavefunction and form a condensate.

Although the first demonstration of strong light-matter interactions and formation of polaritons in planar microcavities was achieved in 1992<sup>11</sup>, Bose-Einstein condensation of cavity-polaritons was not realised until 2006.<sup>20</sup> This demonstration stimulated much research in this area with many interesting findings underpinning the fascinating physics of polariton condensates.<sup>15,18,21–28</sup>

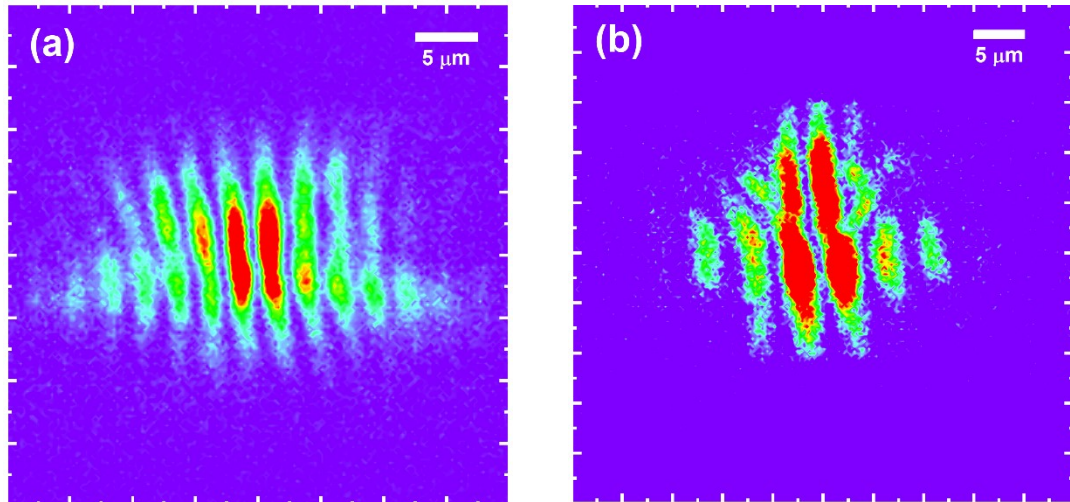


**Figure 2.17.** (a) Interferogram of a polariton condensate. (b) Interferogram of a polariton condensate showing the spontaneous formation of vortices.

## 2.5. Strong coupling in planar microcavities: A historical review

The interaction between light and matter is a prerequisite for all known optical processes, i.e. it gives rise to absorption, spontaneous emission and stimulated emission. Generally, such weak interactions of the electromagnetic field with matter do not significantly modify the electronic transitions of the atoms or molecules involved, and can be approximated by perturbation theory. In the case of strong light-matter interactions, this approximation is not valid and the photonic and matter components must be hybridised with each other to form a new quasiparticle, the so-called polariton. Polaritons were experimentally realised for the first time in bulk ZnO crystals in 1965 by Hopfield.<sup>29</sup> Interestingly, polaritons can occur naturally in bulk crystalline semiconductors and molecules,<sup>29,30</sup> however, in order to be observed they must travel to the surface of the bulk material resulting in the loss of their polaritonic

nature.<sup>31</sup> Planar microcavities are favourable for the study of strong coupling and polaritonic effects because they allow the photonic component of polaritons to escape through the mirrors and then be ‘interrogated’ through photoluminescence, carrying information about their polaritonic properties (i.e. energy, momentum, phase, spin). The first demonstration of strong coupling in a Fabry-Perot microcavity was made by Weisbuch in 1992.<sup>11</sup>

The observation of strong coupling in planar microcavities containing inorganic semiconducting materials was a stepping-stone toward many significant developments. In 2000, polariton parametric amplification and photoluminescence were observed<sup>32,33</sup> and a few years later, Bose-Einstein condensation (BEC) and lasing of polaritons was achieved following laser excitation.<sup>20,21,34–36</sup> Electrically driven polariton lasers have been also demonstrated,<sup>37,38</sup> with novel structural designs allowing for room-temperature operation.<sup>39</sup> BECs are an exotic state of matter and have resulted in the demonstration of many interesting many-body quantum phenomena in inorganic semiconductor polaritonic systems, such as superfluidity and spontaneous formation of quantum vortices.<sup>18,19,23,40</sup> Recently, a number of authors have suggested that polariton condensates can be used in practical applications,<sup>41–43</sup> for example complex multivariable problems can be simulated using arrays of polariton condensates.<sup>44</sup>

Wannier-Mott excitons, found in inorganic semiconductors,<sup>45</sup> have small binding energies (1-10 meV), as a result of screening caused by large dielectric constants, which reduces the coulombic interactions between electrons and holes. Therefore, excitons in inorganic semiconductors suffer thermal dissociation and the strong coupling regime can only be realized, in many cases, at cryogenic temperatures. Frenkel-like excitons in organic semiconductors,<sup>46</sup> have larger binding energies (0.1-1 eV) and therefore are relatively smaller and more localised. This allows Frenkel excitons to be stable at room temperature, which is a necessary requirement for practical applications. While room-temperature emission from weakly coupled organic semiconductor microcavities was studied extensively,<sup>47–53</sup> it was only in 1998 that Lidzey et al. demonstrated strong coupling in a planar microcavity containing an organic semiconductor.<sup>54</sup> In this work, a porphyrin molecule was placed in the spacing between a DBR and a metallic mirror and was coupled to the confined electromagnetic field at room temperature. A maximum Rabi splitting energy of 160 meV was

reported, which at the time was one order of magnitude larger than those observed in II-VI quantum-well microcavities<sup>55</sup> and more than 30 times those reported in microcavities containing III-V quantum-wells.<sup>11,56,57</sup> Later on, larger Rabi splitting energies were reported in organic semiconductor microcavities ( $\sim 0.4$ - $1.1$  eV)<sup>58-60</sup> which in some cases classify the system as operating in the ultra-strong coupling regime.<sup>61</sup> Note that in the original observation of strong coupling by Lidzey et al., polariton emission was absent because the photonic mode was strongly coupled to the non-radiative Soret band, with excitons rapidly relaxing to the lower-lying q-band, depleting emission from polaritonic states.<sup>54</sup> In a second follow-on paper, Lidzey et al. showed that room-temperature polariton photoluminescence could be emitted from a strongly coupled organic microcavity containing a J-aggregated cyanine dye.<sup>62</sup> White-light reflectivity and photoluminescence from a strongly coupled J-aggregate containing microcavity is shown in Figure 2.18.<sup>62</sup>

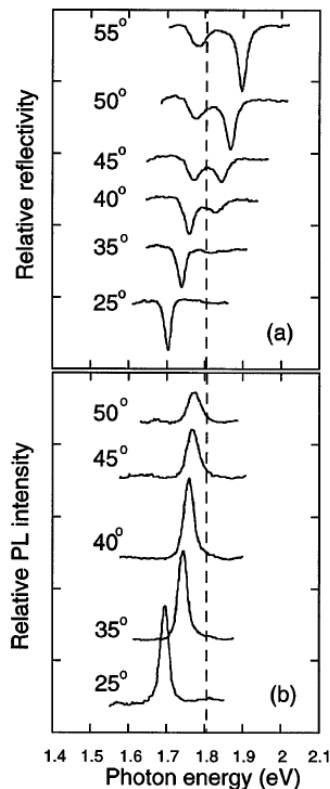


**Figure 2.18.** (a) Reflectivity and (b) photoluminescence emission from a strongly coupled microcavity containing a cyanine dye. Spectra were recorded at different viewing angles. Figure taken from Lidzey et al.<sup>62</sup>

### 2.5.1. Polariton lasing

Advancements in organic semiconductor microcavities followed those in inorganic microcavities, with the first demonstration of organic polariton lasing at room temperature reported in 2010.<sup>24</sup> Here, Kéna-Cohen and Forrest placed a melt-grown single crystal of anthracene between two DBRs, and following optical excitation they observed polariton lasing.<sup>24</sup> Organic polariton BECs were also reported by Plumhof<sup>25</sup> and Daskalakis<sup>26</sup> almost simultaneously in 2014 as shown in Figures 2.19 and 2.20. In the first paper, a ladder conjugated-polymer was sandwiched between two highly reflective mirrors and in the latter, a fluorene oligomer was used as the organic semiconducting material. In both cases, the authors reported a polariton energy blueshift and a high degree of spatial coherence, which is thought to be a “smoking

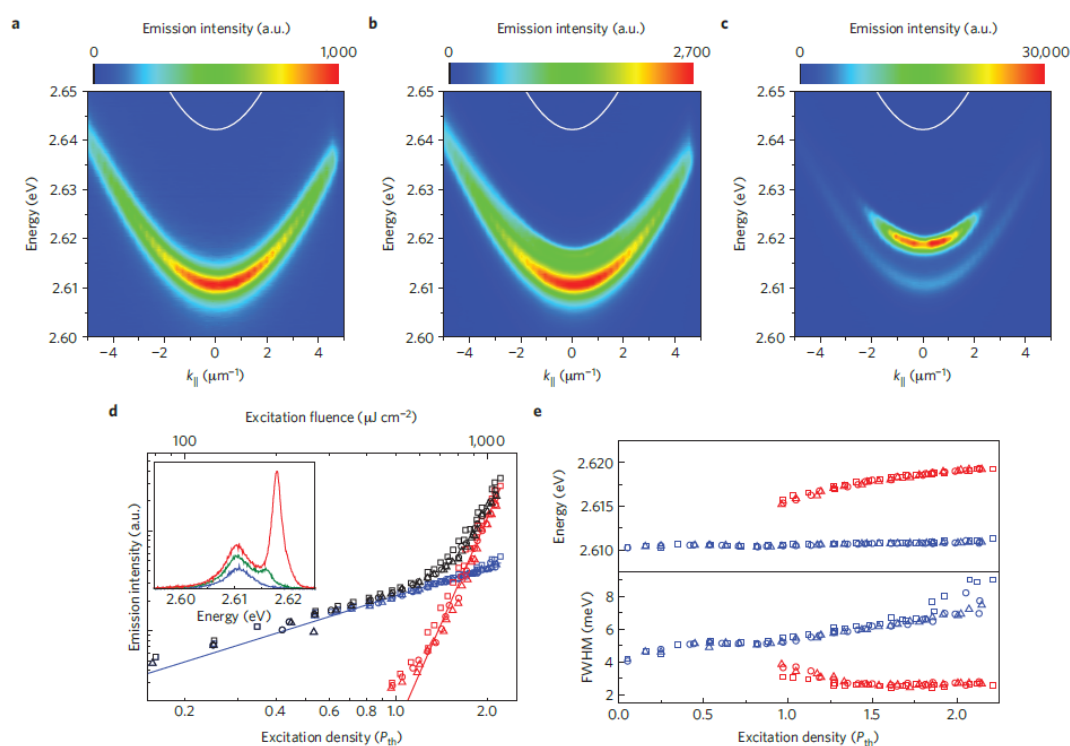


**Figure 2.19.** Time-integrated polariton emission for laser excitation densities (a) below, (b) near and (c) above threshold. (d) Non-linear increase in the photoluminescence emission with excitation density (inset: emergence of a second peak above threshold corresponding to a polariton condensate). (e) Energy blueshift of the condensate emission and decrease of the linewidth above threshold. Figure adapted from Plumhof et al.<sup>25</sup>

gun” for polariton condensation.<sup>25,26</sup> More demonstrations followed,<sup>15,27,63</sup> with work by Diedrich et al. showing polariton lasing in a strongly coupled microcavity filled with a Green Fluorescent Protein. In this work, a transition from the strong to weak coupling regime at high excitation densities resulted in conventional photon lasing.<sup>15</sup>

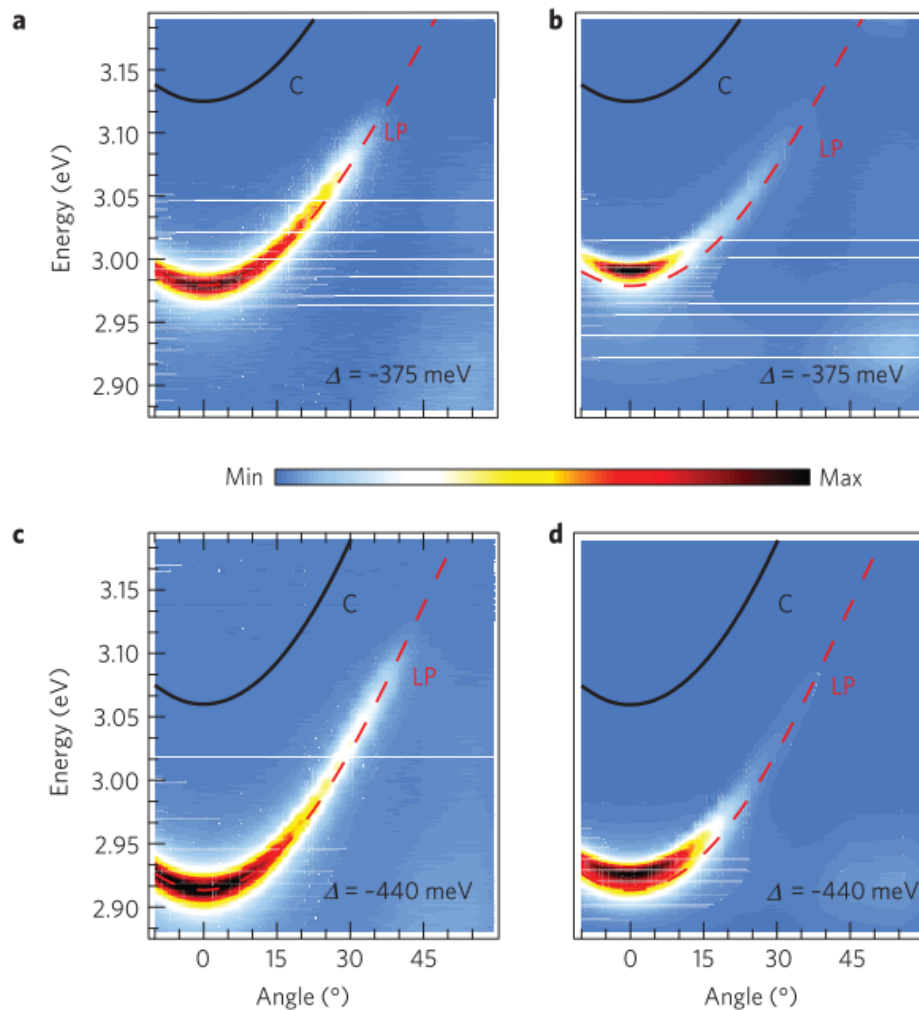


**Figure 2.20.** Polariton photoluminescence emission for low pump fluence (below threshold) for detunings of (a)  $\Delta=-375$  meV and (c)  $\Delta=-440$  meV. Polariton photoluminescence emission above threshold showing the energetic collapse of the emission to the polariton ground state for detuning of (b)  $\Delta=-375$  meV and (d)  $\Delta=-440$  meV. Figure adapted from Daskalakis et al.<sup>26</sup>

Although organic polariton LEDs have been reported by a number of authors,<sup>64–66</sup> electrically injected polariton lasing and condensation in organic semiconductor

microcavities remains elusive due to low charge-carrier mobilities and carrier-related loss mechanisms.<sup>43</sup> Promising steps toward this direction have been recently made, when Graf et al. reported room-temperature electroluminescence from a strongly-coupled microcavity containing single-walled carbon nanotubes.<sup>67</sup>

### 2.5.2. *New effects in organic microcavities*

In addition to allowing the study of interesting many-body quantum phenomena, strong coupling can be also used in the linear regime to generate new effects. For example, by placing two different organic semiconductors in a microcavity having an excitonic energy separation that is commensurate with the typical Rabi splitting energy, the confined optical mode can be used to hybridize both excitations.<sup>12</sup> The three new resultant hybrid polariton states (LPB, MPB and UPB) are described as admixtures of all three constituents (see Figure 2.21).<sup>12</sup> Here, it has been shown that such hybridisation can be used to drive energy transfer between the different organic materials,<sup>12,68,69</sup> even if they are spatially separated by a significant distance.<sup>70,71</sup>

A number of authors have also explored the direct strong coupling of a cavity photon to the infra-red active vibrational transitions of a series of molecular materials.<sup>72–75</sup> Here, it has been predicted that the hybridization of an optical resonance with a vibrational mode associated with a chemical bond may weaken the strength of the bond, leading to a modification of the ground-state energy landscape.<sup>72</sup> By using such an approach in a liquid phase, it is hoped that such bond softening could be used to modify targeted chemical reactions.<sup>73</sup>

### 2.5.3. *The importance of the exciton reservoir*

The photophysics of organic semiconductor microcavities are dominated by the exciton reservoir (ER). The concept of the ER is generally used to describe an ensemble of excitons that remain uncoupled or weakly coupled to the confined photonic mode. The existence of an exciton reservoir is at present an active field of research, and its validity is still a matter of debate. The ER is thought to consist of uncoupled molecular excitations that are of the same nature as those undergoing strong

coupling.<sup>76</sup> The maximum density of states in the ER is usually energetically located around the bare uncoupled exciton energy and the properties of the ER are material- and possibly sample-dependent.<sup>77</sup> It has been shown that scattering from such uncoupled states to polariton states, and vice versa, is assisted by absorption or emission of a molecular vibrational quanta.<sup>78-82</sup> It is also possible, in materials with strong vibronic replicas, to have an ER which radiatively pumps polariton states, with this process being mediated by vibronic states.<sup>24,83,84</sup> The concept of an ER is in fact similar to the picture of excitons that exist at high wavevector in inorganic semiconductor microcavities that limit the relaxation process.<sup>85</sup>

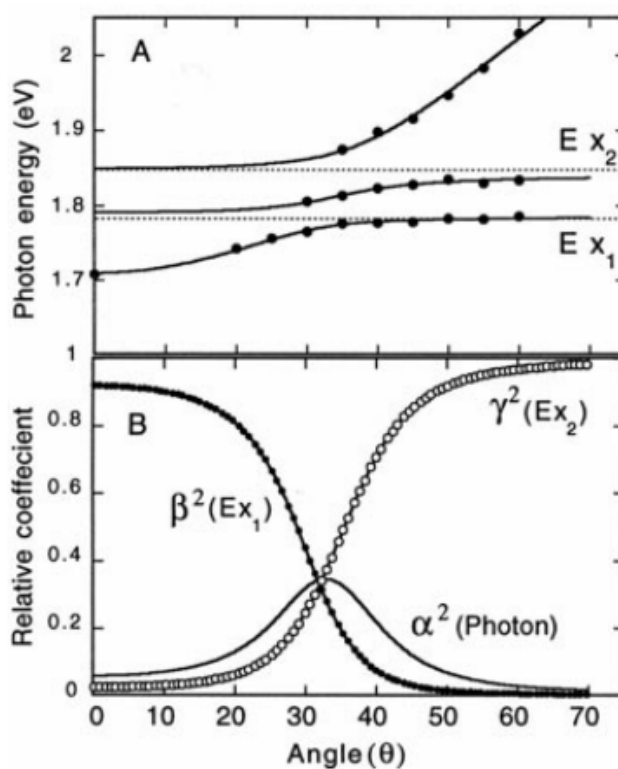


**Figure 2.21.** (a) White-light reflectivity data along with a fit using a three-level coupled oscillator model for a cavity containing two different molecular J-aggregates coupled to the same cavity mode. (b) Hopfield coefficients of the middle polariton branch as calculated from the coupled oscillator model showing that the hybrid polariton state is an admixture of all three constituents. Figure taken from Lidzey et al.<sup>12</sup>

Early work by Lidzey et al. studied the emission from a strongly coupled microcavity containing molecular J-aggregates.<sup>86</sup> They showed that following non-resonant excitation, an ER was created which then populated coherent polaritonic states. A rate model was used to demonstrate that polaritons in the UPB could scatter to the LPB faster than the radiative rate of polaritons, depleting most of the emission from the UPB. Therefore the majority of emission came from the LPB. It was argued that the rate of scattering from the UPB to LPB is proportional to both exciton fractions of the initial and final states and their model agreed with the experimental results. They also suggested that a reservoir of incoherent exciton states could populate polariton states, with the efficiency of this process being proportional to the exciton fraction of the final state. This is a one-way process because the radiative rate of polaritons is high and it is more likely to emit a photon rather than scattering back to the ER. In both processes (inter-branch scattering and reservoir-to-polariton scattering) the emission or absorption of a vibration quanta is a prerequisite to ensure conservation of energy and momentum.<sup>86</sup> While the concept of reservoir-to-polariton has been demonstrated experimentally,<sup>82</sup> the inter-branch population transfer process has not yet been evidenced by experiments although it is known that upper branch polaritons are able to rapidly scatter back to the exciton reservoir.<sup>87</sup>

An early theoretical paper by Agranovich et al. investigated the optical properties of cavity polaritons in microcavities containing disordered organic semiconductors using a macroscopic model.<sup>88</sup> Here, it was shown that microcavities filled with molecular J-aggregates could support the coexistence of two different excitations; namely coherent states (cavity-polaritons) and incoherent states. It was concluded that coherent polariton states exist only in certain restricted intervals where the wavevector is a good quantum number; i.e. the wavevector ( $k$ ) was much greater than the wavevector broadening ( $\delta k$ ). States that did not have well-defined wavevectors were regarded as being incoherent. Here, states located at very small wavevectors on the LPB ( $k \rightarrow 0$ ), can be regarded as incoherent, although they still have polaritonic nature. However, at higher  $k$ , LPB states were considered to be uncoupled to the cavity photon, and were similar in nature to excited states found in a non-cavity film. Considering this picture, exciton and polariton relaxation processes were investigated.<sup>88</sup> Non-resonant laser excitation was used to create states that were mainly incoherent, forming an ER. Any polariton states created on the UPB quickly relaxed (time-scale of 50 fs) into the ER

which exists at an energy similar to that of the bare exciton. Photoluminescence from such incoherent states in the ER pumped the coherent polariton states of the LPB and the UPB. The fast relaxation of the UPB polaritons into incoherent states was expected to cause an imbalance in the emission intensity between the two polariton branches, with more intense emission coming from the LPB. Although this paper focused on microcavities based on J-aggregated molecular dyes, it has been suggested that other disordered and crystalline organic semiconductor systems also support the coexistence of coherent and incoherent states with similar relaxation and polariton population mechanisms.<sup>88</sup> The arguments about the coexistence of coherent and incoherent states were later substantiated using a microscopic approach.<sup>76</sup>

Another theoretical paper concluded that coherent and incoherent states can coexist in a microcavity.<sup>80</sup> Here, they showed that following non-resonant laser excitation, an incoherent ER was formed which then populated coherent polariton states by two principal processes (see Figure 2.22). In the first, incoherent states in the ER optically pumped polaritons in the LPB and UPB. In the second, emission of intermolecular vibrations assisted uncoupled exciton states within the ER to scatter into coherent polariton states; here it is critical that the Rabi splitting energy is on the order of a Raman-active mode in the semiconducting material, creating an efficient relaxation route.<sup>80</sup> Following this, Michetti and La Rocca introduced a model that described the photoluminescence intensity from the LPB and UPB in such microcavities.<sup>78,79</sup> It was found that scattering of reservoir excitations to the UPB is subject to thermal activation<sup>78,79</sup> and that the bottleneck effect strongly depends on the Rabi splitting energy.<sup>79</sup>

It has been shown that incoherent ER states are not always those that undergo strong coupling to light and that the efficiency by which they populate polariton states (by optical pumping) is directly related to the photonic component of the polaritons.<sup>77</sup> Indeed, Lodden and Holmes exploited this effect and incorporated an additional weakly coupled emitter into a strongly coupled microcavity and thus engineered the structure of the ER.<sup>89</sup> Using photoluminescence and electroluminescence measurements, they showed that weakly coupled excitons of the emitter could radiatively pump polariton states in the upper and lower branch.<sup>89</sup> This approach offers an efficient polariton population mechanism in systems where the polariton states

cannot be populated because uncoupled excitons rapidly relax to lower-lying non-emissive states.<sup>54,71</sup>

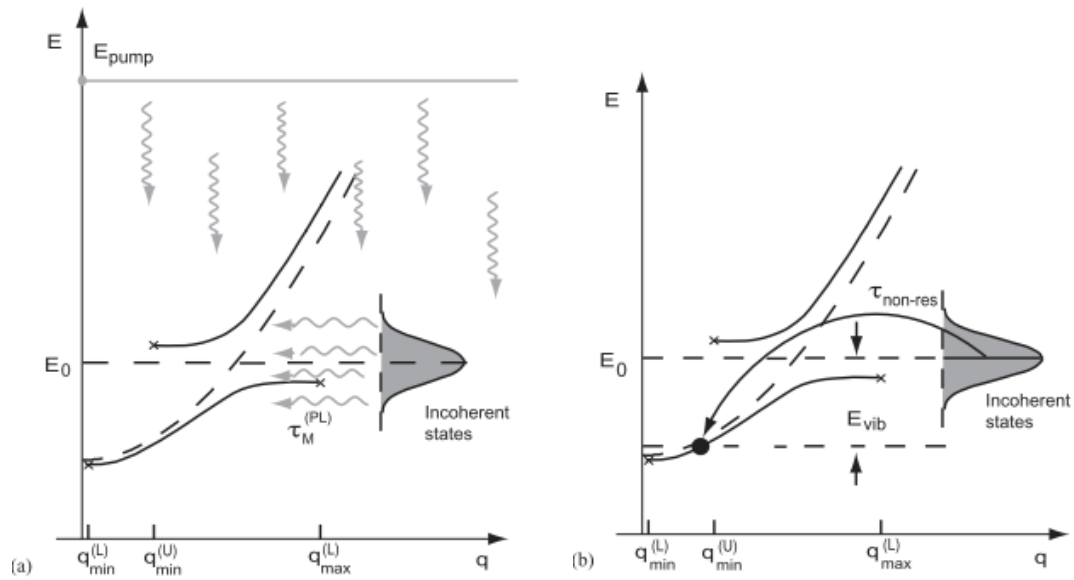


**Figure 2.22.** Schematic representation of possible relaxation processes in a microcavity. (a) Non-resonant excitation and relaxation to an incoherent exciton reservoir. Luminescence from incoherent states in the reservoir pumps coherent polaritonic states. (b) Non-radiative decay of incoherent states in the reservoir to coherent lower polariton states following emission of a vibrational quantum. Figure adapted from Litinskaya et al.<sup>80</sup>

## 2.6. References

1. Wenham, S. R. & Green, M. A. Silicon solar cells. *Prog. Photovoltaics* **4**, 3–33 (1996).
2. Tanenbaum, M., Valdes, L. B., Buehler, E. & Hannay, N. B. Silicon n-p-n grown junction transistors. *J. Appl. Phys.* **26**, 686–692 (1955).
3. Burroughes, J. H. *et al.* Light-emitting diodes based on conjugated polymers. *Nature* **347**, 539 (1990).
4. Dodabalapur, A. Organic Light Emitting Diodes. *Solid State Commun.* **102**, 259–267 (1997).
5. Geoghegan, M. & Hadziioannou, G. *Polymer Electronics*. (Oxford Univ. Press, 2013).
6. Fox, A. M. *Optical Properties of Solids*. (Oxford Univ. Press, 2010).
7. Kavokin, A. V., Baumberg, J. J., Malpuech, G. & Laussy, F. P. *Microcavities*. (Oxford Univ. Press, 2007).
8. Hecht, E. *Optics*. (2002).
9. Fox, A. M. *Quantum Optics: An introduction*. (Oxford Univ. Press, 2006).
10. Purcell, E. M. Spontaneous emission probabilities at radio frequencies. *Phys. Rev.* **69**, 681 (1946).
11. Weisbuch, C., Nishioka, M., Ishikawa, A. & Arakawa, Y. Observation of the coupled exciton-photon mode splitting in a semiconductor quantum microcavity. *Phys. Rev. Lett.* **69**, 3314–3317 (1992).
12. Lidzey, D. G., Bradley, D. D. C., Armitage, A., Walker, S. & Skolnick, M. S. Photon-Mediated Hybridization of Frenkel Excitons in Organic Semiconductor Microcavities. *Science* **288**, 1620–1623 (2000).
13. Kéna-cohen, S., Davanço, M. & Forrest, S. R. Strong Exciton-Photon Coupling in an Organic Single Crystal Microcavity. *Phys. Rev. Lett.* **101**, 1–4 (2008).
14. Armitage, A. *et al.* Polariton-induced optical asymmetry in semiconductor

- microcavities. *Phys. Rev. B* **58**, 15367–15370 (1998).
15. Dietrich, C. P. *et al.* An exciton-polariton laser based on biologically produced fluorescent protein. *Sci. Adv.* **2**, (2016).
  16. Deng, H., Weihs, G., Snoke, D., Bloch, J. & Yamamoto, Y. Polariton lasing vs. photon lasing in a semiconductor microcavity. *Proc. Natl. Acad. Sci. U. S. A.* **100**, 15318–15323 (2003).
  17. Wouters, M. & Carusotto, I. Excitations in a nonequilibrium bose-einstein condensate of exciton polaritons. *Phys. Rev. Lett.* **99**, 140402 (2007).
  18. Lagoudakis, K. G. *et al.* Quantized vortices in an exciton–polariton condensate. *Nat. Phys.* **4**, 706–710 (2008).
  19. Lagoudakis, K. G. *et al.* Probing the dynamics of spontaneous quantum vortices in polariton superfluids. *Phys. Rev. Lett.* **106**, 1–4 (2011).
  20. Kasprzak, J. *et al.* Bose-Einstein condensation of exciton polaritons. *Nature* **443**, 409–414 (2006).
  21. Balili, R., Hartwell, V., Snoke, D., Pfeiffer, L. & West, K. Bose-Einstein condensation of microcavity polaritons in a trap. *Science (80-. )*. **316**, 1007–10 (2007).
  22. Christmann, G., Butté, R., Feltin, E., Carlin, J.-F. & Grandjean, N. Room temperature polariton lasing in a GaN/AlGaN multiple quantum well microcavity. *Appl. Phys. Lett.* **93**, 051102 (2008).
  23. Lagoudakis, K. G. *et al.* Observation of Half-Quantum Vortices in an Exciton-Polariton Condensate. *Science (80-. )*. **326**, 974–976 (2009).
  24. Kéna-cohen, S. & Forrest, S. R. Room-temperature polariton lasing in an organic single-crystal microcavity. *Nat. Photonics* **4**, 371–375 (2010).
  25. Plumhof, J. D., Stoeflerle, T., Mai, L., Scherf, U. & Mahrt, R. F. Room-Temperature Bose-Einstein Condensation of cavity exciton-polariton in a polymer. *Nat. Mater.* **13**, 247–252 (2014).
  26. Daskalakis, K. S., Maier, S. A., Murray, R. & Kéna-cohen, S. Nonlinear

- interactions in an organic polariton condensate. *Nat. Mater.* **13**, 271–278 (2014).
27. Cookson, T. *et al.* A Yellow Polariton Condensate in a Dye Filled Microcavity. *Adv. Opt. Mater.* **5**, 1700203 (2017).
  28. Lerario, G. *et al.* Room-temperature superfluidity in a polariton condensate. *Nat. Phys.* **13**, 837–841 (2017).
  29. Hopfield, J. J. & Thomas, D. G. Polariton absorption lines. *Phys. Rev. Lett.* **15**, 22–25 (1965).
  30. Morris, G. C. & Sceats, M. G. The 4000 Å Transition of Crystal Anthracene. *Chem. Phys.* **3**, 164–179 (1974).
  31. Skolnick, M. S., Tartakovskii, A. I., Butté, R., Whittaker, D. M. & Stevenson, R. M. High-occupancy effects and stimulation phenomena in semiconductor microcavities. *IEEE J. Sel. Top. Quantum Electron.* **8**, 1060–1071 (2002).
  32. Savvidis, P. G. *et al.* Angle-Resonant Stimulated Polariton Amplifier. *Phys. Rev. Lett.* **84**, 1547–1550 (2000).
  33. Stevenson, R. M. *et al.* Continuous wave observation of massive polariton redistribution by stimulated scattering in semiconductor microcavities. *Phys. Rev. Lett.* **85**, 3680–3683 (2000).
  34. Deng, H., Weihs, G., Santori, C., Bloch, J. & Yamamoto, Y. Condensation of semiconductor microcavity exciton polaritons. *Science* **298**, 199–202 (2002).
  35. Christopoulos, S. *et al.* Room-temperature polariton lasing in semiconductor microcavities. *Phys. Rev. Lett.* **98**, 1–4 (2007).
  36. Bajoni, D. *et al.* Polariton Laser Using Single Micropillar GaAs-GaAlAs Semiconductor Cavities. *Phys. Rev. Lett.* **100**, 047401 (2008).
  37. Schneider, C. *et al.* An electrically pumped polariton laser. *Nature* **497**, 348–352 (2013).
  38. Bhattacharya, P., Xiao, B., Das, A., Bhowmick, S. & Heo, J. Solid state electrically injected exciton-polariton laser. *Phys. Rev. Lett.* **110**, 1–5 (2013).

39. Bhattacharya, P. *et al.* Room temperature electrically injected polariton laser. *Phys. Rev. Lett.* **112**, 29–31 (2014).
40. Amo, A. *et al.* Superfluidity of polaritons in semiconductor microcavities. *Nat. Phys.* **5**, 805–810 (2009).
41. Keeling, J. & Berloff, N. G. Exciton-polariton condensation. *Contemp. Phys.* **52**, 131–151 (2011).
42. Carusotto, I. & Ciuti, C. Quantum fluids of light. *Rev. Mod. Phys.* **85**, 299–366 (2013).
43. Sanvitto, D. & Kéna-Cohen, S. The road towards polaritonic devices. *Nat. Mater.* **15**, 1061–1073 (2016).
44. Berloff, N. G. *et al.* Realizing the XY Hamiltonian in polariton simulators. *Nat. Mater.* **16**, 1120–1126 (2017).
45. Wannier, G. H. The structure of electronic excitation levels in insulating crystals. *Phys. Rev.* **52**, 191–197 (1937).
46. Frenkel, J. On the transformation of light into heat in solids. i. *Phys. Rev.* **37**, 17–44 (1931).
47. Jordan, R. H., Rothberg, L. J., Dodabalapur, A. & Slusher, R. E. Efficiency enhancement of microcavity organic light emitting diodes. *Appl. Phys. Lett.* **69**, 1997–1999 (1996).
48. Takada, N., Tsutsui, T. & Saito, S. Control of emission characteristics in organic thin-film electroluminescent diodes using an optical-microcavity structure. *Appl. Phys. Lett.* **63**, 2032–2034 (1993).
49. Lidzey, D. G. *et al.* Mapping the confined optical field in a microcavity via the emission from a conjugated polymer. *Appl. Phys. Lett.* **71**, 744–746 (1997).
50. Karthaus, O., Adachi, C., Kurimura, S. & Oyamada, T. Electroluminescence from self-organized ‘microdomes’. *Appl. Phys. Lett.* **84**, 4696–4698 (2004).
51. Fisher, T. A. *et al.* Electroluminescence from a conjugated polymer microcavity structure. *Appl. Phys. Lett.* **67**, 1355 (1995).

52. Wittmann, H. F. *et al.* Microcavity effect in a single-layer polymer light-emitting diode. *Adv. Mater.* **7**, 541–544 (1995).
53. Dodabalapur, A. *et al.* Physics and applications of organic microcavity light emitting diodes. *J. Appl. Phys.* **80**, 6954–6964 (1996).
54. D. G. Lidzey *et al.* Strong exciton-photon coupling in an organic semiconductor microcavity. *Lett. to Nat.* **395**, 53–55 (1998).
55. Kelkar, P. *et al.* Excitons in a II-VI Semiconductor Microcavity in the Strong Coupling Regime. *Phys. Rev. B* **52**, 5491–5494 (1995).
56. Houdré, R., Stanley, R. P., Oesterle, U., Ilegems, M. & Weisbuch, C. Room-temperature cavity polaritons in a semiconductor microcavity. *Phys. Rev. B* **49**, 16761–16764 (1994).
57. Skolnick, M. S., Fisher, T. A. & Whittaker, D. M. Strong coupling phenomena in quantum microcavity structures. *Semicond. Sci. Technol.* **13**, 645–669 (1998).
58. Kéna-Cohen, S., Maier, S. A., C Bradley S Kéna-Cohen, D. D., Maier, S. A. & C Bradley, D. D. Ultrastrongly Coupled Exciton–Polaritons in Metal-Clad Organic Semiconductor Microcavities. *Adv. Opt. Mater.* **1**, 827–833 (2013).
59. Gambino, S. *et al.* Exploring Light-Matter Interaction Phenomena under Ultrastrong Coupling Regime. *ACS Photonics* **1**, 1042–1048 (2014).
60. Wei, H.-S. *et al.* Adjustable exciton-photon coupling with giant Rabi-splitting using layer-by-layer J-aggregate thin films in all-metal mirror microcavities. *Opt. Express* **21**, 21365 (2013).
61. Ciuti, C., Bastard, G. & Carusotto, I. Quantum vacuum properties of the intersubband cavity polariton field. *Phys. Rev. B - Condens. Matter Mater. Phys.* **72**, 1–9 (2005).
62. Lidzey, D. G. *et al.* Room Temperature Polariton Emission from Strongly Coupled Organic Semiconductor Microcavities. *Phys. Rev. Lett.* **82**, 3316–3319 (1999).

63. Scafirimuto, F., Urbonas, D., Scherf, U., Mahrt, R. F. & Stöferle, T. Room-Temperature Exciton-Polariton Condensation in a Tunable Zero-Dimensional Microcavity. *ACS Photonics* **5**, 85–89 (2018).
64. Tischler, J. R., Bradley, M. S., Bulović, V., Song, J. H. & Nurmikko, A. Strong coupling in a microcavity LED. *Phys. Rev. Lett.* **95**, 036401 (2005).
65. Christogiannis, N. *et al.* Characterizing the Electroluminescence Emission from a Strongly Coupled Organic Semiconductor Microcavity LED. *Adv. Opt. Mater.* **1**, 503–509 (2013).
66. Gubbin, C. R., Maier, S. A. & Kéna-Cohen, S. Low-voltage polariton electroluminescence from an ultrastrongly coupled organic light-emitting diode. *Appl. Phys. Lett.* **104**, (2014).
67. Graf, A. *et al.* Electrical pumping and tuning of exciton-polaritons in carbon nanotube microcavities. *Nat. Mater.* **16**, 911–917 (2017).
68. Coles, D. *et al.* Polariton-mediated energy transfer between organic dyes in a strongly coupled optical microcavity. *Nat. Mater.* **13**, 712–9 (2014).
69. Zhong, X. *et al.* Non-Radiative Energy Transfer Mediated by Hybrid Light-Matter States. *Angew. Chemie - Int. Ed.* **55**, 6202–6206 (2016).
70. Zhong, X. *et al.* Energy Transfer between Spatially Separated Entangled Molecules. *Angew. Chemie Int. Ed.* **56**, 9034–9038 (2017).
71. Georgiou, K. *et al.* Control over energy transfer between fluorescent BODIPY dyes in a strongly-coupled microcavity. *ACS Photonics* **5**, 258–266 (2018).
72. Shalabney, A. *et al.* Coherent coupling of molecular resonators with a microcavity mode. *Nat. Commun.* **6**, 5981 (2015).
73. George, J., Shalabney, A., Hutchison, J. A., Genet, C. & Ebbesen, T. W. Liquid-phase vibrational strong coupling. *J. Phys. Chem. Lett.* **6**, 1027–1031 (2015).
74. Long, J. P. & Simpkins, B. S. Coherent coupling between a molecular vibration and fabry-perot optical cavity to give hybridized states in the strong coupling limit. *ACS Photonics* **2**, 130–136 (2015).

75. del Pino, J., Feist, J. & Garcia-Vidal, F. J. Quantum theory of collective strong coupling of molecular vibrations with a microcavity mode. *New J. Phys.* **17**, 053040 (2015).
76. Michetti, P. & La Rocca, G. C. Polariton states in disordered organic microcavities. *Phys. Rev. B - Condens. Matter Mater. Phys.* **71**, 115320 (2005).
77. Grant, R. T. *et al.* Efficient Radiative Pumping of Polaritons in a Strongly Coupled Microcavity by a Fluorescent Molecular Dye. *Adv. Opt. Mater.* **4**, 1615–1623 (2016).
78. Michetti, P. & La Rocca, G. C. Simulation of J-aggregate microcavity photoluminescence. *Phys. Rev. B - Condens. Matter Mater. Phys.* **77**, 195301 (2008).
79. Michetti, P. & La Rocca, G. C. Exciton-phonon scattering and photoexcitation dynamics in J-aggregate microcavities. *Phys. Rev. B - Condens. Matter Mater. Phys.* **79**, 035325 (2009).
80. Litinskaya, M., Reineker, P. & Agranovich, V. M. Fast polariton relaxation in strongly coupled organic microcavities. *J. Lumin.* **110**, 364–372 (2004).
81. Virgili, T. *et al.* Ultra-fast polariton dynamics in an organic microcavity. *EPJ Web Conf.* **41**, 04015 (2013).
82. Coles, D. *et al.* Vibrationally assisted polariton-relaxation processes in strongly coupled organic-semiconductor microcavities. *Adv. Funct. Mater.* **21**, 3691–3696 (2011).
83. Mazza, L., Fontanesi, L. & La Rocca, G. C. Organic-based microcavities with vibronic progressions: Photoluminescence. *Phys. Rev. B* **80**, 235314 (2009).
84. Mazza, L., Kéna-Cohen, S., Michetti, P. & La Rocca, G. C. Microscopic theory of polariton lasing via vibronically assisted scattering. *Phys. Rev. B* **88**, 075321 (2013).
85. Tartakovskii, A. I. *et al.* Relaxation bottleneck and its suppression in semiconductor microcavities. *Phys. Rev. B* **62**, R2283 (2000).

86. Lidzey, D. G. *et al.* Experimental study of light emission from strongly coupled organic semiconductor microcavities following nonresonant laser excitation. *Phys. Rev. B* **65**, 195312 (2002).
87. Virgili, T. *et al.* Ultrafast polariton relaxation dynamics in an organic semiconductor microcavity. *Phys. Rev. B* **83**, 245309 (2011).
88. Agranovich, V. M., Litinskaya, M. & Lidzey, D. G. Cavity polaritons in microcavities containing disordered organic semiconductors. *Phys. Rev. B* **67**, 085311 (2003).
89. Lodden, G. H. & Holmes, R. J. Electrical excitation of microcavity polaritons by radiative pumping from a weakly coupled organic semiconductor. *Phys. Rev. B - Condens. Matter Mater. Phys.* **82**, 125317 (2010).

## Chapter 3. Exploring the photophysics of BODIPY-core materials as microcavity active layers

### 3.1. Introduction

As discussed in Chapter 2, the condition  $g_o \gg (k, \gamma)$  must be met in a microcavity in order to enter the strong coupling regime. Apart from the quality of the cavity (which determines the photon decay rate), the properties of the semiconducting material placed in the active region play an important role and can define whether the microcavity will enter the strong coupling regime. Materials having a transition with a relatively narrow linewidth and high oscillator strength are more suitable for microcavity active layers as narrow transitions minimise the emission into modes not resonant with the cavity. It has been shown that materials with broad electronic transitions can enter the strong coupling regime, however, to do this, it is necessary that such materials possess very high oscillator strength.<sup>1,2</sup>

In all the experiments described in this thesis, boron-dipyrromethene (BODIPY) core materials were used as the active semiconducting materials. The different BODIPY derivatives were synthesized by Marco Cavazzini and Francesco Galeotti at ISMAC and ISTM – CNR, Milan Italy and Lizhi Gai and Zhen Shen at Nanjing University, Nanjing China. BODIPY-core materials are fluorescent dyes that have a relatively narrow electronic transition and possess high oscillator strength. They are very good candidates for sensing and labelling applications<sup>3,4</sup> due to their stability and high quantum efficiency.<sup>5,6</sup> This class of material is very soluble in toluene and makes smooth films of low roughness when dispersed in a polystyrene (PS) matrix at high concentration (up to 20% by mass). Figure 3.1 shows an atomic force microscopy (AFM) image of a film of a BODIPY dye dispersed in a PS/toluene matrix at 10% concentration by mass. The RMS roughness of the film shown in Figure 3.1 was measured to be less than 1 nm. It is important to emphasize that the quality of the film is crucial for the fabrication of high quality microcavities. A rough surface layer would compromise the quality of the top mirror, and consequently reduce the Q factor of the cavity. Large fluctuations of the active region thickness over small length scales would affect the cavity length and induce broadening of the cavity mode.

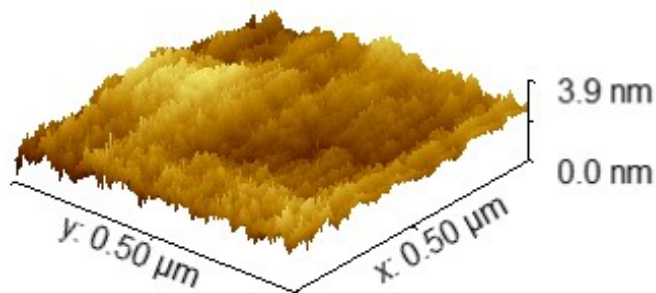


**Figure 3.1.** AFM measurement of a film of a BODIPY dye dispersed in polystyrene at a concentration of 10% by mass with measured roughness RMS < 1 nm.

The photophysics of a series of BODIPY-core dyes were explored before any of these materials were incorporated into a microcavity structure. This allowed a better understanding of the optical properties of the materials to be gained before moving onto the more complex cavity experiments.

The optical properties of the different BODIPY-core materials were adjusted by chemical modifications during synthesis.<sup>7-14</sup> Figure 3.2 shows the absorption and photoluminescence (PL) of a number of BODIPY-core materials doped in PS matrix at different concentrations, along with their chemical structures. Here, all films were 300 nm thick and deposited on quartz-coated glass substrates. To measure UV-Vis absorption, a Horiba Fluoromax 4 fluorometer was used equipped with a Xenon lamp. For the PL measurements a 473 nm laser diode was used to excite the films with the PL detected using a Newton CCD coupled to an Andor Shamrock spectrometer. The change of the PL spectrum with concentration is attributed to the formation of excimers and aggregates.<sup>15</sup> We categorise the different materials into two classes as shown in Figure 3.2 E1, 2 and 3 and A1, 2 and 3, where E and A stand for excimers and aggregates respectively. In the E class, increasing the concentration yields a broadening at long wavelengths, consistent with the formation of excimers. In the A class, an increase in the concentration results in the formation of ground-state aggregates which manifest themselves as strongly red-shifted, highly structured spectral features.<sup>15</sup>

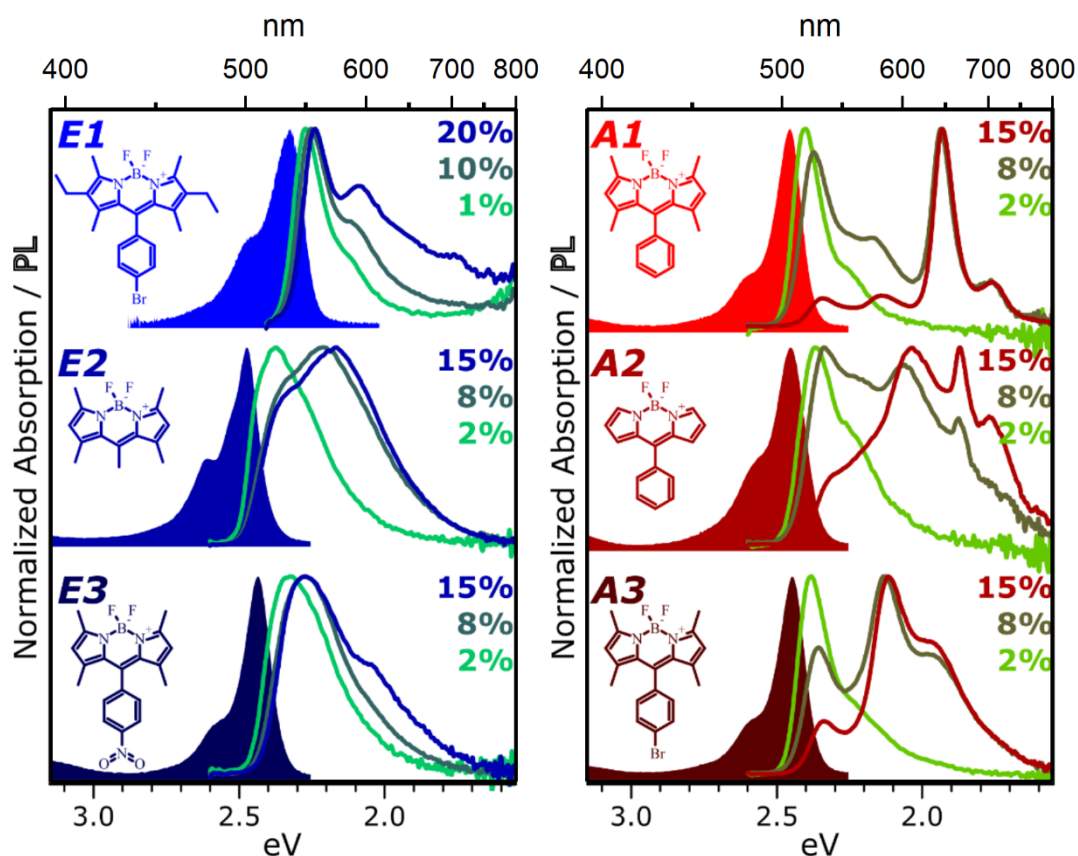


**Figure 3.2.** Chemical structures and normalised UV-Vis absorption (filled) and PL spectra (lines) of the BODIPY derivatives. Molecules were dispersed in polystyrene matrix, at three different loading ratios (1%, 10% and 20% by mass for E1 and 2%, 8% and 15% by mass for E2, E3, A1, A2 and A3).

### 3.2. Photoluminescence quantum yield

The photoluminescence quantum yield (PLQY) of BODIPY E2 and 3 and A1 to 3 was measured using an integrating sphere configuration as plotted in Figure 3.3. The films were mounted inside the sphere and excited using a frequency-doubled mode-locked Coherent Mira 900 Ti:Sapphire crystal pumped by a 532 nm Verdi V10. The PL was fibre-coupled from the sphere into an Oriel MS-125 1/8<sup>th</sup> m spectrometer. As it can be seen, the PLQY drops with increasing concentration, a result largely attributed to excimer-related non-radiative decay pathways.<sup>16</sup> The PLQY of BODIPY E1 has been previously reported<sup>17</sup> and exhibits a concentration-dependent PLQY drop similar to the materials shown in Figure 3.3.

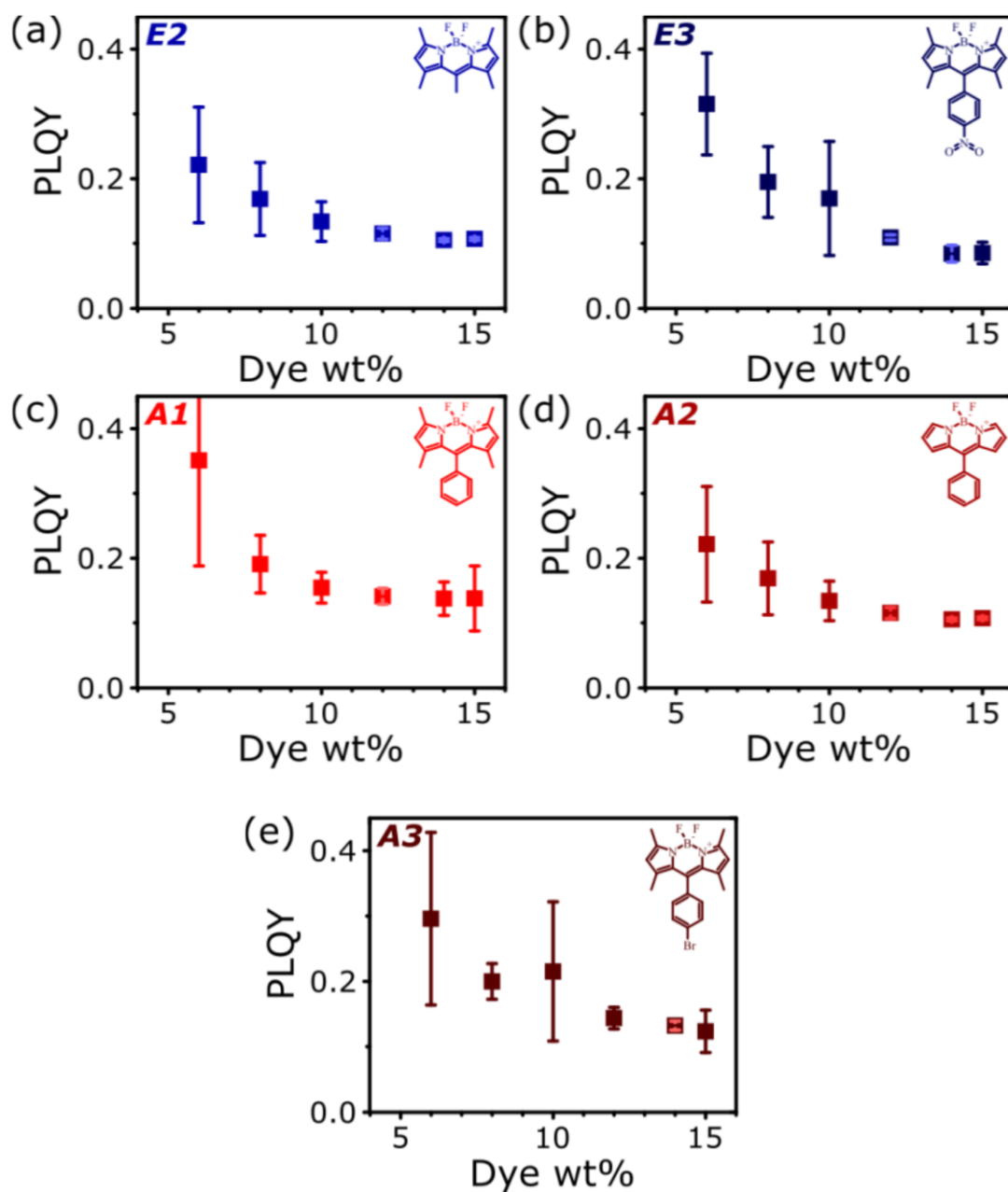


**Figure 3.3.** Photoluminescence quantum yield (PLQY) of (a) E2, (b) E3, (c) A1, (d) A2 and (e) A3 BODIPY derivatives with increasing concentration (6-15% by mass)

### 3.3. Photo-oxidation

We have explored photo-oxidation during laser excitation. This is an important property that determines which materials are most suitable for condensation applications in a microcavity. The relative PL efficiency as a function of illumination time of BODIPY dyes was measured following ~10 minutes of continuous

illumination, with PL recorded every 1 to 2 minutes. The laser used in these experiments was a Coherent Libra-HE<sup>+</sup> frequency-doubled Ti:Sapphire pulsed laser (400 nm) with 1 kHz repetition rate and 100 fs pulse length. The measurements were taken at the femtosecond laboratory at the Dipartimento di Fisica, Politecnico di Milano in Milan, Italy with help and guidance provided by Sai Kiran Rajendran and Tersilla Virgili. The selection of the laser wavelength at 400 nm was intended to coincide with the excitation wavelength that would be later used for polariton condensation experiments (see Chapter 4). As it will be discussed later, in condensation experiments the DBRs were designed to have minimum reflectivity at 400 nm, and thus this laser wavelength would be effectively coupled into the cavity.

Dyes were spin-cast on quartz-coated glass substrates at a concentration of 12% by mass for E2-3 & A1-3 and 15% for E1. The value of the peak PL intensity was normalised to the initial peak PL intensity for each material at  $t=0$  sec (Figure 3.4). For comparison, the perylene-based materials Perylene-Red (9.4% by mass in PS/toluene) and Lumogen-F Orange (LFO) (6% by mass in PS/toluene), were also tested under the same conditions. Perylene-Red and LFO both absorb light at a spectral region similar to that of BODIPY derivatives. As it can be seen, the perylene-based materials are more stable over time, while the different BODIPY dyes all undergo a similar PL efficiency reduction over time, with E1 being the mostly affected by laser excitation. Considering that E1 was dispersed at 15% by mass in PS compared to 12% used for the other BODIPYs, it is possible that this behaviour might be related to the higher concentration of the material. This concentration dependence of the relative PL stability over time is also shown in Figure 3.5 where the degradation of the different BODIPY dyes at two concentrations (4% and 12% by mass in PS/toluene) is plotted. It appears that the higher the concentration of the dye in the matrix, the quicker the PL efficiency reduces following laser excitation.

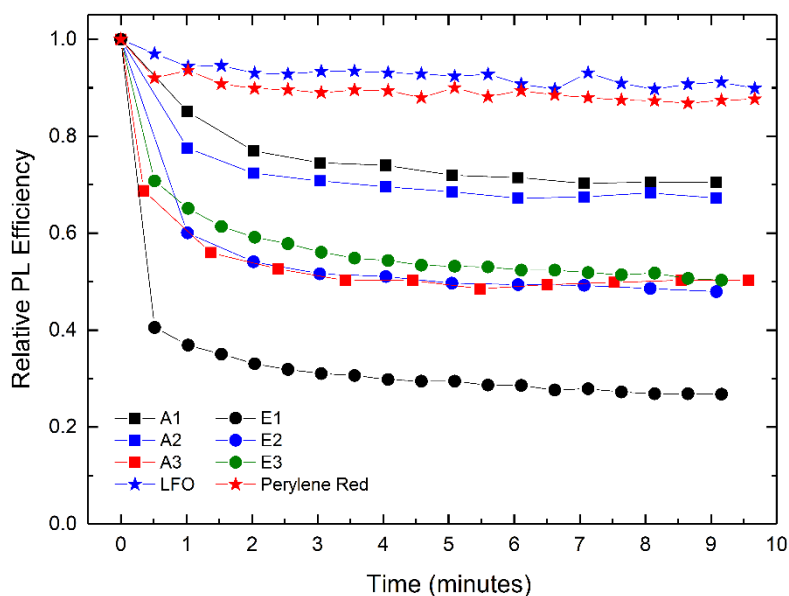


**Figure 3.4.** Relative PL efficiency as a function of time following 10 minutes of continuous laser excitation. Data plotted for thin films of BODIPY derivatives E1-3 and A1-3 as well as two perylene-based materials, Perylene-Red and LFO.

### 3.4. Amplified spontaneous emission

Optical gain is an important requirement for materials that are used as laser media, as this it quantifies the efficiency of optical amplification within the material. Following optical excitation, spontaneous emission causes stimulated emission of identical photons, resulting in amplified spontaneous emission (ASE). This emission has a characteristic nonlinear behaviour with excitation density and is manifested by a laser-like narrowing of the PL spectra, which indicates the gain spectral region of the material. An easy experimental approach to investigate whether a material undergoes optical gain is the stripe-length method.<sup>18</sup>

Although it is not yet very clear which material properties are important in order to achieve polariton lasing and condensation in organic systems, efficient population of the bottom of the lower polariton branch appears to be a key ingredient in this process. Low optical loss within a material, which is directly related to whether or not the material can support optical amplification, is likely a desirable property for materials undergoing polariton condensation and lasing.<sup>19-21</sup> We have therefore explored ASE measurements on the BODIPY-core materials in order to identify whether they undergo optical gain.

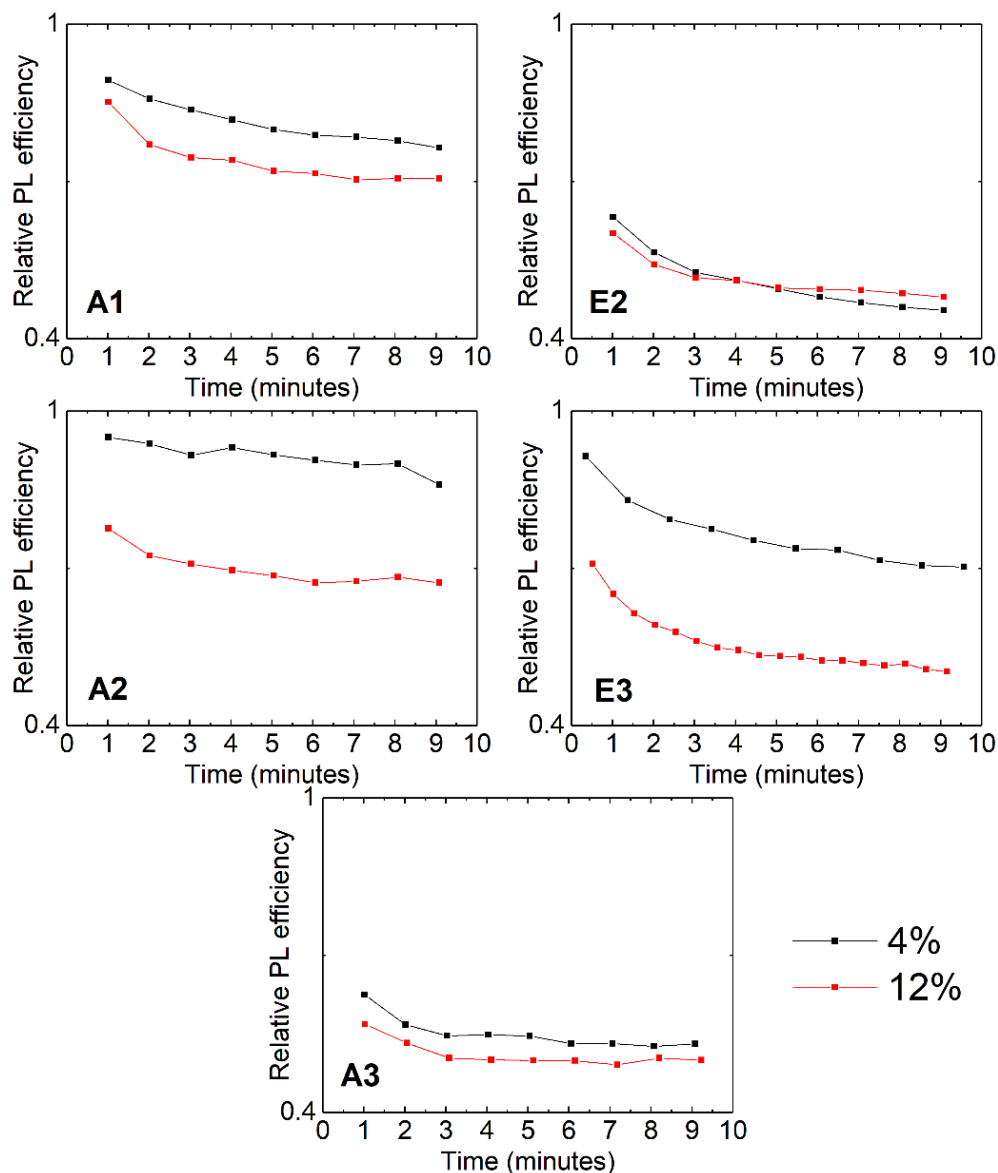


**Figure 3.5.** Relative PL efficiency over time following 10 minutes of continuous excitation for thin films of BODIPY derivatives A1, 2 and 3 and E2 and 3 at a concentration of 4% (black) and 12% (red) by mass.

BODIPY E1 has been extensively studied in this thesis and it is also known as BODIPY-Br as it is a bromine-substituted variant upon boron-dipyrromethene. For this reason, BODIPY-Br (E1) has been studied in more detail compared to the other BODIPY derivatives in this chapter. For simplicity, from now on we will refer to BODIPY E1 as BODIPY-Br.

Experiments were performed at Politecnico di Milano using the laser described in Section 3.3. Experiments were performed at two different excitation wavelengths. Here, an optical parametric amplifier (OPA) was used to generate light at 500 nm. Laser light was focused onto the sample at normal incidence after having passed through a cylindrical lens in order to create a stripe excitation. The profile of the stripe beam is shown in Figure 3.6 (a), where its area is calculated to be  $A = 0.0209 \text{ mm}^2$ . Following excitation of the film using the stripe configuration, PL was detected through the side of the sample, in a direction perpendicular to the excitation beam (see Figure 3.6 (b)). Unlike PL emission from a thin film (which is emitted in all directions), ASE is strongly directional. The stripe excitation method is based on a waveguide effect<sup>18,22</sup> where spontaneous emission causes waveguided photons to propagate along the stripe, resulting in stimulated emission of identical photons and therefore optical amplification.

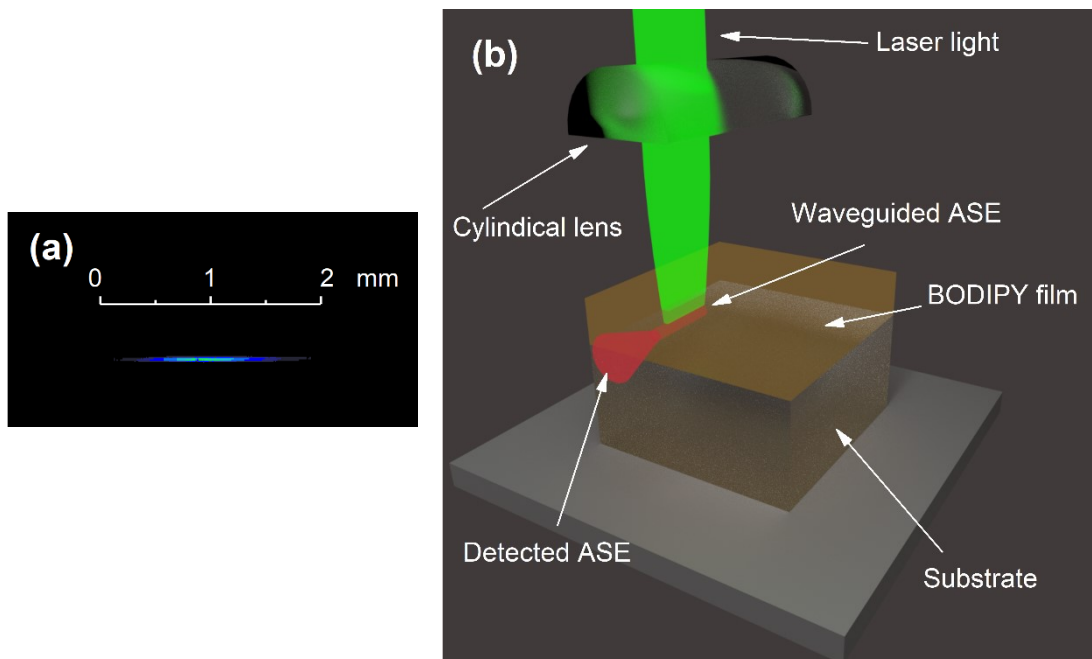


**Figure 3.6.** (a) Stripe beam profile having an area of  $A = 0.0209 \text{ mm}^2$ . (b) Schematic of the waveguided ASE process showing the collimated laser beam passing through a cylindrical lens creating a stripe laser excitation. The ASE PL is waveguided along the laser stripe and exits from the side of the film.

The different BODIPY derivatives were spin-cast on quartz-coated glass, creating thin films having thicknesses of 200 nm and 300 nm. The concentration of the dyes in the polymer matrix (polystyrene) was also tuned between 2-15% by mass. The emission spectra of the dyes were recorded at low, medium and high excitation densities. Figure 3.7 shows the normalised waveguided PL emission collected from the edge of a 300 nm film of the dye BODIPY-Br at a concentration of 14% by mass, when excited at 400 nm with a stripe configuration at three excitation densities ( $40 \mu\text{J cm}^{-2}$ ,  $200 \mu\text{J cm}^{-2}$  and  $240 \mu\text{J cm}^{-2}$ ). It can be seen that the excitation density of  $40 \mu\text{J cm}^{-2}$  is well below ASE threshold (black), the  $200 \mu\text{J cm}^{-2}$  corresponds to the ASE threshold (red) and excitation at  $240 \mu\text{J cm}^{-2}$  is above threshold (blue).

A series of BODIPY-Br films of concentrations 2-15% by mass and film thicknesses of 200 nm and 300 nm were excited using the stripe configuration in order to identify if they possess optical gain. The cut-off thickness ( $h_c$ ) at which no waveguided emission is expected to be supported by the films, was calculated using waveguide modelling. This is given by Equation 3.1 which defines the cut-off condition of the zeroth order mode.<sup>23</sup>

$$\frac{h_c}{\lambda} = \frac{\tan^{-1} \sqrt{(n_s^2 - n_a^2)/(n_f^2 - n_s^2)}}{2\pi \sqrt{(n_f^2 - n_s^2)}} \quad (3.1)$$

Here  $\lambda$  is the emission wavelength, while  $n_f$ ,  $n_s$  and  $n_a$  are the refractive indices of the organic film, substrate and air, respectively. We find that for a wavelength range corresponding to emission from BODIPY dyes, the cut-off thickness is well below the thickness of the films under investigation.

Figure 3.8 shows the ASE threshold of 200 nm (black) and 300 nm (red) films when excited using laser light at 400 nm (solid squares) and 500 nm (solid circles). As it can be seen, the threshold excitation density,  $P_{th}$ , has a strong concentration dependence which we attribute to the following two reasons: (i) With increasing concentration the threshold is significantly reduced, indicating that at higher dye concentration in PS, intermolecular distances are reduced as there are a larger number of molecules per unit

volume leading to higher optical gain.<sup>23,24</sup> (ii) Using waveguide modelling, it has been shown that the so-called ‘confinement factor’ (which is directly related to the ASE threshold)<sup>22</sup> is strongly dependent on the effective refractive index of the waveguide.<sup>22,23</sup> A higher concentration of a dye in the matrix, will increase the effective refractive index of the film, leading to a higher confinement factor and reduced ASE threshold.

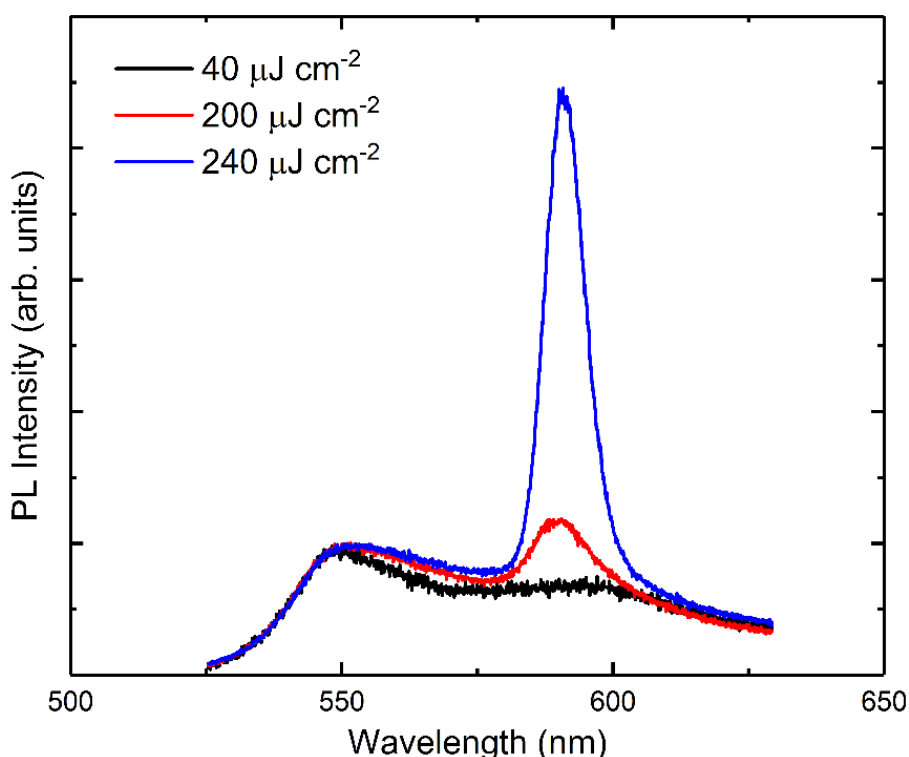


**Figure 3.7.** ASE measurement of a 300 nm film of BODIPY-Br at 14% concentration by mass in polystyrene when excited at 400 nm. Spectra recorded for 40  $\mu\text{J cm}^{-2}$  (black line), 200  $\mu\text{J cm}^{-2}$  (red line) and 240  $\mu\text{J cm}^{-2}$  (blue line) excitation densities.

Note that the confinement factor is also related to the thickness of the film ( $h$ ) through the effective thickness ( $h_{eff}$ ) of the waveguide. As shown in Equation 3.2 the effective thickness is the sum of the thickness of the film and the penetration depth of the optical mode into the media that surround the waveguide (the substrate,  $x_s$  and air,  $x_a$ ).<sup>22,23</sup> Here, the confinement factor is maximized when the effective thickness corresponds to the thickness of the film. Increasing the thickness of the film will result in a higher

confinement factor, which in turn reduces the ASE threshold as can be seen in Figure 3.8.<sup>22</sup>

$$h_{eff} = h + x_s + x_a \quad (3.2)$$

The excitation wavelength dependence of the ASE threshold is attributed to the fact that the dye absorption is higher at 500 nm compared to 400 nm where the absorption is minimum (see Figure 3.2). Therefore, exciting with 400 nm laser pulse leads to higher ASE thresholds compared to 500 nm pulse as shown in Figure 3.8.

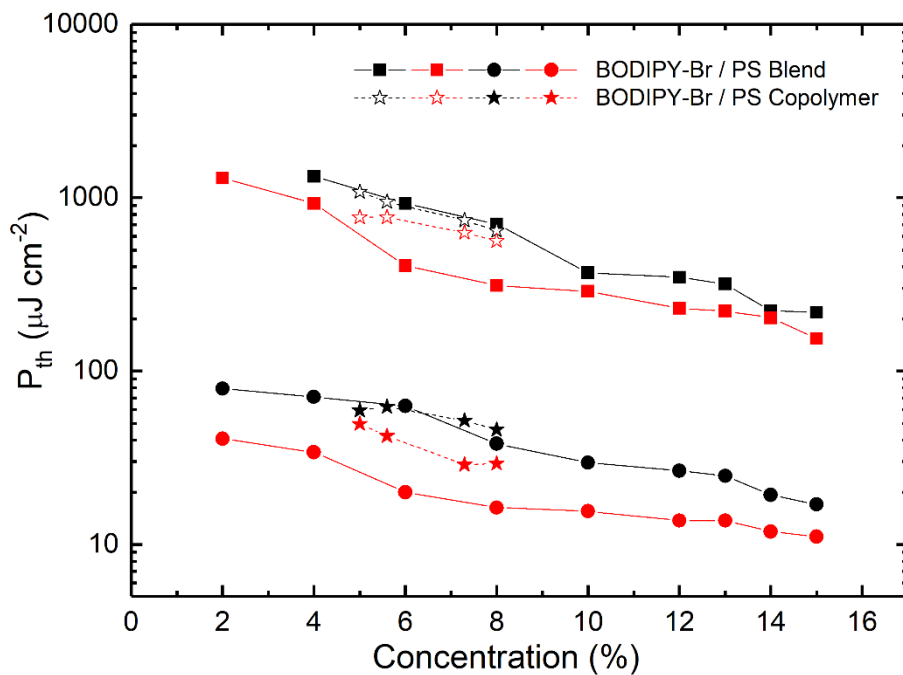


**Figure 3.8.** ASE thresholds for 200 nm (black) and 300 nm (red) films of BODIPY-Br doped in polystyrene at different concentrations when excited at 400 nm (solid squares) and 500 nm (solid circles). ASE thresholds for 200 nm (black) and 300 nm (red) films of BODIPY-Br/PS copolymers when excited at 400 nm (open stars) and 500 nm (solid stars). The ASE threshold is defined as the excitation density at which the FWHM is reduced to half of that of low excitation density.<sup>22,23</sup>

We have also studied a polystyrene copolymer onto which BODIPY-Br was attached to the polymer chain during synthesis. Four different copolymers were studied that contained BODIPY-Br at a concentration by mass of 5%, 5.6%, 7.3% and 8%. As can be seen in Figure 3.8 (star symbols), the ASE thresholds are similar to those of films of BODIPY-Br that are dispersed into PS. It is worth noting that in these copolymers, the concentration of BODIPY-Br is relatively low and cannot be adjusted (unless it is tuned during synthesis). For this reason these materials are not suitable for strong coupling in a microcavity due to their relatively low oscillator strength. Here, it was calculated that a BODIPY-Br / PS copolymer film of 5.6% by mass has 4 times smaller effective oscillator strength compared to a 10% by mass BODIPY / PS blend film.

We find that the other BODIPY derivatives (E2-3 and A1-3) undergo optical gain with similar threshold concentration dependence to that of BODIPY-Br. This is summarised in Figure 3.9. Here 200 nm BODIPY-Br, E2, E3 and A1, A2, A3 films were excited using light at 500 nm in a stripe geometry.

We find that the peak wavelength of the ASE is dependent on dye concentration and thickness of the films. With increasing concentration, the peak ASE wavelength of BODIPY derivatives undergoes a continuous redshift. Figure 3.10 shows this behaviour for BODIPY-Br films of 300 nm (black) and 200 nm (red) thickness when excited with 400 nm laser pulses. This effect has been previously observed and attributed to increased self-absorption at shorter wavelength and at higher concentrations. This reduces the optical gain in the high-energy spectral region, pushing the ASE to longer wavelengths.<sup>23</sup> It has also been suggested that at higher concentrations the polarity of the film increases due to the polarity of the fluorophore.<sup>23</sup> Interestingly, Calzado et al.<sup>23</sup> observed that the 0-0 PL emission wavelength at low excitation density also undergoes a spectral red-shift with increasing concentration. We have shown previously that BODIPY derivatives, exhibit a red shift in their emission spectra at higher concentration (similar to Calzado et al.<sup>23</sup>), which has been attributed to the formation of excimers and aggregates.<sup>15</sup> It is likely therefore that these two effects (self-absorption and excimer formation) explain the red-shift of the peak ASE wavelength with concentration in BODIPY / PS films.

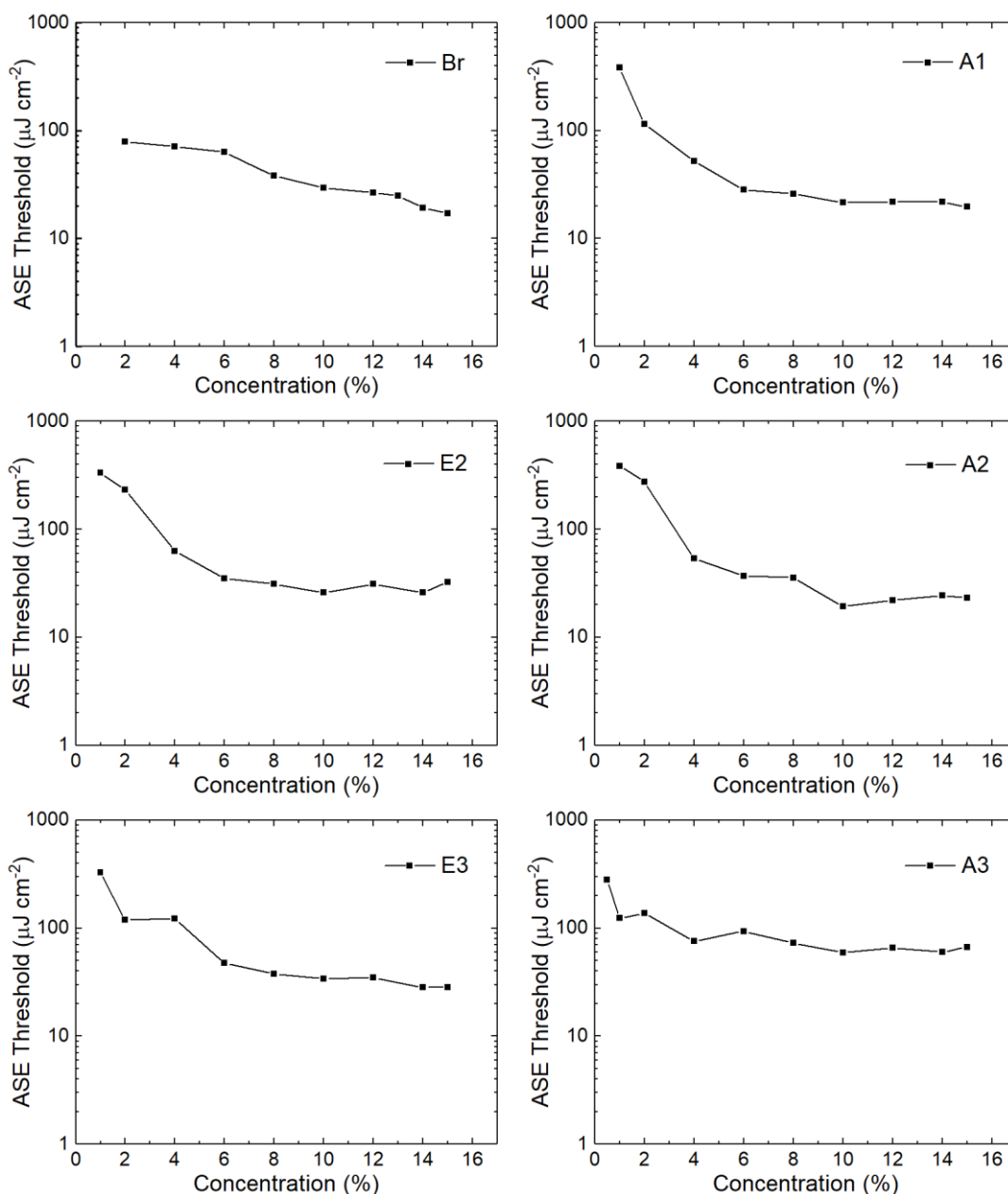


**Figure 3.9.** ASE thresholds for 200 nm films of BODIPY derivatives doped in polystyrene at different concentrations when excited at 500 nm. The ASE threshold is defined as the excitation density when the FWHM is reduced to half of that of low excitation density.

In summary therefore, to find a material suitable for strong coupling and condensation we should consider the findings above. A material should have a high oscillator strength at moderate concentration to allow it enter the strong coupling regime without (i) compromising its ability to emit light efficiently (high PLQY) and (ii) being susceptible to significant photo-oxidation. In addition, it must support optical amplification. This will ensure that there are not significant optical losses following

high-density excitation, which is a desirable property of materials for polariton condensation.<sup>19</sup> BODIPY-Br possesses all these properties, with its ability to emit light and support optical gain in the yellow-orange spectral region (a wavelength difficult to engineer using traditional inorganic semiconductors), making it a promising material system for room-temperature polariton lasing applications. For this reason, BODIPY-Br has selected as the active-material in the polariton condensate described in Chapter 4.

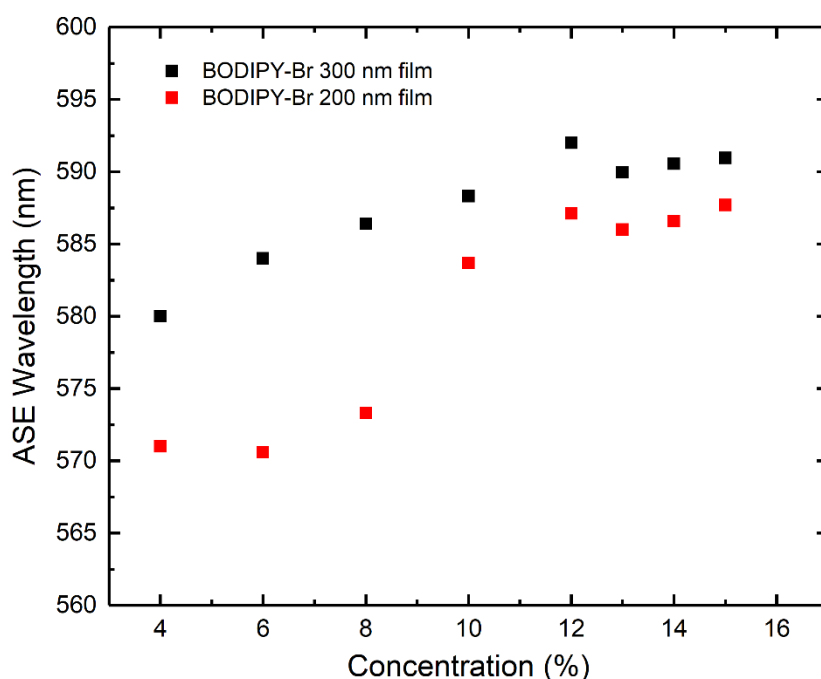


**Figure 3.10.** Peak ASE wavelength of 300 nm (black) and 200 nm (red) thin films of BODIPY-Br when excited with 400 nm laser pulses at different concentrations in PS.

### 3.5. Strong coupling in BODIPY-filled microcavities

Before progressing to lasing experiments, this section describes the linear optical properties of a series of microcavities containing the different BODIPY-derivatives. Here, the cavities were based on two DBR mirrors. The bottom mirror was made out of 10 pairs of alternating SiO<sub>2</sub> / Nb<sub>2</sub>O<sub>5</sub> layers. These layers were deposited onto quartz-coated glass substrates using ion assisted electron beam evaporation (Nb<sub>2</sub>O<sub>5</sub>) and reactive sublimation (SiO<sub>2</sub>). After the deposition of the bottom mirror, the active

layer was spin-cast having an appropriate thickness to create a  $\lambda/2$  cavity. The top mirror was then deposited on top of the organic material consisting of 8 pairs of alternating  $\text{SiO}_2$  /  $\text{Nb}_2\text{O}_5$  layers. The ion gun was turned off during the deposition of the first few layers of the top mirror to avoid any damage to the organic film.

All the BODIPY derivatives were dispersed in PS at a concentration of 10% by mass. The thickness of the active layer was tuned in order to fabricate a series of cavities with small ( $\delta=-40$  meV), intermediate ( $\delta=-160$  meV) and large ( $\delta=-280$  meV) negative photon-exciton detunings.

Angular white-light reflectivity measurements indicate that all cavities appear to enter the strong coupling regime. Figures 3.11 and 3.12 show data from angle-dependent white-light reflectivity (left) and angle-dependent PL (right) measurements made on cavities filled with thin films of BODIPY E2-E3 and A1-A3. All cavities were designed to have the bottom of the LPB around 570-575 nm; a wavelength region close to the maximum reflectivity of the DBRs. Data recorded on microcavities filled with the fluorescent dye BODIPY-Br is not presented here, as Chapter 4 is dedicated to the demonstration of strong coupling and realisation of polariton condensation in the BODIPY-Br system.

White-light reflectivity measurements were performed using a goniometer configuration (see Figure 3.13). Two arms mounted on two concentric motorised wheels were used to change the angle of the incident light onto the microcavity as well as the collection path of the reflected light from the microcavity. A fibre-coupled Ocean Optics DH-2000 Halogen-Deuterium lamp was focused onto the surface of the microcavity using a collimating ( $l_1$ ) and a focussing ( $l_2$ ) lens both attached on the first arm.

The reflected light was collected using two lenses ( $l_3$  and  $l_4$ ) that were attached to a second arm, with light focused into a fibre-coupled Andor Shamrock CCD spectrometer. For PL measurements, the microcavities were excited using a laser diode focused onto the cavity close to normal incidence with the laser beam having a slight downwards tilt to avoid direct reflection into the CCD camera.

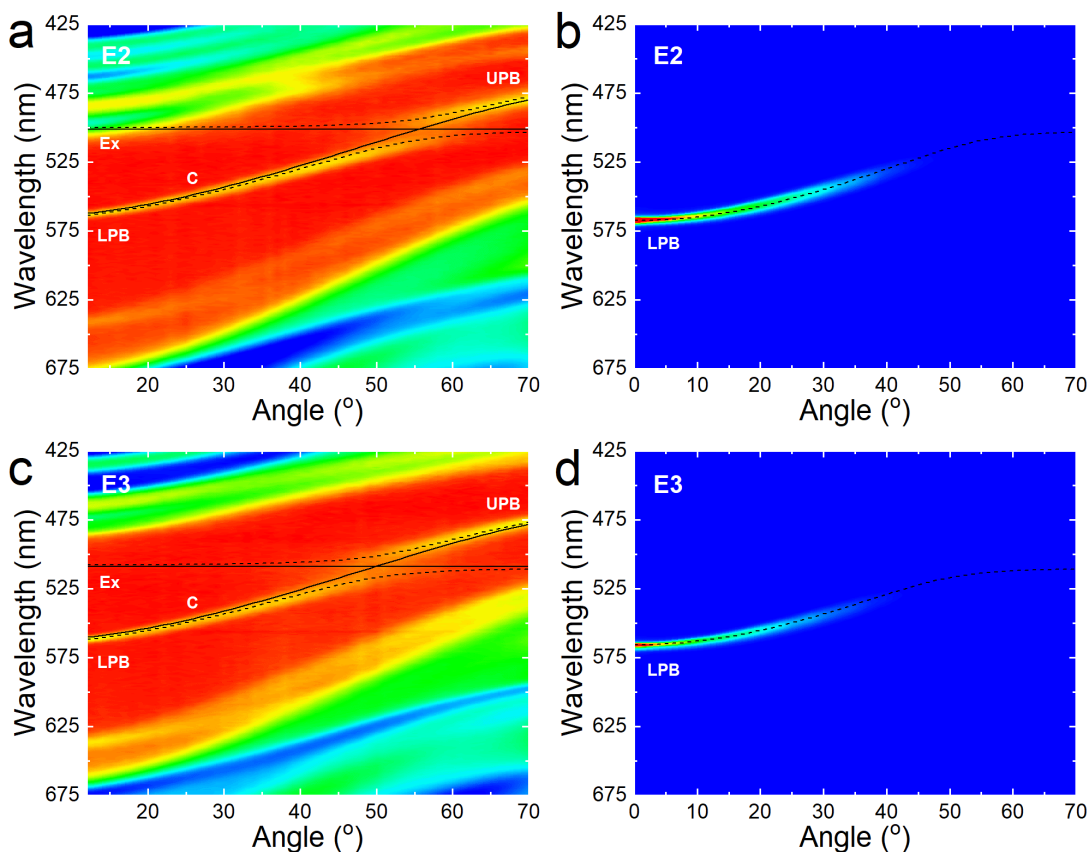


**Figure 3.11.** Unpolarized angular white-light reflectivity data and PL emission from a DBR-DBR microcavity containing the dye BODIPY-E2 parts (a) & (b) and BODIPY-E3 parts (c) & (d), along with the LPB and UPB (dashed lines) and photon (C) and exciton (Ex) energies (solid lines) extracted from a standard two-level coupled oscillator model.

Photoluminescence emission measurements were made following non-resonant excitation at 405 nm, with all measurements made at room temperature. Collection of the angular polariton emission was achieved through the collection arm used in reflectivity measurements (second motorised arm). As it can be seen in Figures 3.11 and 3.12, the angle was tuned from 12° to 70° for the white-light reflectivity measurements and 0° to 70° for the PL measurements with an angle resolution of 1°.

A standard two-level coupled oscillator model, which is explained in detail in Chapter 2, has been used to describe the two polariton modes, LPB and UPB, along with the cavity mode (C) and exciton energy (Ex). This can be seen in Figures 3.11 and 3.12

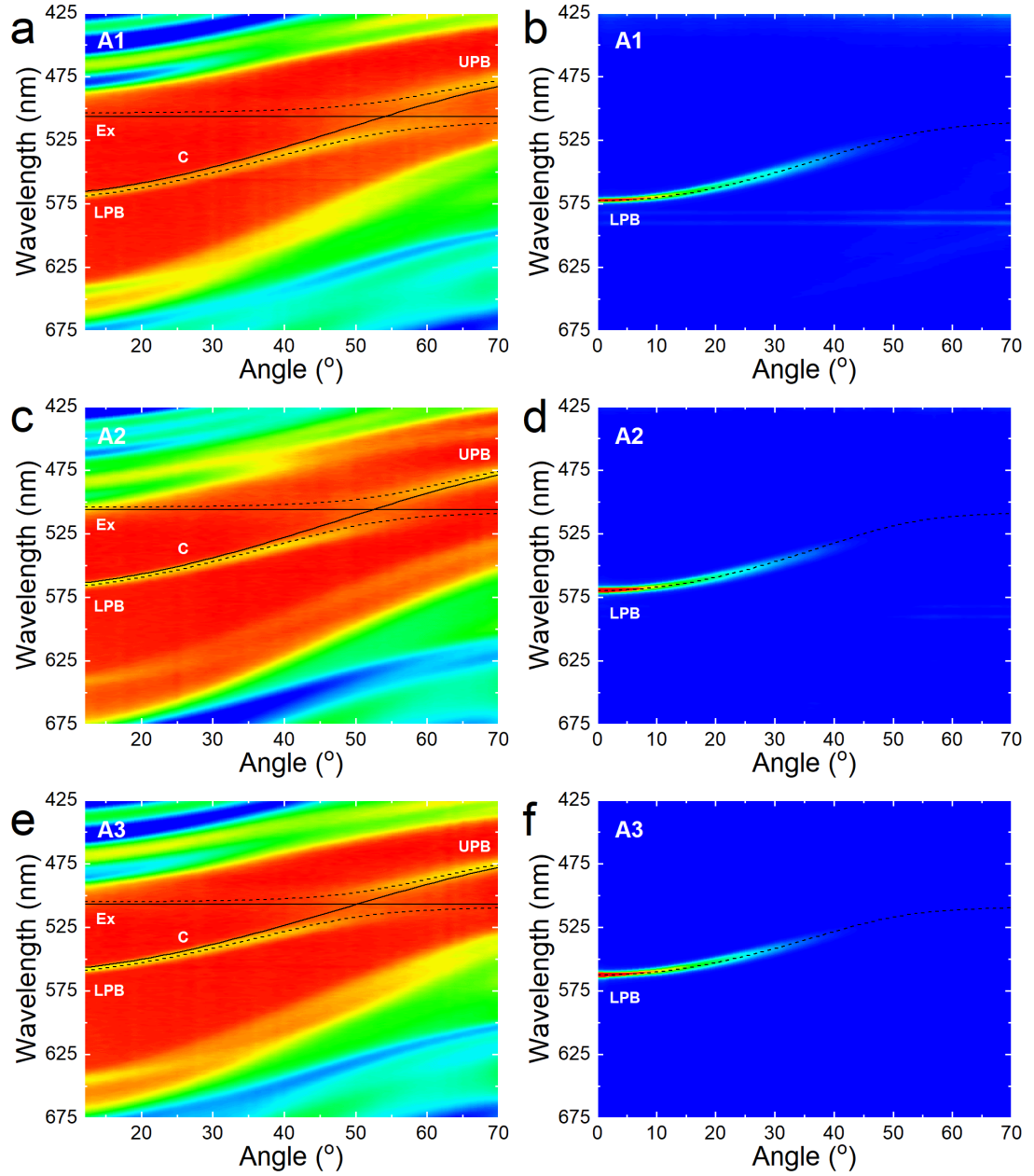


**Figure 3.12.** Unpolarized angular white-light reflectivity data and PL emission from a DBR-DBR microcavity containing the dye BODIPY-A1 parts (a) & (b), BODIPY-A2 parts (c) & (d) and BODIPY-A3 parts (e) & (f), along with the LPB and UPB (dashed lines) and photon (C) and exciton (Ex) energies (solid lines) extracted from a standard two-level coupled oscillator model.

as dashed (LPB and UPB) and solid (C and Ex) lines overlaying the experimental data. Strong coupling is manifested by a characteristic anticrossing of the LPB and UPB at the energy where the exciton and photon modes are degenerate. At this angle ( $\theta_{res}$ ) the energy separation between the two modes is at its minimum, corresponding to the Rabi splitting energy ( $\hbar\Omega_{rabi}$ ). Table 3.1 summarizes the values of  $C_{\theta=0}$ ,  $Ex$ ,

$\delta$  and  $\hbar\Omega_{rabi}$  extracted from the coupled oscillator model for the cavities shown in Figures 3.11 and 3.12.

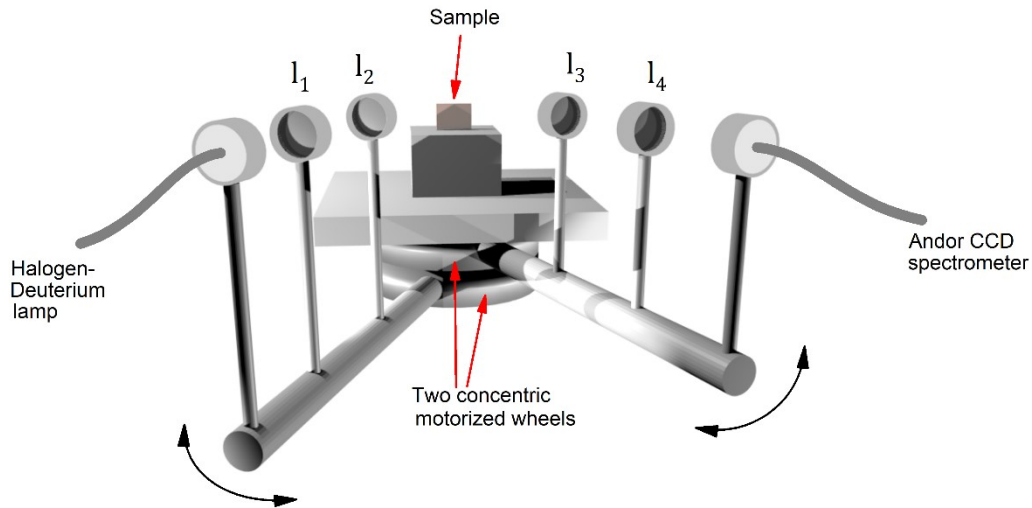


**Figure 3.13.** Schematic of the angular white-light reflectivity and PL setup showing the sample, the two concentric motorized wheels and the two rotating arms used to excite the cavity and detect light emitted or reflected from the cavity at different angles. Lenses  $l_1$ ,  $l_2$ ,  $l_3$  and  $l_4$  were used to collimate and focus the light beams.

Cavity	$E_x$ (eV)	$C_{\theta=0}$ (eV)	$\delta$ (meV)	$\hbar\Omega_{Rabi}$ (meV)
<b>E2</b>	2.475	2.190	285	75
<b>E3</b>	2.436	2.198	238	75
<b>A1</b>	2.449	2.178	271	120
<b>A2</b>	2.451	2.185	266	97
<b>A3</b>	2.446	2.213	233	93

**Table 3.1.** Exciton ( $E_x$ ) and photon ( $C_{\theta=0}$ ) energy values along with the photon-exciton detuning ( $\delta$ ) and the Rabi splitting energy ( $\hbar\Omega_{Rabi}$ ) of cavities with BODIPY E2-3 and A1-3 shown in Figures 3.11 and 3.12.

### 3.6. Analysis of PL distribution

The angular PL emission of the different cavities (Figure 3.11 (b) and (d) and Figure 3.12 (b), (d) and (f)) was analyzed in order to determine the polariton population distribution along the LPB at room temperature. This was achieved by dividing the peak PL intensity of each polariton state by its corresponding photon fraction. Results of this analysis are shown in Figure 3.14 (open squares) where we plot the normalized polariton population with energy for the different BODIPY microcavities.

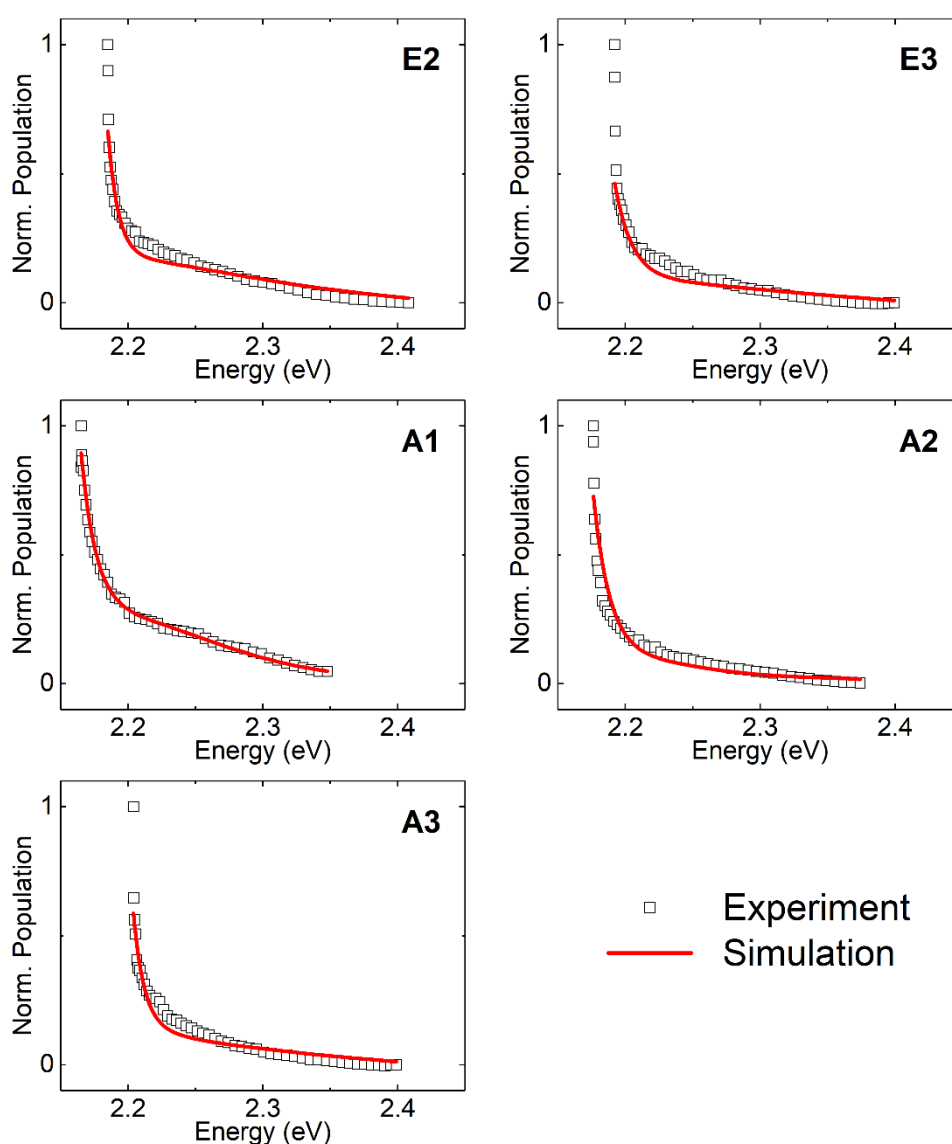


**Figure 3.14.** The open squares show the polariton population distribution along the LPB at room temperature that was obtained from microcavities containing the BODIPY derivatives E2, E3, A1, A2 and A3. The red solid lines are fits to the experimental data.

In a study by Grant et al.<sup>17</sup>, it was suggested that when strongly coupled microcavities containing the molecular dye BODIPY-Br are excited non-resonantly, an exciton reservoir (ER) of weakly coupled states is formed. States in this ER are then able to radiatively pump polaritons in the LPB, with the efficiency of this process being proportional to the photon fraction of the polaritons (see Equation 3.3).<sup>17</sup> The states responsible for pumping polaritons were identified as the weakly coupled 0-1 vibronic transition and excimers of the molecular dye. The authors used up to two Gaussian functions to describe the ER and the polariton population distribution of the LPB was simulated by multiplying these Gaussian functions with the photon fraction of the polaritons.<sup>17</sup>

$$W_{k \leftarrow x} = W_1 e^{\frac{-(E_k - E_1)^2}{2\sigma^2}} |a(k)|^2 \quad (3.3)$$

Here, we have used a similar approach to describe the population distribution of polaritons on the LPB. Surprisingly however, we found that this approach only provided an acceptable fit to the LPB at relatively high viewing angles ( $\theta > 20^\circ$ ). At small angles ( $\theta = 0^\circ \rightarrow 20^\circ$ ) however, it was found that there was a much larger population of polaritons than could be described using this model. Indeed, as can be seen in Figure 3.14, there is a very sharp increase in polariton density in all cavities around normal incidence.

To address this issue, we have added an extra term to the model as advanced by Grant et al.<sup>17</sup> and summarized in Equation 3.3. Here, we specifically included a term which arbitrarily describes a co-existing population of thermalized polaritons alongside the reservoir pumping term. We feel justified in doing this, as the Q-factor of the cavities explored here is around 3-4 times higher than those studied by Grant et al.,<sup>17</sup> and thus the enhanced stability of the polariton states may allow some degree of thermalization to occur.

Table 3.2 tabulates the centre energy and width of the Gaussian functions used to best fit the reservoir pumping term.

Cavity	$E_1$ (eV)	$\sigma_1$ (eV)	$E_2$ (eV)	$\sigma_2$ (eV)	$E_3$ (eV)	$\sigma_3$ (eV)	$E_4$ (eV)	$\sigma_4$ (eV)
<b>E2</b>	2.134	0.266	-	-	-	-	-	-
<b>E3</b>	2.147	0.256	-	-	-	-	-	-
<b>A1</b>	2.166	0.177	1.933	0.066	1.865	0.039	-	-
<b>A2</b>	2.206	0.099	2.072	0.169	1.873	0.039	1.872	0.237
<b>A3</b>	2.127	0.077	2.09	0.288	-	-	-	-

**Table 3.2.** Center energy ( $E$ ) and width ( $\sigma$ ) of the Gaussian functions that were used to fit the reservoir pumping term.

As it can be seen in Figure 3.14, this simple model allows us to obtain a relatively reasonable fit of the population distribution (fit shown using red solid line). However, the thermalisation temperatures extracted from this model range from 80 to 150 K and are thus rather unrealistic, as this temperature is much lower than the temperature at which the measurements were made.

A key assumption of our model is that thermalisation can occur within timescales defined by the lifetime of polaritons. The description of the ER using a series of simple Gaussian functions is also questionable. Nevertheless, the agreement between data and theory is reasonable. We believe therefore that our results must be considered as suggestive rather than conclusive, and we emphasize that a more detailed study is needed to identify the relaxation and population mechanisms of the system.

### 3.7. Conclusions

Six different BODIPY-core materials were introduced in this chapter. These dyes are highly fluorescent and make smooth and relatively uniform thin films when dispersed into a PS/toluene matrix. They have narrow linewidths and high oscillator strength making them good candidates as the active semiconductor in organic strongly coupled microcavities.

Before exploring their properties in microcavity structures, a series of experiments were conducted to study and understand their optical properties. It was concluded that the PLQY has a strong concentration dependence and the dyes seem to be stable following intense pulsed optical excitation. BODIPY-derivatives spin-cast onto quartz-coated glass substrates undergo optical gain, which leads to ASE following pulsed excitation using a stripe-pumping geometry. There is a clear concentration dependence on the ASE threshold as well as the peak ASE wavelength. Film thickness also affects the ASE threshold. These are explained with reference to a waveguide model and the photophysical properties of the dyes.

A series of DBR-DBR  $\lambda/2$  cavities were designed and fabricated containing BODIPY films in a PS matrix at 10% concentration by mass. Angular white-light reflectivity and PL measurements were used to show that these cavities enter the strong coupling regime. A two-level coupled oscillator model was used to model the energy of the polariton branches along with the photon and exciton mode energy and the Rabi splitting energy of the system. The polariton population distribution along the LPB was calculated using the PL data and the photon fraction of the polaritons. A simple model combining radiative pumping of polaritons from an exciton reservoir and a thermalisation term was then used to describe the experimental results.

All BODIPY derivatives have been proved to be good candidates for strong coupling experiments. In particular, BODIPY-Br exhibits high oscillator strength at moderate concentrations, and has a reasonably high PLQY, good optical gain and reasonable photostability. This material system has also the advantage of emitting luminescence at a spectral region not easily accessible using inorganic semiconductors, making it favorable system with which to explore non-linear effects in microcavities (see Chapter 4). As we discuss later in this thesis (Chapter 5), the slightly different exciton

energy of the BODIPY derivatives can allow two different dyes to be combined in a microcavity and then hybridized to the same optical mode.

### 3.8. References

1. Tropf, L. *et al.* Influence of optical material properties on strong coupling in organic semiconductor based microcavities. *Appl. Phys. Lett.* (2017). doi:10.1063/1.4978646
2. Grant, R. T. *et al.* Strong coupling in a microcavity containing  $\beta$  - carotene. *Opt. Express* **26**, 3320–3327 (2018).
3. Bergström, F. *et al.* Dimers of Dipyrrometheneboron Difluoride (BODIPY) with light spectroscopic applications in chemistry and biology. *J. Am. Chem. Soc.* **124**, 196–204 (2002).
4. Kim, H. N., Ren, W. X., Kim, J. S. & Yoon, J. Fluorescent and colorimetric sensors for detection of lead, cadmium, and mercury ions. *Chem. Soc. Rev.* **41**, 3210–3244 (2012).
5. Loudet, A. & Burgess, K. BODIPY dyes and their derivatives: Syntheses and spectroscopic properties. *Chem. Rev.* **107**, 4891–4932 (2007).
6. Ulrich, G., Ziesel, R. & Harriman, A. The chemistry of fluorescent bodipy dyes: Versatility unsurpassed. *Angew. Chemie - Int. Ed.* **47**, 1184–1201 (2008).
7. Gupta, N. *et al.* A bodipy based dual functional probe for the detection of hydrogen sulfide and H<sub>2</sub>S induced apoptosis in cellular systems. *Chem. Commun.* **51**, 10875–10878 (2015).
8. Wang, Z., Xie, Y., Xu, K., Zhao, J. & Glusac, K. D. Diiodobodipy-styrylbodipy Dyads: Preparation and Study of the Intersystem Crossing and Fluorescence Resonance Energy Transfer. *J. Phys. Chem. A* **119**, 6791–6806 (2015).
9. Gai, L. *et al.* New 2,6-distyryl-substituted BODIPY isomers: Synthesis, photophysical properties, and theoretical calculations. *Chem. - A Eur. J.* **20**, 1091–1102 (2014).
10. Yang, Z. *et al.* A self-calibrating bipartite viscosity sensor for mitochondria. *J. Am. Chem. Soc.* **135**, 9181–9185 (2013).
11. Aydın Tekdaş, D. *et al.* Antimicrobial activity of a quaternized BODIPY

- against *Staphylococcus* strains. *Org. Biomol. Chem.* **14**, 2665–2670 (2016).
12. Imahori, H. *et al.* Light-harvesting and photocurrent generation by gold electrodes modified with mixed self-assembled monolayers of boron-dipyrin and ferrocene-porphyrin-fullerene triad. *J. Am. Chem. Soc.* **123**, 100–110 (2001).
  13. Nepomnyashchii, A. B., Bröring, M., Ahrens, J. & Bard, A. J. Chemical and electrochemical dimerization of BODIPY compounds: Electrogenerated chemiluminescent detection of dimer formation. *J. Am. Chem. Soc.* **133**, 19498–19504 (2011).
  14. Nöll, G., Daub, J., Lutz, M. & Rurack, K. Synthesis, spectroscopic properties, and electropolymerization of azulene dyads. *J. Org. Chem.* **76**, 4859–4873 (2011).
  15. Musser, A. J. *et al.* Intermolecular states in organic dye dispersions: excimers vs. aggregates. *J. Mater. Chem. C* **5**, 8380–8389 (2017).
  16. Musser, A. J. *et al.* Supplementary Information: Intermolecular states in organic dye dispersions: excimers vs. aggregates. *J. Mater. Chem. C* **5**, 8380–8389 (2017).
  17. Grant, R. T. *et al.* Efficient Radiative Pumping of Polaritons in a Strongly Coupled Microcavity by a Fluorescent Molecular Dye. *Adv. Opt. Mater.* (2016).
  18. Hvam, J. M. Direct recording of optical-gain spectra from ZnO. *J. Appl. Phys.* **49**, 3124–3126 (1978).
  19. Cookson, T. *et al.* A Yellow Polariton Condensate in a Dye Filled Microcavity. *Adv. Opt. Mater.* **5**, 1700203 (2017).
  20. Daskalakis, K. S., Maier, S. A., Murray, R. & Kéna-cohen, S. Nonlinear interactions in an organic polariton condensate. *Nat. Mater.* **13**, 271–278 (2014).
  21. Kéna-cohen, S. & Forrest, S. R. Room-temperature polariton lasing in an organic single-crystal microcavity. *Nat. Photonics* **4**, 371–375 (2010).

22. Calzado, E. M., Villalvilla, J. M., Boj, P. G., Quintana, J. A. & Diaz-Garcia, M. A. Tuneability of amplified spontaneous emission through control of the thickness in organic-based waveguides. *J. Appl. Phys.* **97**, 93103 (2005).
23. Calzado, E. M., Villalvilla, J. M., Boj, P. G., Quintana, J. a. & Díaz-García, M. A. Concentration dependence of amplified spontaneous emission in organic-based waveguides. *Org. Electron. physics, Mater. Appl.* **7**, 319–329 (2006).
24. Kazlauskas, K. *et al.* Concentration effects on spontaneous and amplified emission in benzo[c]fluorenes. *Phys. Chem. Chem. Phys.* 9–11 (2015).

## Chapter 4. A yellow polariton condensate in a dye filled microcavity

### 4.1. Motivation of work

Because strongly coupled organic semiconductor microcavities operate at room temperature, they are a popular platform to study macroscopic quantum phenomena, with a number of researchers now considering practical applications of this technology. When this project was initiated, organic polariton lasers and condensates had only recently been reported<sup>1-3</sup> using pure films of chromophores placed between two mirrors. Such systems operated at room temperature and emitted light between 420 nm and 475 nm. In the following paper, we report a polariton condensate at room temperature that emits light in the yellow spectral region, a wavelength that is difficult to engineer using traditional inorganic semiconductors. Importantly, we use a dilute system in which small fluorescent molecules (BODIPY-Br) are dispersed in an inert polymeric matrix. This allows us to tune both the light-matter interaction strength and the photoluminescence quantum efficiency of the active layer through the dye/polymer concentration ratio. The new material system that we create opens the field to using a range of commercially available fluorescent molecular dyes blended in an inert matrix in microcavities; a prospect that will allow tuning of the polariton lasing wavelength over the entire visible spectrum to the near-IR.

### References

1. Kéna-cohen, S. & Forrest, S. R. Room-temperature polariton lasing in an organic single-crystal microcavity. *Nat. Photonics* **4**, 371–375 (2010).
2. Daskalakis, K. S., Maier, S. A., Murray, R. & Kéna-cohen, S. Nonlinear interactions in an organic polariton condensate. *Nat. Mater.* **13**, 271–278 (2014).
3. Plumhof, J. D., Stoeferle, T., Mai, L., Scherf, U. & Mahrt, R. F. Room-Temperature Bose-Einstein Condensation of cavity exciton-polariton in a polymer. *Nat. Mater.* **13**, 247–252 (2014).

## 4.2. Author contributions

T.C. and K.G. contributed equally to this work. K.G. studied the photophysics of BODIPY materials and found suitable derivatives for polariton condensation. K.G. designed and fabricated the microcavity structures. K.G. performed the white-light reflectivity measurements and characterized the steady state photoluminescence from the strongly coupled microcavities and control non-cavity films. T.C. contributed to the non-linear spectroscopy, with power dependent measurements and interferometry. A.Z. performed the ASE measurements. K.G., T.C. and R.T.G. analysed the data. M.C., F.G., T.V. synthesized and provided the BODIPY-Br. C.C. from Helia Photonics Ltd (industrial collaborator) was involved with the growth of the DBRs. K.G. and T.C. wrote the manuscript with significant input from D.G.L. and P.G.L.. N.G.B., D.G.L. and P.G.L. supervised the project.

## 4.3. Publication

In the following, we present the publication as it appears online in the Journal Advanced Optical Materials.

“Reprinted with permission from Cookson T. and Georgiou K. et al., A yellow polariton condensate in a dye filled microcavity, *Adv. Opt. Mater.* 2017, 5, 18, 1700203. Copyright (2018) John Wiley and Sons.”

## A Yellow Polariton Condensate in a Dye Filled Microcavity

Tamsin Cookson, Kyriacos Georgiou, Anton Zasedatelev, Richard T. Grant, Tersilla Virgili, Marco Cavazzini, Francesco Galeotti, Caspar Clark, Natalia G. Berloff, David G. Lidzey,\* and Pavlos G. Lagoudakis\*

**Polariton condensation in the yellow part of the visible spectrum from a planar organic semiconductor microcavity containing the molecular dye bromine-substituted boron-dipyrromethene is observed. This study provides experimental fingerprint of polariton condensation under nonresonant optical excitation, including the nonlinear dependence of the emission intensity and wavelength blueshift with increasing excitation density, single excitation pulse dispersion imaging, and real space interferometry. The latter two allow to visualize the collapse of the energy distribution and the long-range coherence of the polariton condensate.**

Bose–Einstein condensation (BEC) is an exotic state of matter, wherein particles coalesce to a macroscopically occupied coherent state. BECs have been observed for a broad range of systems such as  $^4\text{He}$ ,<sup>[1]</sup> alkali-metal atoms,<sup>[2]</sup> magnons,<sup>[3]</sup> and polaritons.<sup>[4]</sup> Beyond the beauty of the underlying physics describing the fundamental properties and dynamics of BECs,<sup>[5]</sup> there is a range of applications that utilize the coherence of their massive wavefunctions, especially in the rapidly developing field of quantum technologies.<sup>[6]</sup> Unlike other BECs, polariton

condensates (hosted in semiconductor slabs embedded in optical cavities) can optically be pumped, and more importantly are interrogated through photoluminescence (PL). Indeed, due to finite cavity lifetimes, polaritons decay in the form of photons that carry all information of the corresponding polariton state (energy, momentum, spin, and phase). By appropriate choice of the crystalline semiconductor host, polariton condensates can form even at room temperature.<sup>[7,8]</sup> Circumventing the challenges of epitaxial growth, polariton condensates were also realized in soft-matter organic

microcavities.<sup>[9,10]</sup> The room temperature operation and ease with which organic polariton condensates can be “written” and “read” is attractive for imprinting polariton lattices, a promising platform for quantum simulators.<sup>[11]</sup>

A number of very different molecular systems have been used to date as the semiconductor host in optical cavities to demonstrate polariton condensation, varying from crystalline anthracene to oligofluorenes, conjugated polymers and fluorescent proteins.<sup>[9,10,12,13]</sup> Although the chemical structure and morphology of these molecular hosts are very dissimilar, all three have relatively narrow absorption spectra and small Stokes shift with respect to their optical oscillator strengths. These features are necessary for strong coupling, but not sufficient for polariton condensation. For example, J-aggregates have very similar spectroscopic characteristics with the above molecular systems allowing for strong coupling, however, in J-aggregates polariton condensates remains elusive even under resonant excitation schemes.<sup>[14]</sup> A characteristic of the molecular systems that have exhibited polariton condensation is their relatively high quantum yield (QY), >10%, even with increasing excitation densities. It is plausible that a key ingredient for polariton condensation in molecular systems is the balance between radiative and nonradiative decay paths, since the latter will limit the number of excitons available to form polaritons. Undoubtedly, there is still a plethora of molecular systems that satisfy the above conditions and other considerations should be taken into account to address limitation beyond the formation of a polariton condensate. For any application that utilizes the macroscopic wavefunction of organic polariton condensates to become viable, control over the disorder and its adverse effects on spatial coherence and homogeneity of the polariton energy landscape need to be addressed. Here, we demonstrate evidence of polariton condensation in a different class of organic semiconductors, that of a molecular dye diluted in a matrix polymer, resulting in extended polariton condensates.

T. Cookson, P. G. Lagoudakis  
Department of Physics and Astronomy  
The University of Southampton  
University Road, Southampton SO17 1BJ, UK  
E-mail: pavlos.lagoudakis@soton.ac.uk

K. Georgiou, R. T. Grant, D. G. Lidzey  
Department of Physics and Astronomy  
The University of Sheffield  
Hicks Building, Hounsfield Road, Sheffield S3 7RH, UK  
E-mail: d.g.lidzey@sheffield.ac.uk

A. Zasedatelev, N. G. Berloff, P. G. Lagoudakis  
Skolkovo Institute of Science and Technology  
Moscow 143026, Russia

T. Virgili, M. Cavazzini, F. Galeotti  
IFN  
ISMAR and ISTM – CNR, 20133 Milano, Italy

C. Clark  
Helia Photonics Ltd  
2 Rosebank Rd, Livingston EH54 7EJ, UK

N. G. Berloff  
Department of Applied Mathematics and Theoretical Physics  
University of Cambridge  
Cambridge CB3 0WA, UK

 The ORCID identification number(s) for the author(s) of this article can be found under <https://doi.org/10.1002/adom.201700203>.

DOI: 10.1002/adom.201700203

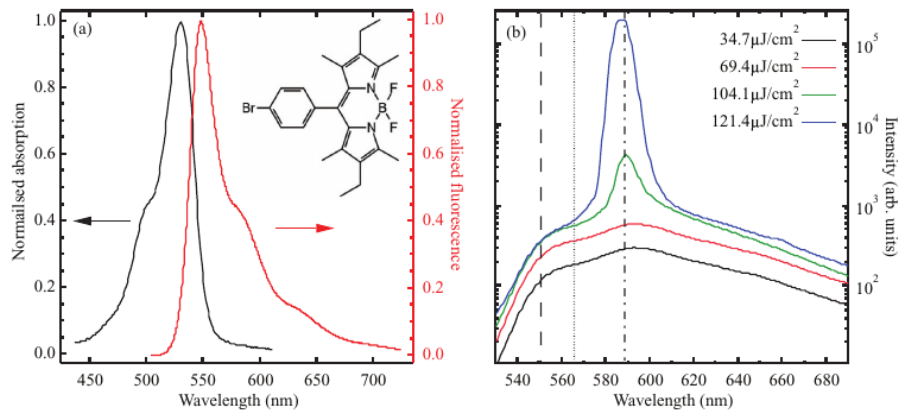


**Figure 1.** a) The normalized absorption (black) and fluorescence spectrum (red) of BODIPY-Br dispersed in a transparent polystyrene matrix. The chemical structure is shown in the insert. b) Amplified spontaneous emission from a 186 nm thick film of the BODIPY-Br dispersed in a polystyrene matrix and deposited on a quartz substrate. A threshold is observed at a pump fluence of  $104.1 \mu\text{J cm}^{-2}$  with a peak forming at 589 nm (dashed-dotted line). The dotted line indicates the polariton emission from the microcavity, while the large dashed line indicates the fluorescence emission peak shown in (a).

The material investigated is a bromine-substituted boron-dipyrromethene (BODIPY-Br) that combines relatively high photoluminescence quantum yield, between 10% and 50% (dependent on sample preparation conditions), with fluorescence emission around 550 nm.<sup>[15]</sup> To incorporate BODIPY-Br into a microcavity, it is necessary to disperse it into a transparent polymeric matrix at relatively low concentration to limit unwanted molecular aggregation and luminescence quenching phenomena.<sup>[16–18]</sup> This approach to creation of a medium is different from previous studies in which a pure film of organic chromophores was used.<sup>[9,12]</sup>

**Figure 1a** shows the chemical structure of the molecular dye BODIPY-Br, together with its absorption and fluorescence when dispersed into a transparent polystyrene matrix at a concentration of 10% by mass. It can be seen that the absorption maximum of BODIPY-Br peaks at 530 nm, while its fluorescence maximum is redshifted to 550 nm. We have previously explored the photophysics of microcavities containing BODIPY-Br, and have concluded that weakly coupled excimer-like states, together with emission from the (0,1) vibrational transition that are both located around 593 nm are responsible for optically pumping polariton states along the lower polariton branch.<sup>[15]</sup>

To explore the nonlinear emission properties of BODIPY-Br, we used a stripe-pumping geometry to generate amplified spontaneous emission from a noncavity control film. Here a 186 nm thick noncavity film of BODIPY-Br in polystyrene (10% by mass) was spin-cast onto a quartz substrate and then pumped using 100 fs laser pulses at a repetition rate of 1 kHz at 500 nm along a 20 mm long stripe. **Figure 1b** shows emission from the film at various pump fluences. Here, it can be seen that at threshold of  $104.1 \mu\text{J cm}^{-2}$ , there is a strong increase in emission at around 589 nm with the emergence of a peak having a linewidth of around  $\approx 8$  nm (28 meV). This wavelength approximately coincides with the (0,1) vibrational transition, suggestive of a 4-level lasing system. This measurement usefully indicates that BODIPY-Br can support optical amplification, which is indicative of low optical losses under high excitation density,

rendering it a promising candidate for realizing polariton condensation.

We fabricate BODIPY-Br into a microcavity by spin-casting a 186 nm thin film onto a distributed Bragg reflector (DBR) consisting of 10 pairs of  $\text{SiO}_2/\text{Nb}_2\text{O}_5$ . We deposit a second 8-pair  $\text{SiO}_2/\text{Nb}_2\text{O}_5$  DBR onto the BODIPY-Br film using ion assisted electron beam and reactive sublimation, as shown in the schematic of the cavity structure in **Figure 2a**. The measured Q-factor of the resulting cavity is  $\approx 440$  corresponding to a cavity lifetime of 133 fs. **Figure 2b** shows white light reflectivity spectra as a function of the off-axis viewing angle, where the measurements are made through the 8-pair DBR. It can be seen that two optical modes are clearly visible undergoing anticrossing around a wavelength of 530 nm; a wavelength that we associate with the (0,0) monomer absorption transition of the BODIPY-Br. **Figure 2c** shows the energy of the upper and lower polariton branches determined from the reflectivity measurements. The data are fitted to a standard two-level oscillator model from which we obtain a Rabi-splitting energy of 91 meV. The energy of the exciton energy of the fit (2.33 eV) closely coincides with the peak absorption energy of the BODIPY-Br (0,0) electronic transition (2.34 eV). We overlay the dispersion plot with an intensity map of the photoluminescence emitted by the cavity under nonresonant pumping. Here, we excite our sample using a bandpass filter centered at 450 with 10 nm bandwidth to spectrally filter a 6 ps pulsed super-continuum laser operating at 40 MHz. The excitation density for these measurements is  $1.2 \mu\text{J cm}^{-2}$ . It can be seen that the cavity emission is most intense around the bottom of the lower polariton branch (corresponding to  $k_{\parallel} = 0$ ), and reduces in intensity toward the energy of the uncoupled exciton. We have previously shown that the distribution of emission along the lower polariton branch (LPB) is primarily determined by the distribution of weakly coupled states within the exciton reservoir.<sup>[15]</sup> **Figure 2d** shows the free space yellow emission from our cavity under nonresonant pumping.

We investigate the nonlinear photoluminescence dynamics using 2 ps optical pulses at 400 nm. The sample is held in a

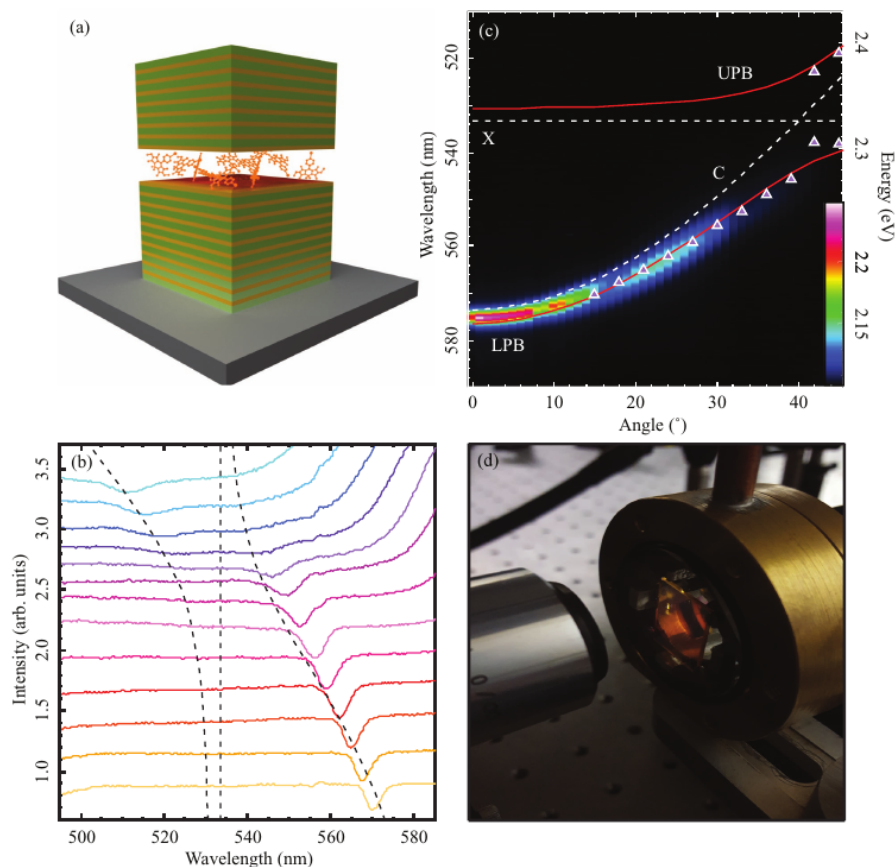


**Figure 2.** a) Schematic of the dye filled microcavity. b) Reflectivity spectra taken first at an angle of 15° (light orange) and at every successive 3° up to 51° (light blue). The lower polariton branch is observed clearly in the smaller angles (orange to pink), while the anticrossing can be observed from 42° (dark purple) with the upper polariton branch becoming visible from that point onwards. The dashed lines indicate the upper polariton branch, exciton, and lower polariton branch from left to right. c) Polariton dispersion in the linear regime. The dispersion of the upper polariton (UPB) and lower polariton (LPB) branches are fitted using a standard two level oscillator model (red lines). The peaks from the reflectivity spectra in (b) are plotted as purple triangles showing a good fit to the polariton branches. d) An image of the microcavity held in a vacuum chamber showing the yellow emission of the polariton condensate.

vacuum chamber at  $10^{-6}$  mbar at room temperature. The full width at half maximum of the pump beam on the sample is  $\approx 8$   $\mu\text{m}$ . Photoluminescence is collected using a lens with 0.42 numerical aperture that allows for dispersion and real space imaging using an electron multiplying charge coupled device (EMCCD) camera at the exit slit of a 55 cm spectrophotometer and a grating of 1200 grooves  $\text{mm}^{-1}$ . We have synchronized the timing of the optical detection system with the train of excitation pulses down to a single pulse excitation/image acquisition. Using the setup described above we can perform single pulse excitation dispersion imaging. Also with the use of a stabilized Michelson interferometer, we can record interferograms that allow us to measure the extent of the coherence of the emissive states under single pulse excitation.

Figure 3a–c) shows dispersion images recorded below, near and twice above threshold. Figure 3a shows the linear dispersion time averaged over 1500 excitation pulses. With increasing pump intensity, at a threshold excitation density we observe the collapse of the emission to the bottom of the

polariton dispersion, centered on  $k_{\parallel} = 0$ , as shown in the dispersion image of Figure 3b that is time averaged over 2 excitation pulses. Figure 3c shows the dispersion image at approximately twice above threshold, integrated over 4 excitation pulses, where the emission appears blueshifted with respect to the linear regime. In Figure 3d, we plot the photoluminescence spectra extracted at  $k_{\parallel} = 0$  from dispersion images recorded for different pump intensities and normalized to the number of excitation pulses used per recording. Evidently, as the pump intensity increases the spectrum gets narrower and blueshifts with respect to the spectrum at the lowest excitation density (black curve in Figure 3d). In Figure 3e, we plot the integrated intensity of the above spectra and the corresponding linewidth measured at FWHM as a function of the upper bound of the threshold excitation density ( $527.3 \mu\text{J cm}^{-2}$ ). We observe a threshold-like behavior at  $527.3 \mu\text{J cm}^{-2}$  accompanied by a reduction in linewidth from 2.8 to 0.5 nm. Figure 3f shows a continuous blueshift of the photoluminescence spectrum, up to 5 meV at twice the threshold density, of similar magnitude

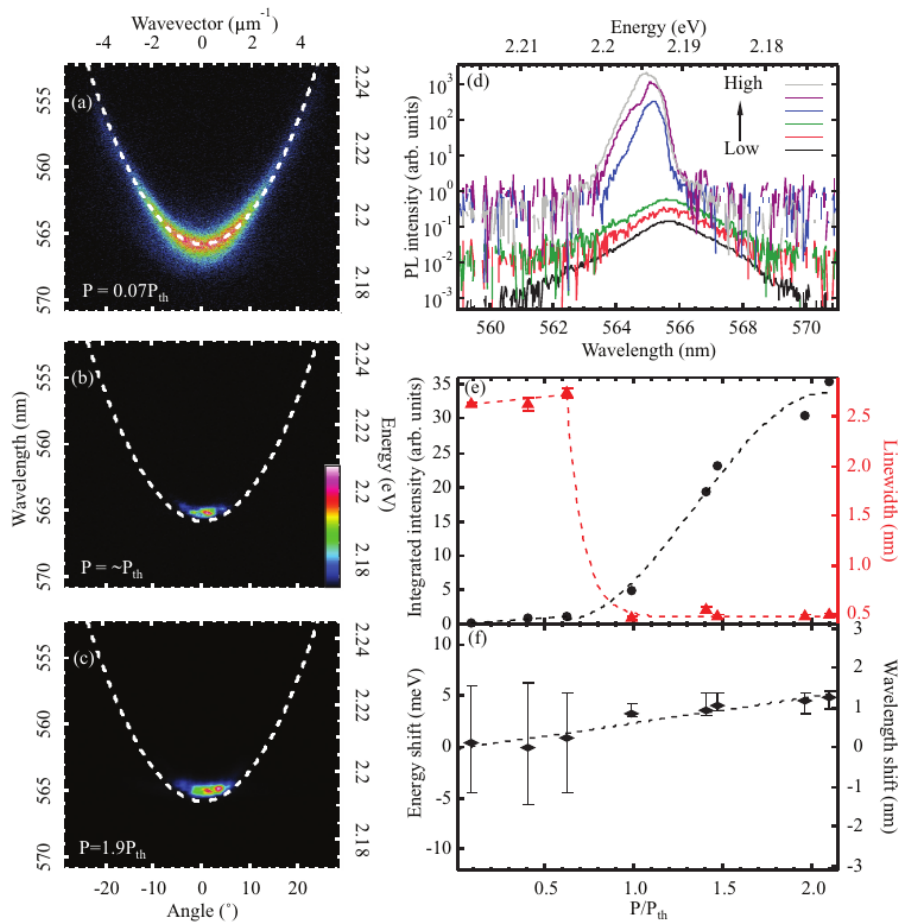


**Figure 3.** a–c) Normalized dispersions taken below threshold, near threshold, and above threshold. The white dashed line indicates the linear regime. d) Photoluminescence spectra extracted at  $k_{||} = 0$  from dispersion images recorded for different pump intensities and normalized to the number of excitation pulses used per recording. e) Integrated intensity of the spectra and the corresponding linewidth measured at full width at half maximum (FWHM) as a function of threshold excitation density. f) Energy shift of the photoluminescence spectrum as a function of threshold excitation density.

to that observed by Plumhof et al.,<sup>[10]</sup> in a cavity containing a conjugated polymer. In areas on the sample where we do not observe polariton condensation, there is no visible blueshift of the dispersion. For the detuning used here, we calculate the exciton content,  $|X_{LP}|^2$ , to be 0.103 at  $k_{||} = 0$  of the lower polariton branch. We note here that by ramping the excitation density twice above threshold and back to the linear regime the optical properties of the sample remain virtually unchanged, including the shape of the photoluminescence spectrum. The observed nonlinearity on the excitation density associated with the continuous blueshift of the photoluminescence spectrum provides strong evidence of polariton condensation.

Figure 4a shows the interferogram of a polariton condensate at threshold excitation density for a single excitation pulse utilizing a stabilized Michelson interferometer equipped with a retro-reflector to generate optical interference between the emitted light by the cavity and its inverted image. This technique has been utilized to realize experimentally the long range phase coherence of the condensate in many previous organic condensate studies.<sup>[19–22]</sup> The interference fringes across the

image are plotted in Figure 4b and are fitted with a convoluted Gaussian (red curve). The visibility contrast of 86% indicates a high degree of spatial coherence across the condensate that extends beyond the excitation spot. From the standard deviation of the Gaussian fit we calculate a coherence length of  $28 \mu\text{m}$  from  $\lambda_c = 2\sqrt{2\pi}\sigma$ , suggesting a homogeneous polariton energy landscape of the same order.

In conclusion, we report on a yellow polariton condensate in a dye filled microcavity. We obtain strong evidence of nonlinear photoluminescence with increasing excitation density, associated with a sixfold linewidth narrowing and a continuous blueshift attributed to polariton interactions with other polaritons and the exciton reservoir. The wavelength of the polariton condensate is blueshifted with respect to the wavelength, where amplified spontaneous emission occurs in BODIPY-Br (565 and 589 nm, respectively) indicating that the nonlinearity does not necessarily coincide with the point of maximum gain of the molecular dye. Furthermore, single shot interferometry reveals substantial long range coherence across the condensate and uniformity of the polariton energy

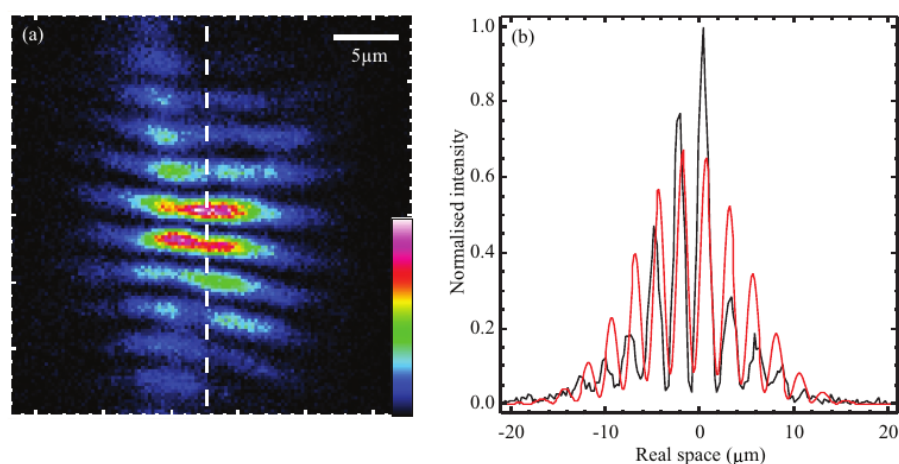


**Figure 4.** a) Interferogram of a polariton condensate at threshold excitation density for a single excitation pulse. b) Intensity profile (black line) taken along the white dashed line of (a) and the corresponding Gaussian fit to the data (red curve).

landscape. The latter is important for expanding this work to lattices of polariton condensates and their applications in polariton simulators. It is conceivable that there is a large number of different molecular dyes that could be dispersed into a polymer matrix and embedded in a cavity that would allow for polariton condensation to be realized at wavelengths spanning the entire visible and near infrared. This wavelength selectivity could become of interest in the development of future optoelectronic devices, including hybrid organic–inorganic polariton laser diodes.

## Experimental Section

**Sample Preparation:** A polymer matrix solution was prepared using polystyrene (PS) having an average molecular weight ( $M_w$ ) of  $\approx 192\,000$  in toluene at a concentration of  $35\text{ mg mL}^{-1}$ . The PS/toluene solution was heated up to a temperature of  $70\text{ }^\circ\text{C}$  and stirred for 30 min. BODIPY-Br was then added to the solution at a concentration of 10% by mass. Noncavity films for absorption, photoluminescence, and ASE measurements were spin-cast onto quartz-coated glass substrates.

For the microcavity fabrication a bottom 10-pair DBR of  $\text{SiO}_2/\text{Nb}_2\text{O}_5$  was deposited onto quartz-coated glass substrates using ion assisted electron beam ( $\text{Nb}_2\text{O}_5$ ) and thermal evaporation ( $\text{SiO}_2$ ). The 186 nm thick BODIPY-Br active layer was then spin-coated on top of the bottom mirror. A second 8-pair DBR was deposited on top of the organic with the ion gun kept turned-off during the first few layers to avoid any damage on the organic material.

**Spectroscopy:** The absorption and PL measurements of the BODIPY-Br noncavity films were performed using a Fluoromax 4 fluorometer (Horiba) that utilizes a Xe lamp. The angular white light reflectivity measurement was performed using a fiber-coupled Halogen–Deuterium white light source. A motorized arm was used to allow for the different illumination angles between the sample and the white light source. The reflected light was collected and coupled into an optical fiber mounted on a second motorized arm and then sent into a Andor Shamrock CCD spectrometer.

Angular PL measurement was performed using the same motorized goniometer setup described earlier. A fiber-coupled Fianium supercontinuum laser with 6 ps pulses and 40 MHz repetition rates was

used to nonresonantly excite the sample at 450 nm using a bandpass filter. The sample was excited at a fixed angle of  $45^\circ$  following a slight downward tilt to the optical axis to avoid collection of the reflected excitation beam. An optical fiber on a motorized arm was used to collect a range of different angles with a resolution of  $1^\circ$ . The excitation density of the laser was kept relatively low ( $1.2\text{ }\mu\text{J cm}^{-2}$ ).

The ASE measurements were carried out using optical parametric amplifier (Coherent OPerA SOLO) pumped by high energy Ti:sapphire regenerative amplifier system (Coherent Libra-HE) providing up to 200  $\mu\text{J}$  per pulse at 500 nm, with 100 fs pulse duration, and 1 kHz repetition rate. Line distributed beam was produced by Thorlabs ED1-L4100 line pattern diffuser and focused on the sample using 25.4 mm lens providing  $0.173 \times 20\text{ mm}$  vertically polarized beam on the sample. Stimulated emission of BODIPY-Br thin film was detected from the edge of the film, in the direction of the strip and perpendicular to the propagation direction of the incident pump beam using Ocean Optics QE PRO spectrometer (0.7 nm spectral resolution). All measurements were performed at room temperature in air.

For the condensation study, the microcavity was excited nonresonantly at a wavelength of 400 nm using pulses at a 50 kHz repetition rate and a pulse width  $< 2\text{ ps}$  from a regenerative amplifier (Rega 9000 pumped with a Verdi V10, Coherent) seeded by a mode-locked picosecond Ti:Sapphire oscillator (Mira 900, coherent, pumped by the Millennia X<sub>s</sub>, Spectra Physics) which was frequency-doubled through an optical parametric amplifier (OPA, Coherent). To prevent photo-oxidation of the sample, two optical choppers in a master-slave configuration with a modulation frequency of 28 Hz were used in conjunction with an optical shutter. This limited sample excitation to between 1 and 5 pulses over a 30 ms exposure time. The sample was mounted in a vacuum chamber held under a dynamic vacuum of  $10^{-6}$  mbar to further reduce photo-oxidation.

Photoluminescence was collected in transmission using an apochromatic Mitutoyo 50x microscope objective with a numerical aperture of 0.42 and focused into a 550 nm spectrometer (Horiba Triax 550) coupled to an electron multiplying CCD with a 500 nm long-pass filter blocking the residual light from the excitation beam. The PL was spectrally and in-plane wavevector resolved using a 1200 grooves  $\text{mm}^{-1}$  grating and a slit width of 100  $\mu\text{m}$  at the entrance of the spectrometer. The spatial coherence measurements were obtained by splitting the PL with a nonpolarizing beam splitter in a Michelson interferometer configuration with the mirror on one arm replaced by a retroreflector. The PL was then coupled into the spectrometer with the grating at zero order to spatially resolve the PL on the EMCCD.

## Acknowledgements

T.C. and K.G. contributed equally to this work. The authors thank the EPSRC for funding this research through the Programme Grant No. EP/M025330/1 "Hybrid Polaritonics" and for funding Ph.D. scholarships for T.C., K.G., and R.T.G. through institutional DTP allocations. K.G. fabricated the sample and characterized the linear dynamics of the microcavity. T.C. contributed the nonlinear spectroscopy and A.Z. contributed the ASE measurements. The data from this paper can be obtained from University of Southampton Institutional repository DOI: <http://doi.org/10.5258/SOTON/D0125>.

## Conflict of Interest

The authors declare no conflict of interest.

## Keywords

BODIPY-Br, polaritons, polariton condensates

Received: March 3, 2017

Revised: May 2, 2017

Published online:

- [1] F. Pereira Dos Santos, J. Léonard, J. Wang, C. J. Barrelet, F. Perales, E. Rasel, C. S. Unnikrishnan, M. Leduc, C. Cohen-Tannoudji, *Phys. Rev. Lett.* **2001**, *86*, 3459.
- [2] M. H. Anderson, J. R. Ensher, M. R. Matthews, C. E. Wieman, E. A. Cornell, *Science* **1995**, *269*, 198.
- [3] V. Zapf, M. Jaime, C. D. Batista, *Rev. Mod. Phys.* **2014**, *86*, 563.
- [4] J. Kasprzak, M. Richard, S. Kundermann, A. Baas, P. Jeambrun, J. M. J. Keeling, F. M. Marchetti, M. H. Szymańska, R. André, J. L. Staehli, V. Savona, P. B. Littlewood, B. Deveaud, L. S. Dang, *Nature* **2006**, *443*, 409.
- [5] J. R. Anglin, W. Ketterle, *Nature* **2002**, *416*, 211.
- [6] K. R. Patton, U. R. Fischer, *Phys. Rev. A* **2013**, *87*, 52303.
- [7] G. Christmann, R. Butté, E. Feltin, J.-F. Carlin, N. Grandjean, *Appl. Phys. Lett.* **2008**, *93*, 51102.
- [8] T.-C. Lu, Y.-Y. Lai, Y.-P. Lan, S.-W. Huang, J.-R. Chen, Y.-C. Wu, W.-F. Hsieh, H. Deng, *Opt. Express* **2012**, *20*, 5530.
- [9] K. S. Daskalakis, S. A. Maier, R. Murray, S. Kéna-Cohen, *Nat. Mater.* **2014**, *13*, 271.
- [10] J. D. Plumhof, T. Stoferle, L. Mai, U. Scherf, R. F. Mahrt, *Nat. Mater.* **2014**, *13*, 328.
- [11] N. G. Berloff, K. Kalinin, M. Silva, W. Langbein, P. G. Lagoudakis, *ArXiv:160706065 Cond-Mat Physicsquant-Ph* **2016**.
- [12] S. Kéna-Cohen, S. R. Forrest, *Nat. Photonics* **2010**, *4*, 371.
- [13] C. P. Dietrich, A. Steude, L. Töpf, M. Schubert, N. M. Kronenberg, K. Ostermann, S. Höfling, M. C. Gather, *Sci. Adv.* **2016**, *2*, e1600666.
- [14] N. Somaschi, L. Mouchliadis, D. Coles, I. E. Perakis, D. G. Lidzey, P. G. Lagoudakis, P. G. Savvidis, *Appl. Phys. Lett.* **2011**, *99*, 143303.
- [15] R. T. Grant, P. Michetti, A. J. Musser, P. Gregoire, T. Virgili, E. Vella, M. Cavazzini, K. Georgiou, F. Galeotti, C. Clark, J. Clark, C. Silva, D. G. Lidzey, *Adv. Opt. Mater.* **2016**, *4*, 1615.
- [16] T. T. Vu, M. Dvorko, E. Y. Schmidt, J. F. Audibert, P. Retailleau, B. A. Trofimov, R. B. Pansu, G. Clavier, R. Méallet-Renault, *J. Phys. Chem. C* **2013**, *117*, 5373.
- [17] I. Mikhalyov, N. Gretskaya, F. Bergström, L. B.-A. Johansson, *Phys. Chem. Chem. Phys.* **2002**, *4*, 5663.
- [18] S. Choi, J. Bouffard, Y. Kim, *Chem. Sci.* **2014**, *5*, 751.
- [19] H. Deng, G. S. Solomon, R. Hey, K. H. Ploog, Y. Yamamoto, *Phys. Rev. Lett.* **2007**, *99*, 126403.
- [20] G. Roumpos, M. Lohse, W. H. Nitsche, J. Keeling, M. H. Szymańska, P. B. Littlewood, A. Löffler, S. Höfling, L. Worschech, A. Forchel, Y. Yamamoto, *Proc. Natl. Acad. Sci. USA* **2012**, *109*, 6467.
- [21] D. Caputo, D. Ballarini, G. Dagvadorj, C. S. Muñoz, M. De Giorgi, L. Dominici, K. West, L. N. Pfeiffer, G. Gigli, F. P. Laussy, M. H. Szymańska, D. Sanvitto, *ArXiv:161005737 Cond-Mat* **2016**.
- [22] K. S. Daskalakis, S. A. Maier, S. Kéna-Cohen, *Phys. Rev. Lett.* **2015**, *115*, 35301.

## **Chapter 5. Control over energy transfer between fluorescent BODIPY dyes in a strongly coupled microcavity**

### **5.1. Motivation of work**

It has been shown that when two different semiconductors are placed in a microcavity they can hybridize via the confined photon modes, resulting in three different polariton branches. Energy transfer to the lower polariton branch (LPB) via hybridised polaritonic modes can occur in such hybrid systems, even when the molecular materials are physically separated by a “spacer layer”.

Polariton condensation occurs following bosonic stimulated scattering to the bottom of the LPB when the occupation of this state exceeds unity. Efficient population of the bottom of the LPB is a key ingredient in order to achieve a high occupancy. Therefore, studying efficient mechanisms by which the LPB can be populated may allow the reduction of polariton condensation threshold.

This work built upon work that showed that polariton states in the LPB in a range of molecular-barrier systems are populated from a reservoir of uncoupled excitons. Here we compare two microcavity structural designs. One type of cavity allowed short-range Förster resonance energy transfer (FRET) to take place between molecules. This was compared with a second type of cavity that was designed to allow only long-range polariton mediated energy transfer. We showed that FRET creates an energetically low-lying exciton reservoir with an efficiency close to unity. The FRET process was shown to be more efficient than long-range energy transfer, although it was only created over very small distances.

Here, it was concluded that in the multilayer microcavities, long-range polariton-mediated energy transfer was dependent on the detuning of the microcavity. Positively detuned microcavities showed an incomplete energy transfer to the LPB with the majority of luminescence emitted by the middle polariton branches (MPBs). This observation was explained using the Hopfield coefficients of MPB states along with the fact that the energetic distribution of the two exciton reservoirs favoured

population of middle branch polaritons rather than polaritons on the LPB. When negatively detuned microcavities were investigated, it was shown that a more efficient energy transfer occurred toward states on the LPB with a significant redistribution of emission from the microcavity.

In the case of microcavities where the two molecular dyes were blended together in a single layer, we showed that energy transfer occurred only in the exciton reservoir. In such structures, although MPB states are energetically accessible, luminescence is emitted only from the LPB suggesting a near-unity energy transfer.

## **5.2. Author contributions**

K.G. designed and fabricated the microcavity structures and then performed the optical spectroscopy experiments. P.M. supported the theory for polariton population density calculations (included in SI). L.G., M.C. and Z.S. synthesized and provided the BODIPY derivatives. K.G. wrote the manuscript with significant input from D.G.L. who also supervised the project.

## **5.3. Publication**

In the following, we present the publication, as it appears online in the Journal ACS Photonics.

“Reprinted with permission from Georgiou K. et al., Control over energy transfer between fluorescent BODIPY dyes in a strongly coupled microcavity, *ACS Photonics* 2018, 5, 1, 258-266. Copyright (2018) American Chemical Society.”

# Control over Energy Transfer between Fluorescent BODIPY Dyes in a Strongly Coupled Microcavity

Kyriacos Georgiou,<sup>†</sup> Paolo Michetti,<sup>‡</sup> Lizhi Gai,<sup>§</sup> Marco Cavazzini,<sup>||</sup> Zhen Shen,<sup>§</sup> and David G. Lidzey<sup>\*,†</sup>

<sup>†</sup>Department of Physics and Astronomy, The University of Sheffield, Sheffield S3 7RH, United Kingdom

<sup>‡</sup>Institute of Theoretical Physics, Technische Universität Dresden, 01062 Dresden, Germany

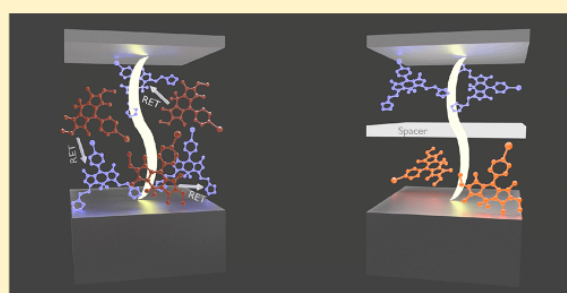
<sup>§</sup>State Key Laboratory of Coordination and Chemistry, School of Chemistry and Chemical Engineering, Nanjing University, Nanjing 210046, China

<sup>||</sup>Istituto di Scienze e Tecnologie Molecolari del Consiglio Nazionale delle Ricerche (ISTM-CNR), Via Golgi 19, I-20133 Milano, Italy

## Supporting Information

**ABSTRACT:** Hybridization of two fluorescent BODIPY dyes in a microcavity is achieved by coupling different exciton transitions to the same cavity mode. We characterize the luminescence of such a hybrid system following nonresonant laser excitation and show that the relative population along the different polariton branches can be controlled by changing cavity detuning. This effect is used to enhance exciton energy transfer to states along the lower polariton branch in negatively detuned cavities. We compare the efficiency of energy transfer via exciton hybridization with that achieved by dipole–dipole coupling.

**KEYWORDS:** polaritons, microcavities, hybridization, radiative pumping, fluorescent molecules



Since the first demonstration of strong coupling in organic microcavities in 1998<sup>1</sup> and room-temperature polariton emission shortly after,<sup>2</sup> organic exciton–polaritons have become a popular testbed for studying intriguing physics and macroscopic quantum phenomena at room temperature.<sup>3–8</sup> Organic polariton condensation and lasing have been reported in a handful of different systems such as conjugated polymers,<sup>3</sup> fluorescent proteins,<sup>4</sup> pure films of fluorescent molecules,<sup>5</sup> and crystalline organic semiconductors.<sup>6</sup> Very recently, a room-temperature organic exciton–polariton condensate was demonstrated in a cavity containing a fluorescent molecule dispersed in an inert polymer matrix.<sup>9</sup> Achieving condensation in such dilute molecular systems opens the possibility to create polariton lasers having wavelengths spanning the entire visible and near IR. However, it is not yet obvious which properties of organic materials lead to efficient polariton condensation and lasing. Efficient population of polaritons toward the bottom of the lower polariton branch (LPB) appears to be a key component in generating a macroscopic occupation and bosonic final state stimulation.<sup>10</sup> Understanding and controlling possible relaxation pathways are therefore an essential component in the design of efficient polariton lasing devices.

Hybridization of Frenkel excitons through strong coupling and polariton-mediated energy transfer between different excitons has been demonstrated in microcavities containing J-aggregated cyanine dyes.<sup>11–14</sup> Such molecular aggregates have relatively narrow absorption line widths (10's of meV),<sup>15,16</sup>

allowing different materials to be selected whose excitonic transitions are separated by an energy commensurate with the typical Rabi-splitting energy of a molecular material in a microcavity ( $\sim 100$  meV).<sup>1,2,17</sup> However, many J-aggregated molecular dyes have low fluorescence quantum efficiency<sup>18</sup> as a result of competing nonradiative pathways, a property that has so far precluded polaritons in J-aggregate microcavities undergoing condensation and lasing. It is of great interest therefore to explore polariton hybridization in microcavities based on diluted highly fluorescent molecules, as such materials have already been shown to undergo room-temperature polariton condensation.<sup>9</sup> We believe that by understanding and controlling energy transfer between hybridized molecular systems having high radiative rates, it may be possible to harness such effects to efficiently generate macroscopic polariton occupations in the “energy trap” at the bottom of the lower polariton branch and therefore reduce polariton lasing thresholds.

In this paper, we explore polariton hybridization and energy transfer in hybrid cavities containing a combination of two different, highly fluorescent molecular dyes doped in an optically inert polymer matrix. In cavities containing cyanine-

**Special Issue:** Strong Coupling of Molecules to Cavities

**Received:** September 3, 2017

**Published:** December 5, 2017

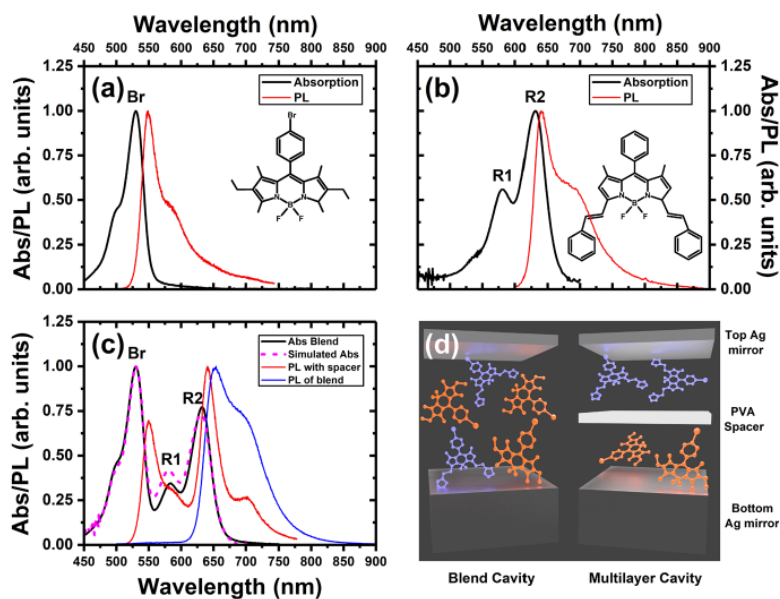


**Figure 1.** (a) Absorption and PL spectra of a BODIPY-Br control thin film along with its molecular structure. (b) Absorption and PL spectra of a BODIPY-R control thin film along with its molecular structure. (c) Absorption spectrum of the multilayer/blend film (black). PL emission from the multilayer (red) and blend (blue) thin film. Simulated absorption of the multilayer film (dotted). (d) Microcavity schematics for the two different configurations used (blend and multilayer).

dye J-aggregates, energy-transfer between polariton states can occur that is mediated by hybridized middle polariton branch (MPB) states.<sup>12</sup> Here, our objective is to explore whether such a process occurs in a cavity containing hybridized fluorescent molecular dyes and to compare the efficiency of such a process with the same structure in which direct energy transfer can occur between the dyes by dipole–dipole coupling (Förster transfer). In our experiments, we control direct and indirect interactions between uncoupled excitonic states by design of the cavity “active” layer. In one type of microcavity (hereafter termed a “multilayer cavity”), we place an optically inert thin spacer of the polymer polyvinyl alcohol (PVA) between two active layers that both contain a different type of strongly coupled molecular dye dispersed in a polystyrene (PS) matrix. Here, the thickness of the spacer layer was several tens of nanometers, corresponding to a value well in excess of the typical Förster transfer radii (typically less than 10 nm).<sup>19,20</sup> The spacer layer thus precludes any direct dipole–dipole coupling between molecules in the different active layers. In the second type of microcavity (termed a “blend cavity”), the two different molecular dyes are instead mixed together in a polystyrene matrix, with the average spatial separation between molecules being <3 nm, permitting direct dipole–dipole coupling and thus nonradiative energy transfer.<sup>21</sup> Our experiments allow us to compare the efficiency of energy transfer in the strong-coupling regime against that of short-range Förster transfer. We show that energy transfer to states along the lower polariton branch is significantly enhanced in a negatively detuned cavity; however this process is not as efficient as dipole–dipole coupling in which energy transfer occurs with an efficiency of almost unity.

The molecular materials used in our experiments are based on a boron-dipyrromethene core (BODIPY) that has been functionalized in such a way to modify its exciton energy (see Methods). The chemical structures as well as the optical

absorption and fluorescence spectra of the two BODIPY derivatives (termed BODIPY-Br and BODIPY-R) as measured from control thin films are shown in Figure 1(a) and (b), respectively. Here spectra were recorded when the dyes were dispersed in a PS matrix at a concentration of 20% and 10%, respectively (by mass). BODIPY-Br has a (0, 0) electronic transition at 530 nm that can strongly couple, which we refer to, for the sake of simplicity, as “Br”. The molecular dye BODIPY-R has two dipole-allowed transitions at 581 and 630 nm (corresponding to (0, 1) vibronic and (0, 0) electronic transitions) that we show can both undergo strong coupling, which we refer to as “R1” and “R2”, respectively.

BODIPY-Br and BODIPY-R were deposited into microcavity structures consisting of two silver mirrors (a 200 nm thick bottom mirror and a 35 nm thick semitransparent top mirror deposited by thermal evaporation) with the whole structure fabricated on a quartz-coated glass substrate. To fabricate “multilayer” cavities (see schematic in Figure 1(d)), a layer of PVA (spin-cast from a water solution) was used to separate the two BODIPY-containing PS films that were both spin-cast from toluene. The orthogonal nature of the solutions used to deposit the various layers permitted well-defined and stable multilayers to be constructed. “Blend” cavities instead contained a mixture of BODIPY-Br and BODIPY-R that were both dispersed in a PS matrix and deposited in a single layer. The optical properties of a (control) blend layer of BODIPY-Br and BODIPY-R and a multilayer of the same materials are shown in Figure 1(c).

We first consider the optical properties of the blend film. Here, we find that its measured absorption spectrum can be described by an approximate superposition of the absorption spectra of its BODIPY-Br and BODIPY-R components. This is shown in Figure 1(c), where we simulate the blend absorption based on a linear superposition of absorption spectra (19% BODIPY-Br and 11% BODIPY-R), a composition that is very similar to that added to the solution used to spin-cast this layer

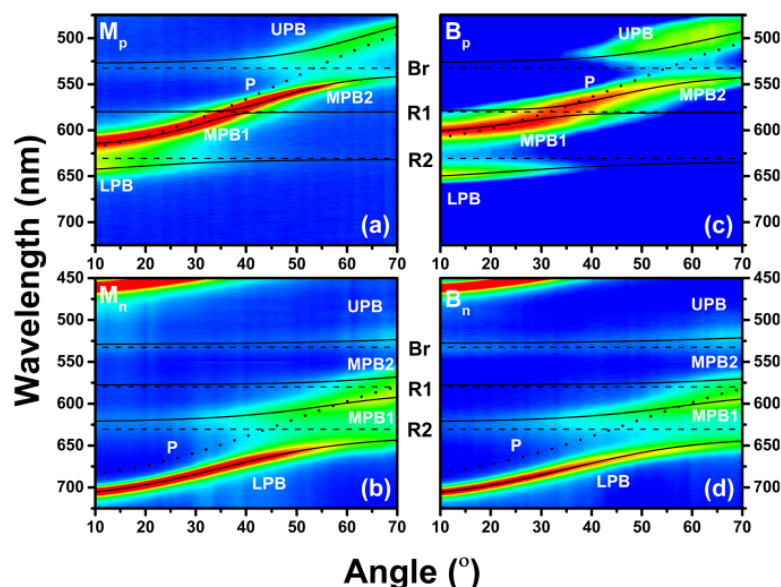


**Figure 2.** Angular white-light reflectivity data from cavities (a)  $M_p$ , (b)  $M_n$ , (c)  $B_p$ , and (d)  $B_n$ . The black solid lines represent the LPB, MPB1, MPB2, and UPB calculated using the four-level coupled oscillator model. The dashed and dotted lines show the energy of excitons Br, R1, and R2 and the cavity mode P of each cavity.

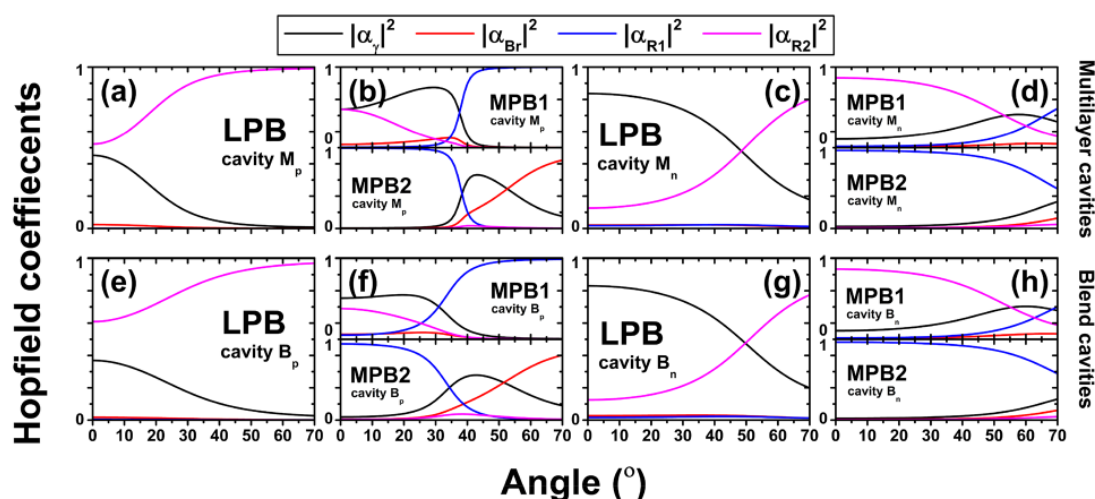


**Figure 3.** Hopfield coefficients of the LPB, MPB1, and MPB2 calculated using the four-level coupled oscillator model for multilayer cavities (a, b)  $M_p$  and (c, d)  $M_n$  and blend cavities (e, f)  $B_p$  and (g, h)  $B_n$ .

(20% BODIPY-Br and 10% BODIPY-R). This indicates that there is no direct ground-state interaction between the different molecular materials. However, excited-state energy transfer between the BODIPY-Br and BODIPY-R components is highly efficient (see spectra plotted using a blue line); on excitation of the film at 473 nm, we find that 99% of PL emission comes from BODIPY-R, with this emission being slightly red-shifted in wavelength due to an inner-filter effect. We attribute the suppression of the BODIPY-Br PL from the blend film as resulting from dipole–dipole coupling between the two different molecular dyes, with BODIPY-Br acting as a donor and BODIPY-R as an acceptor.

The optical absorption of the multilayer can also be approximated by a superposition of the absorption spectra of its BODIPY-Br and BODIPY-R components. The PL emission from the multilayer is however qualitatively different from that of the blend film, with a similar intensity of emission from both BODIPY-Br and BODIPY-R observed (see spectra plotted using a red line in Figure 1(c)). We can in fact describe the emission spectrum of the multilayer using a weighted linear superposition of the emission spectra of its individual components. Here, by integrating the area under the fitted single components of the bilayer, we find that an equal fraction of emission originates from BODIPY-Br and BODIPY-R. In both the multilayer and blend configurations, we find that the

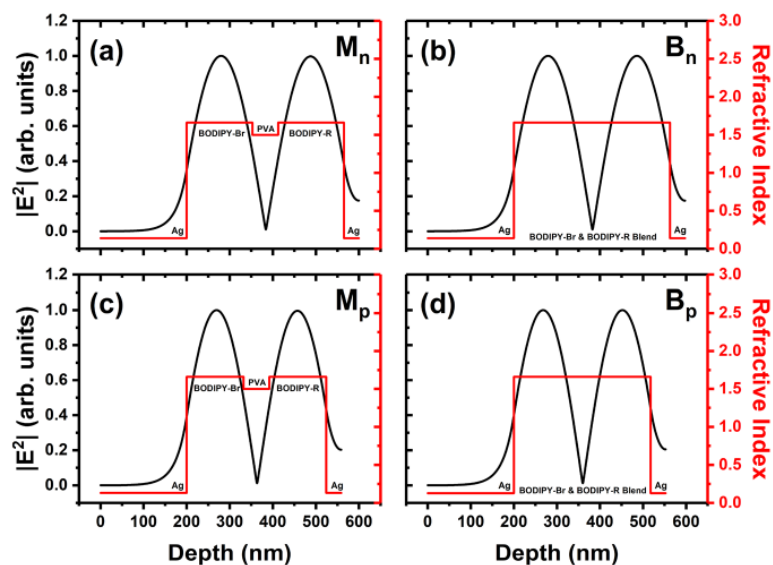


**Figure 4.** Electric field  $|E^2|$  distribution and refractive index along the structure depth for the multilayer cavities (a)  $M_n$  and (c)  $M_p$  and the blend cavities (b)  $B_n$  and (d)  $B_p$ .

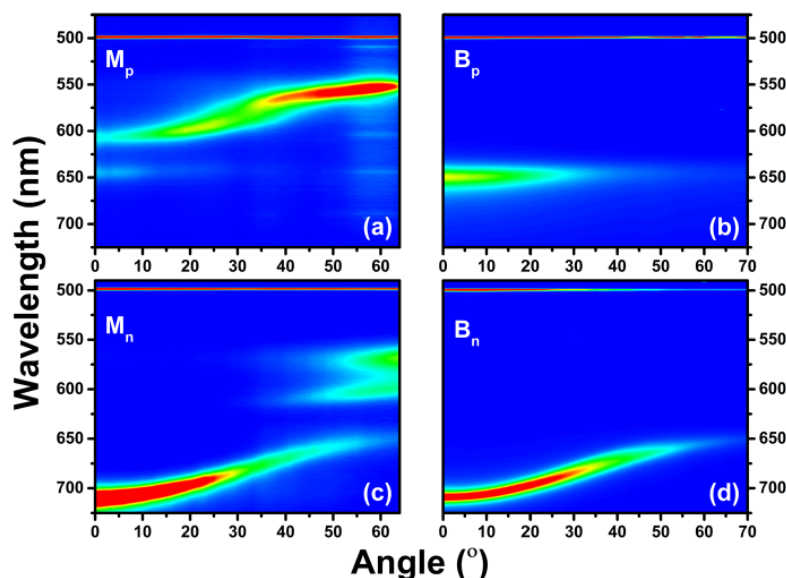


**Figure 5.** PL emission following nonresonant excitation at 500 nm. (a) Cavity  $M_p$ , (b) cavity  $B_p$ , (c) cavity  $M_n$ , and (d) cavity  $B_n$ .

PL emission spectrum is not apparently dependent on the side from which the multilayer film is initially excited.

We now consider the optical properties of blend and multilayer films when placed into a microcavity. Here, for each type of cavity, we have fabricated positively ( $\Delta = +28$  meV) and negatively ( $\Delta = -162$  meV) detuned cavities. Here, we define detuning by the energy difference between BODIPY-R exciton energy ( $E_R$ ) and photon energy ( $E_p$ ) at normal incidence where  $\Delta = E_p - E_R$ . This was done by adjusting the total film thickness to be 330 and 390 nm for the positively and negatively detuned cavities, respectively. To confirm optical strong coupling, we recorded the angular-dependent white-light optical reflectivity of the different cavities. The reflectivity

spectra of four cavities are plotted in Figure 2(a) to (d). Here parts (a) and (b) correspond to measurements made on positively and negatively detuned multilayer cavities (labeled as  $M_p$  and  $M_n$ , respectively). Parts (c) and (d) similarly correspond to measurements made on positively and negatively detuned blend cavities (labeled as  $B_p$  and  $B_n$ , respectively). In all cases, strong coupling is evidenced by anticrossing of the polariton branches at the angles where the photon mode and excitons would have been degenerate. As our cavities couple together four oscillators, Br, R1, R2, and the cavity mode, we expect the cavity dispersion to be characterized by four polariton branches.

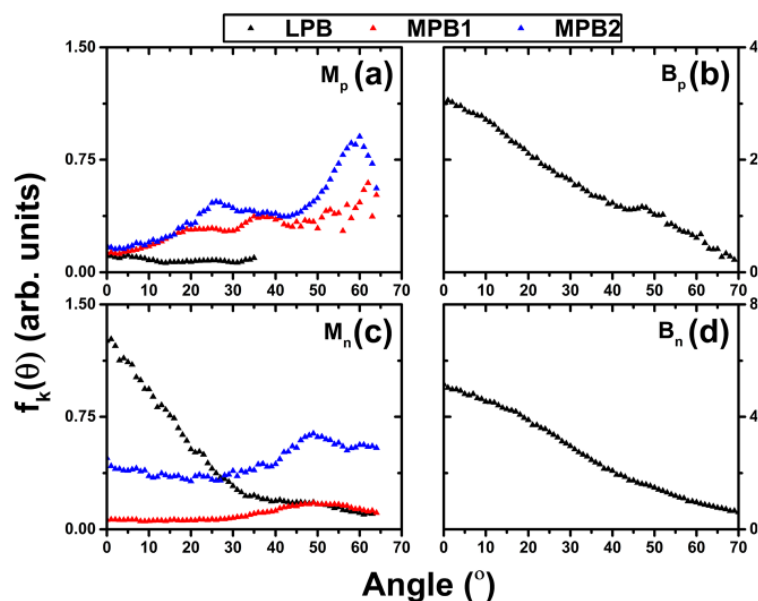


**Figure 6.** (a) Relative polariton population density  $f_k(\theta)$  of LPB, MPB1, and MPB2 from cavity  $M_p$ . (b)  $f_k(\theta)$  of LPB from cavity  $B_p$ . (c)  $f_k(\theta)$  of LPB, MPB1, and MPB2 from cavity  $M_n$ . (d)  $f_k(\theta)$  of LPB from cavity  $B_n$ .

To model the cavities, we use a four-level coupled oscillator model (see Supporting Information), which on diagonalization of the Hamiltonian results in four unique solutions. These are fit to the polariton branches as shown in the reflectivity spectra of the cavities in Figure 2(a) to (d). We tabulate the energy of the LPB at  $k_{\parallel} = 0$  and the coupling constants used in the fits in Supporting Information Table S1. We also identify the upper and lower polariton branches (UPB and LPB), as well as two middle branches (MPB1 and MPB2) in Figure 2 and also plot the energy of the uncoupled photon (P) and Br, R1, and R2 transitions. From the four-level coupled oscillator model, we determine the different Hopfield coefficients that quantify the exciton and photon mixing in each of the polariton branches. This is plotted for the middle and lower polariton branches for  $M_p$ ,  $M_n$ ,  $B_p$ , and  $B_n$  cavities as shown in Figure 3. For simplicity, we omit the upper polariton branch from our discussions, as the polariton population in such states is in most cases relatively low.

Note that the multilayer and the blend configuration cavities were designed to have identical optical properties. While this was largely achieved (as indicated by the very similar cavity-mode dispersion curves), we find it was necessary to use slightly different values of background refractive index and coupling strength between excitons and photons in our modeling. There are two reasons for this; first the PVA layer has a lower refractive index (1.50) compared to that of PS (1.59). As PVA was not used in the blend cavities, the effective refractive index used was slightly higher. Second, the blended cavities required a thicker active layer in order to compensate for the thickness and photon–exciton detuning, in the absence of the PVA spacer layer, which then resulted in a slight increase of the coupling strength between the excitons and the cavity mode. As can be seen in Figure 3, the Hopfield mixing fractions are very similar in the different cavity pairs ( $M_p$ ,  $B_p$ ) and ( $M_n$ ,  $B_n$ ).

We have also used a transfer matrix model to calculate the distribution of the electric field ( $|E^2|$ ) in the structures studied.

Figure 4(a) to (d) show calculated values of  $|E^2|$  together with the refractive index of the different layers in a direction parallel to the cavity axis. In each cavity, we identify the location of the various layers (either dye-doped polystyrene layer or a PVA spacer layer). In the multilayer cavities (parts (a) and (c)), it can be seen that there are field antinodes in the middle of each of the active layers and a node in the center of the PVA spacer. This field distribution results in efficient coupling between the excitons and the cavity mode. In the blend cavities (parts (b) and (d)), the active materials are distributed through a single layer, with the distribution of the field being qualitatively very similar.

We have explored angular PL emission from the cavities following nonresonant excitation at 500 nm (see Figure 5(a) to (d)). Here, excitation was performed close to normal incidence, with luminescence collected using a lens mounted on one arm of a goniometer and then delivered to a CCD spectrometer via a fiber-optic bundle. We estimate that the lens collected luminescence over a solid angle of 0.05 sr and a range of angles between  $0^\circ$  and  $70^\circ$ . It can be seen that in the multilayer cavities, PL is mainly emitted by the MPB1 and MPB2 in the positively detuned cavity (see Figure 5(a)) and by the LPB in the negatively detuned cavity (see Figure 5(c)). In contrast, PL emission from the blend cavities comes only from the LPB in both positively and negatively detuned cavities (see Figure 5(b) and (d)). We note that the emission distribution from the negatively detuned multilayer cavity is qualitatively similar to that observed previously in strongly coupled microcavities containing two hybridized J-aggregated cyanine dyes.<sup>12</sup>

To analyze data shown in Figure 5 in a quantitative manner and convert intensity of luminescence into a relative polariton population, we need to correct for both the photon fraction of each emissive state and also the relative angle subtended by our angular measurement process. We discuss this correction in the Supporting Information. In brief, we convert the intensity of luminescence from each of the branches measured at any angle

$I(\theta)$ ) to a relative polariton population density ( $f_k(\theta)$ ) using  $f_k(\theta) = I(\theta)/[|\alpha_r(\theta)|^2 \cos(\theta)|E_r(\theta)|^2]$ , where  $E_r(\theta)$  is the energy of the polaritons and  $|\alpha_r(\theta)|^2$  is the photon fraction of the branch. We then integrate  $f_k(\theta)$  over all angles, to determine the total polariton population along each of the polariton branches. Figure 6(a) to (d) plots  $f_k(\theta)$  for the middle and lower polariton branches for cavities  $M_p$  and  $M_n$  (parts (a) and (c)) and the lower branch in cavities  $B_p$  and  $B_n$  (parts (b) and (d)), respectively. Note that the middle branch polariton population in cavities  $B_p$  and  $B_n$  is not plotted, as it is negligible. We discuss the relative population of states along these different branches in the following paragraphs.

We have previously shown that the LPB in BODIPY-Br cavities can be effectively populated following radiative decay of weak-coupled excitons in an exciton reservoir (positioned at lower energy) that populates (pumps) the photonic component of the polariton. This process is maximized for photon-like polariton states. Note, however, our previous measurements have shown the distribution of weak-coupled exciton reservoir states is not simply defined by the total distribution of emissive excitonic states.<sup>22</sup> Rather in BODIPY-Br cavities, it appears that emission from a combination of weak-coupled excimer states, together with vibronic emission from (0, 1) excitons, is most effective in pumping LPB polariton states. Here, we use such a concept to understand the emission from hybrid polariton cavities.

We first consider the positively detuned multilayer cavity ( $M_p$ ). Here, nonresonant excitation of the cavity only seems effective in populating MPB states. This observation can be partly explained using the Hopfield coefficients for MPB1,2 as determined using the coupled oscillator model, as can be seen in Figure 3(a) and (b). Here, we find that the MPB1 and MPB2 are highly photon-like over a range of angles, with MPB2 consisting of a relatively large fraction of Br at large angles. As the efficiency of the photon-pumping mechanism is proportional to the photon fraction of the polariton branch, we expect MPB1 and MPB2 polaritons to be efficiently pumped by the weakly coupled excitons in the Br reservoir. Our previous measurements on BODIPY-Br cavities have shown that this reservoir is most effective in optically pumping polariton states over the wavelength range 570 to 600 nm.<sup>22</sup> The coincidence between the spectral position of the two middle branches in cavity  $M_p$  (542 to 615 nm) and the Br exciton reservoir qualitatively suggests that weak-coupled Br states should be able to optically pump hybrid middle-branch polariton states. Figure 6(a) confirms the effective population of MPB states by the substantial polariton population that is determined along these branches (particularly at high angle corresponding to energies close to the Br exciton reservoir).

The polariton population on the LPB of cavity  $M_p$  is in contrast much lower (again see Figure 6(a)). There are a number of effects that we believe contribute to this result. First, the highly radiative nature of the middle branches in this cavity means that polaritons on MPB1,2 are more likely to decay via photon emission, rather than undergo relaxation to the BODIPY-R reservoir. Second, the positive detuned nature of this cavity means that the bottom of the LPB is positioned close in energy to the BODIPY-R (0, 0) exciton (within 50 meV). We have previously shown in a strong-coupled BODIPY-Br cavity that the LPB is actively populated 250 meV below the (0, 0) exciton resonance by a radiative scattering process, which we associated with vibronic-assisted (0, 1) radiative emission or/and with the presence of low-lying weakly coupled exciton

states (i.e., 250 meV below the (0, 0) resonance).<sup>22</sup> If we assume a similar behavior for the BODIPY-R system, then we would expect a radiative pumping mechanism active at about 720 nm, which is however far below the bottom of the LPB of the  $M_p$  microcavity. Previous theoretical and experimental work has shown that such vibronic emission is able to efficiently pump polaritons on the LPB.<sup>22–24</sup> However, as the bottom of the LPB in the  $M_p$  cavity is located at 644 nm, we speculate that there is not a sufficient reservoir population available at this wavelength to populate LPB polaritons. Note that the LPB in this cavity is also predominantly exciton-like (see Figure 3(a)), with its photon fraction that rapidly decreases at higher angles also suppressing possible radiative scattering processes.

We now discuss the negatively detuned multilayer cavity  $M_n$  (see Figure 3(c)). Here, we find that the LPB is highly photon-like particularly at small angles (84% at normal incidence) and emits luminescence efficiently as shown in Figure 5(c). Figure 6(c) confirms that the polariton population in the LPB is also greater than that of MPB1,2 (between angles of 0° and 26°). The LPB is now in the correct energy range for the radiative scattering mechanism from the BODIPY-R reservoir to take place; indeed, the bottom of the LPB is located around 710 nm, providing a very effective route to populate polaritons on the LPB.

In contrast to  $M_p$ , the emission from MPB1 in cavity  $M_n$  is suppressed (see Figure 5(c)). Here we expect the two middle branches to be efficiently pumped from the BODIPY-Br reservoir, with the general increase in population on MPB1,2 at angles >40° consistent with a greater overlap with reservoir states. However, MPB1 and MPB2 are likely to be significantly less radiant than the LPB, as they contain a lower photon fraction; see Figure 3(d). We suspect that polaritons on MPB1 are likely to scatter down in energy and populate the lower lying BODIPY-R reservoir, as they contain a high R2 fraction. Such polaritons are then available to populate states along the LPB, a result confirmed by the distribution of polaritons along the different branches shown in Figure 6(c). Our measurements therefore suggest that negatively detuned hybrid cavities are relatively more efficient in promoting energy transfer between the coupled states than comparable positively detuned structures.

We now turn our attention to the blend cavities  $B_p$  and  $B_n$ . In the noncavity film of the blend, nonradiative energy transfer suppresses emission from the BODIPY-Br donor exciton, and the BODIPY-R acceptor exciton is the only source of luminescence. As it has been discussed earlier for the multilayer cavities, radiative pumping appears to be the main mechanism by which polaritonic states are populated. We therefore expect that energy transfer into the low-lying BODIPY-R reservoir will suppress population of middle branch polaritons. This is indeed confirmed in Figure 5(b) and (d), which show the emission from cavities  $B_p$  and  $B_n$  is dominated by LPB luminescence. Indeed in these cavities, the polariton population is distributed toward the bottom of the LPB (see Figure 6(b) and (d)). The absence of luminescence from the middle branches confirms the fact that despite such states being energetically accessible, relaxation within the exciton reservoirs occurs more rapidly than excitons can populate states on MPB1 and MPB2. This result is consistent with previous studies on microcavities in which a cavity photon was strongly coupled to the Soret band of a porphyrin dye.<sup>1</sup> Here, it was found that the polariton states were nonluminescent due to rapid relaxation of excitons to the lower lying q-band.

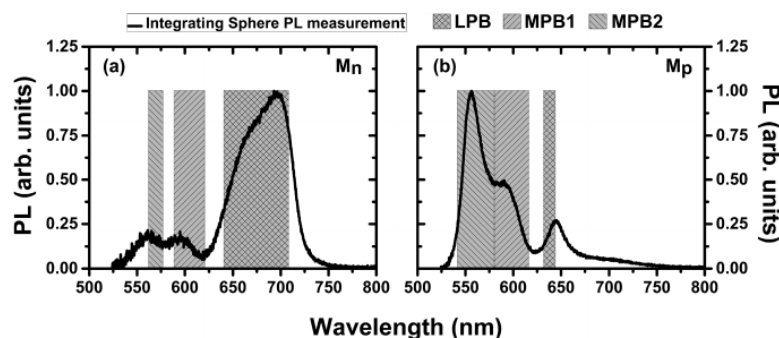


**Figure 7.** PL emission following nonresonant excitation at 405 nm using an integrating sphere. (a) Cavity  $M_n$  and (b) cavity  $M_p$ . The shaded area corresponds to the wavelength range of the LPB, MPB1, and MPB2.

We can use our measurements of the angular-dependent emission to explore the relative efficiency of the energy transfer process that is generated by exciton hybridization. Returning to Figure 6(a) and (c), we find that in cavity  $M_n$  44% of total polariton states are found on the LPB, with 12% and 44% of states located on MPB1 and -2, respectively. Notably, however, both MPB1 and -2 contain a high BODIPY-R exciton fraction (see Figure 3(d)). If we now arbitrarily include polariton states along the middle branches whose excitonic component is predominantly derived from BODIPY-R (i.e., having >90% of their excitonic fraction being BODIPY-R), we find that around 85% of all polariton states in the cavity are in fact associated with BODIPY-R, indicating a substantial degree of population transfer. This is in direct contrast to cavity  $M_p$ , in which only 6% of polaritons are located on the LPB, with 53% and 41% of polaritons located on MPB1 and -2, respectively. Here, while states along MPB1 contain a high fraction of BODIPY-R, polariton branch MPB2 contains a majority fraction (at angles greater than  $40^\circ$ ) of BODIPY-Br. This indicates that in cavity  $M_p$  energy transfer is relatively suppressed.

Figure 6(b) and (d) indicate that in cavities  $B_n$  and  $B_p$  all states are located on the LPB (which in both cavities contains a negligible fraction of BODIPY-Br). This indicates that Förster transfer is more efficient than energy transfer mediated by exciton hybridization. However, it is clear that polariton hybridization is able to transfer energy between excitonic states that are separated by much larger distances than could be achieved by direct dipole–dipole coupling (here the PVA spacer layer has a thickness of 60 nm). Our measurements also demonstrate that the level of energy transfer between polariton states is critically dependent on cavity design, with the relative population of lower branch polaritons being around 6 times higher in cavity  $M_n$  compared to cavity  $M_p$ .

We can also evidence a significant redistribution in emission generated by hybridization of excitons in the strong coupling regime by comparing the integrated angular cavity emission with that of a control film. To explore this effect, we have placed cavities  $M_n$  and  $M_p$  inside an integrating sphere and have measured their emission following nonresonant excitation at 405 nm as shown in Figure 7(a) and (b), respectively. For comparison, we indicate the spectral regions that correspond to the various polariton branches using shaded blocks. Here, the difference in luminescence emission from the different cavities is apparent, with cavity  $M_n$  dominated by an emission band around 650 to 700 nm. Cavity  $M_p$  in contrast is characterized by emission that peaks at 556 nm. Comparing this with the PL

emission from the control multilayer film shown in Figure 1(c), it can be seen that both types of cavity result in a dramatic change in emission pattern.

We analyze the PL emission spectra by fitting it to a series of Lorentzian curves. These curves are then integrated over wavelength to determine the percentage of emission corresponding to each polariton branch. Our calculation suggests that in the positively detuned multilayer cavity  $M_p$ , 12% of the light emitted by the cavity comes from the LPB, with the remainder emitted from MPB1 and -2. In the negatively detuned cavity  $M_n$ , the LPB is highly emissive and comprises 87% of cavity emission. This result again confirms that there is redistribution of luminescence toward states associated with BODIPY-R in negatively detuned cavities, while in the positively detuned cavities, emission mainly occurs at wavelengths corresponding to the emission from both MPB1 and -2 (which also closely coincides with the emission peak of BODIPY-Br).

In conclusion, we have studied strong coupling and hybridization between the excitonic transition of two organic dyes in two different cavity configurations, one that incorporated an inert spacer layer to separate the two dye layers and the other containing the same dye molecules that had been blended together in a host matrix. We show that in cavities containing the spacer layer the emission pattern from the cavity is strongly dependent on the relative detuning of the cavity, with energy transfer to the lower polariton branch being significantly more efficient in a negatively detuned cavity compared to a positively detuned cavity. On placing the cavities into an integrating sphere, we determine that the negatively detuned cavity results in a strong redistribution of emission toward states associated with the lowest energy excitonic state. We find however that energy transfer via strong coupling is not as an efficient process as direct dipole–dipole coupling; here energy transfer between the molecules occurs within the exciton reservoir, with all emission occurring from the lower polariton branch. It will of course be interesting to explore the nonlinear emission from such cavities to determine the extent to which hybridization can modify the process of polariton condensation.

## METHODS

**Sample Fabrication.** BODIPY-Br and BODIPY-R were synthesized following procedures reported in the literature.<sup>25,26</sup> The BODIPY-core materials Br and R were dispersed in a polystyrene (MW  $\approx$  192,000)-containing toluene solution at 35

mg/mL, with the two BODIPY dyes (Br and R) having a relative mass fraction of 20% and 10%, respectively. The PVA was dissolved in DI water at a concentration of 35 mg/mL. The BODIPY-containing layers were spin-coated using 100  $\mu$ L of solution, with 150  $\mu$ L of solution used to deposit the PVA spacer layer. The thickness of each layer was controlled via the spin speed of the spin-coater. The thickness of each layer was measured on a Bruker DektakXT profilometer. The cavity silver mirrors were thermally evaporated using an Auto 306 Edwards thermal evaporator. Typical cavities had a Q-factor of 70.

**Angular White-Light Reflectivity Measurements.** A halogen-deuterium white-light source was used to illuminate the microcavities through the 35 nm semitransparent silver mirror. The incident and reflected light was collimated and focused onto the sample and the detector, respectively, using lenses mounted on two moving arms. The two arms were connected to two concentric motorized wheels, allowing us to change the angle of incidence between the white-light source and the sample as well as the collection path. The reflected light was coupled into an optical fiber and imaged into an Andor Shamrock CCD spectrometer.

**Angular PL and Integrating Sphere Measurements.** Angular-dependent PL measurements were performed using the same collection path as described above. A fiber-coupled Fianium supercontinuum laser filtered at 500 nm by a SPEX 270 M monochromator was used for nonresonant excitation of the microcavities through the semitransparent mirror. A laser beam was focused onto the samples with a slight downward tilt to avoid direct reflection of the excitation beam into the CCD camera. Integrating sphere measurements were performed using a 405 nm CW laser diode to excite the microcavities. The cavity was placed inside the sphere, with a series of baffles placed inside the sphere to homogenize the optical field within the sphere. An optical fiber was used to collect the total PL from the integrating sphere exit port and direct it to a CCD spectrometer. Black tape was placed around the edges of the cavity substrate to ensure that the luminescence detected was emitted through the front surface of the cavity, rather than emitted from the edge of the substrate.

## ■ ASSOCIATED CONTENT

### Supporting Information

The Supporting Information is available free of charge on the ACS Publications website at DOI: 10.1021/acsphtonic.7b01002.

Four-level coupled oscillator model used and table of the values extracted from the model; polariton PL conversion to polariton population density (PDF)

## ■ AUTHOR INFORMATION

### Corresponding Author

\*E-mail: d.g.lidzey@sheffield.ac.uk

### ORCID

Kyriacos Georgiou: 0000-0001-5744-7127

David G. Lidzey: 0000-0002-8558-1160

### Notes

The authors declare no competing financial interest.

## ■ ACKNOWLEDGMENTS

We thank the UK EPSRC for funding this research through the research grant EP/M025330/1 "Hybrid Polaritonics" and for funding a Ph.D. scholarship for K.G.

## ■ REFERENCES

- (1) Lidzey, D. G.; Bradley, D. D. C.; Skolnick, M. S.; Virgili, T.; Walker, S.; Whittaker, D. M. Strong Exciton-Photon Coupling in an Organic Semiconductor Microcavity. *Nature* **1998**, *395*, 53.
- (2) Lidzey, D. G.; Bradley, D. D. C.; Virgili, T.; Armitage, a.; Skolnick, M. S.; Walker, S. Room Temperature Polariton Emission from Strongly Coupled Organic Semiconductor Microcavities. *Phys. Rev. Lett.* **1999**, *82*, 3316.
- (3) Plumhof, J. D.; Stoefler, T.; Mai, L.; Scherf, U.; Mahrt, R. F. Room-Temperature Bose-Einstein Condensation of Cavity Exciton-Polariton in a Polymer. *Nat. Mater.* **2014**, *13*, 328.
- (4) Dietrich, C. P.; Steude, A.; Tropsch, L.; Schubert, M.; Kronenberg, N. M.; Ostermann, K.; Höfling, S.; Gather, M. C. An Exciton-Polariton Laser Based on Biologically Produced Fluorescent Protein. *Sci. Adv.* **2016**, *2*, e1600666.
- (5) Daskalakis, K. S.; Maier, S. a.; Murray, R.; Kéna-cohen, S. Nonlinear Interactions in an Organic Polariton Condensate. *Nat. Mater.* **2014**, *13*, 271.
- (6) Kéna-cohen, S.; Forrest, S. R. Room-Temperature Polariton Lasing in an Organic Single-Crystal Microcavity. *Nat. Photonics* **2010**, *4*, 371.
- (7) Daskalakis, K. S.; Maier, S. A.; Kéna-Cohen, S. Spatial Coherence and Stability in a Disordered Organic Polariton Condensate. *Phys. Rev. Lett.* **2015**, *115*, 35301.
- (8) Lerario, G.; Fieramosca, A.; Barachati, F.; Ballarini, D.; Daskalakis, K. S.; Dominici, L.; De Giorgi, M.; Maier, S. A.; Gigli, G.; Kéna-Cohen, S.; Sanvitto, D. Room-Temperature Superfluidity in a Polariton Condensate. *Nat. Phys.* **2017**, *13*, 837.
- (9) Cookson, T.; Georgiou, K.; Zasedatelev, A.; Grant, R. T.; Virgili, T.; Cavazzini, M.; Galeotti, F.; Clark, C.; Berloff, N. G.; Lidzey, D. G.; Lagoudakis, P. G. A Yellow Polariton Condensate in a Dye Filled Microcavity. *Adv. Opt. Mater.* **2017**, *5*, 1700203.
- (10) Imamoglu, A.; Ram, R.; Pau, S.; Yamamoto, Y. Nonequilibrium Condensates and Lasers without Inversion: Exciton-Polariton Lasers. *Phys. Rev. A: At, Mol, Opt. Phys.* **1996**, *53*, 4250.
- (11) Lidzey, D. G.; Bradley, D. D. C.; Armitage, A.; Walker, S.; Skolnick, M. S. Photon-Mediated Hybridization of Frenkel Excitons in Organic Semiconductor Microcavities. *Science* **2000**, *288*, 1620.
- (12) Coles, D. M.; Somaschi, N.; Michetti, P.; Clark, C.; Lagoudakis, P. G.; Savvidis, P. G.; Lidzey, D. G. Polariton-Mediated Energy Transfer between Organic Dyes in a Strongly Coupled Optical Microcavity. *Nat. Mater.* **2014**, *13*, 712.
- (13) Zhong, X.; Chervy, T.; Wang, S.; George, J.; Thomas, A.; Hutchison, J. A.; Devaux, E.; Genet, C.; Ebbesen, T. W. Non-Radiative Energy Transfer Mediated by Hybrid Light-Matter States. *Angew. Chem., Int. Ed.* **2016**, *55*, 6202.
- (14) Zhong, X.; Chervy, T.; Zhang, L.; Thomas, A.; George, J.; Genet, C.; Hutchison, J.; Ebbesen, T. W. Energy Transfer between Spatially Separated Entangled Molecules. *Angew. Chem., Int. Ed.* **2017**, *56*, 9034.
- (15) Jelley, E. E. Spectral Absorption and Fluorescence of Dyes in the Molecular State. *Nature* **1936**, *138*, 1009.
- (16) Scheibe, G. Der Chemie-Ingenieur. Ein Handbuch Der Physikalischen Arbeitsmethoden in Chemischen Und Verwandten Industrie- Betrieben. *Angew. Chem.* **1936**, *49*, 563.
- (17) Hobson, P. A.; Barnes, W. L.; Lidzey, D. G.; Gehring, G. A.; Whittaker, D. M.; Skolnick, M. S.; Walker, S. Strong Exciton-Photon Coupling in a Low-Q All-Metal Mirror Microcavity. *Appl. Phys. Lett.* **2002**, *81*, 3519.
- (18) Sundström, V.; Gillbro, T.; Gadonas, R. A.; Piskarskas, A. Annihilation of Singlet Excitons in J Aggregates of Pseudoisocyanine (PIC) Studied by Pico- and Subpicosecond Spectroscopy. *J. Chem. Phys.* **1988**, *89*, 2754.

- (19) Virgili, T.; Lidzey, D. G.; Bradley, D. D. C. Efficient Energy Transfer from Blue to Red in Tetraphenylporphyrin-Doped poly(9,9-Dioctylfluorene) Light-Emitting Diodes. *Adv. Mater.* **2000**, *12*, 58.
- (20) Cerullo, G.; Stagira, S.; Zavelani-Rossi, M.; De Silvestri, S.; Virgili, T.; Lidzey, D. G.; Bradley, D. D. C. Ultrafast Förster Transfer Dynamics in Tetraphenylporphyrin Doped poly(9,9-Dioctylfluorene). *Chem. Phys. Lett.* **2001**, *335*, 27.
- (21) Scholes, G. D. Long-Range Resonance Energy Transfer in Molecular Systems. *Annu. Rev. Phys. Chem.* **2003**, *54*, 57.
- (22) Grant, R. T.; Michetti, P.; Musser, A. J.; Gregoire, P.; Virgili, T.; Vella, E.; Cavazzini, M.; Georgiou, K.; Galeotti, F.; Clark, C.; Clark, J.; Silva, C.; Lidzey, D. G. Efficient Radiative Pumping of Polaritons in a Strongly Coupled Microcavity by a Fluorescent Molecular Dye. *Adv. Opt. Mater.* **2016**, *4*, 1615.
- (23) Fontanesi, L.; Mazza, L.; La Rocca, G. C. Organic-Based Microcavities with Vibronic Progressions: Linear Spectroscopy. *Phys. Rev. B: Condens. Matter Mater. Phys.* **2009**, *80*, 235314.
- (24) Mazza, L.; Kéna-Cohen, S.; Michetti, P.; La Rocca, G. C. Microscopic Theory of Polariton Lasing via Vibronically Assisted Scattering. *Phys. Rev. B: Condens. Matter Mater. Phys.* **2013**, *88*, 75321.
- (25) Gupta, N.; Reja, S. I.; Bhalla, V.; Gupta, M.; Kaur, G.; Kumar, M. A Bodipy Based Dual Functional Probe for the Detection of Hydrogen Sulfide and H<sub>2</sub>S Induced Apoptosis in Cellular Systems. *Chem. Commun.* **2015**, *51*, 10875.
- (26) Wang, Z.; Xie, Y.; Xu, K.; Zhao, J.; Glusac, K. D. Diodobodipy-Styrylbodipy Dyads: Preparation and Study of the Intersystem Crossing and Fluorescence Resonance Energy Transfer. *J. Phys. Chem. A* **2015**, *119*, 6791.

## 5.4. Supporting Information

# Control over Energy Transfer between Fluorescent BODIPY Dyes in a Strongly Coupled Microcavity

Kyriacos Georgiou,<sup>1</sup> Paolo Michetti,<sup>2</sup> Lizhi Gai,<sup>3</sup> Marco Cavazzini,<sup>4</sup> Zhen Shen,<sup>3</sup>  
and David G. Lidzey\*,<sup>1</sup>

<sup>1</sup>Department of Physics and Astronomy, The University of Sheffield, Sheffield S3 7RH, United Kingdom

<sup>2</sup>Institute of Theoretical Physics, Technische Universität Dresden, 01062 Dresden, Germany

<sup>3</sup>State Key Laboratory of Coordination and Chemistry, School of Chemistry and Chemical Engineering, Nanjing University, Nanjing 210046, China

<sup>4</sup>Istituto di Scienze e Tecnologie Molecolari del Consiglio Nazionale delle Ricerche (ISTM-CNR), Via Golgi 19, I-20133 Milano, Italy

Number of pages: 3

Number of Tables: 1

## Four level coupled oscillator model

The four level coupled oscillator model used to describe strong coupling in the hybrid microcavities.

$$\begin{pmatrix} E_\gamma(\theta) & \hbar\Omega_1/2 & \hbar\Omega_2/2 & \hbar\Omega_3/2 \\ \hbar\Omega_1/2 & E_{Br} & 0 & 0 \\ \hbar\Omega_2/2 & 0 & E_{R1} & 0 \\ \hbar\Omega_3/2 & 0 & 0 & E_{R2} \end{pmatrix} \begin{pmatrix} \alpha_\gamma \\ \alpha_{Br} \\ \alpha_{R1} \\ \alpha_{R2} \end{pmatrix} = E_p \begin{pmatrix} \alpha_\gamma \\ \alpha_{Br} \\ \alpha_{R1} \\ \alpha_{R2} \end{pmatrix}$$

Diagonalization of the Hamiltonian gives rise to four unique solutions for the four polariton branches with the energy of the LPB at  $k_{//}=0$  and the coupling constants tabulated below.

Cavity	LPB energy $k_{//}=0$	$\hbar\Omega_1$ (meV)	$\hbar\Omega_2$ (meV)	$\hbar\Omega_3$ (meV)
<b>M<sub>p</sub></b>	1.92481	185	23	90
<b>M<sub>n</sub></b>	1.75045	180	110	168
<b>B<sub>p</sub></b>	1.90440	185	50	160
<b>B<sub>n</sub></b>	1.75047	210	110	168

**Table S1.** Energy of the LPB at zero in-plane momentum and coupling constants for the four cavities M<sub>p</sub>, M<sub>n</sub>, B<sub>p</sub> and B<sub>n</sub>.

## Polariton population and polariton PL

The photoluminescence measured by a lens  $P$  is the light collected in the solid angle which subtends the lens itself, i.e.

$$P_\theta = \iint_{lens} d \cos\theta d\varphi I(\theta, \varphi), \quad (1)$$

where  $P_\theta$  is the solid angle PL density for an isotropic MC.

In order to convert polariton PL into polariton population we need to use the reciprocal space, i.e. the number of polariton states for unit surface  $D_\Omega$  corresponding to a certain wave vector region  $\Omega$

$$D_\Omega = \frac{1}{(2\pi)^2} \int_\Omega d^2 \mathbf{k}. \quad (2)$$

Given a certain polariton population density  $f_{\mathbf{k}}$ , the polariton population per unit surface is given by

$$N_\Omega = \frac{1}{(2\pi)^2} \int_\Omega d^2 \mathbf{k} f_{\mathbf{k}}. \quad (3)$$

Assuming isotropic conditions, it is useful to introduce cylindrical coordinates. In this case, the integral of the polariton population density over the LPB can be written as

$$N_{LP} = \frac{1}{(2\pi)^2} \int_0^{k_{max}} dk k \int_0^{2\pi} d\varphi f_{\mathbf{k}}. \quad (4)$$

Similarly, we could express the total photoluminescence of the LPB as

$$P_{LP} \propto \frac{1}{(2\pi)^2} \int_0^{k_{max}} dk k \int_0^{2\pi} d\varphi \frac{|a_\gamma|^2}{\tau_{cav}} f_{\mathbf{k}}, \quad (5)$$

where  $|a_\gamma|^2$  is the amplitude of the photon part of polariton of wave vector  $\mathbf{k}$  and  $\tau_{cav}$  is the confinement time of the microcavity. Assuming as usual that the in-plane wave vector is a conserved quantity, we can pass from the modulus of the wave vector  $k$  to the inclination angle  $\theta$  by using the following formula

$$k = E_k \frac{\eta}{\hbar c} \sin\theta, \quad (6)$$

with  $\eta$  the refractive index.

The PL emission can be then expressed as

$$P_{LP} \propto \frac{1}{(2\pi)^2} \int_0^{\theta_{max}} d\sin\theta E_{k(\theta)}^2 \frac{\eta^2 \sin\theta}{\hbar^2 c^2} \int_0^{2\pi} d\varphi \frac{|a_\gamma|^2}{\tau_{cav}} f_{k(\theta)}. \quad (7)$$

Comparing this expression with (1) we conclude that exists the follow proportionality relation between the observed PL  $I(\theta)$  and the polariton population density  $f_{k(\theta)}$

$$P_\theta \propto E_{k(\theta)}^2 \cos\theta |a_\gamma|^2 f_{k(\theta)}. \quad (8)$$

Therefore  $f_{k(\theta)}$  can be expressed as

$$f_{k(\theta)} \propto \frac{P_\theta}{E_{k(\theta)}^2 \cos\theta |a_\gamma|^2}. \quad (9)$$

We indeed employ the approximate proportionality  $P_\theta \propto I(\theta)$ , with the justified assumption for a smooth enough PL density.

## **Chapter 6. Generation of anti-Stokes fluorescence in a strongly coupled organic semiconductor microcavity**

### **6.1. Motivation of work**

In organic systems, it has been established that the vibrational modes of a molecule can assist the relaxation of uncoupled excitons from the exciton reservoir to polaritonic states in the lower polariton branch (LPB). Recently, a growing interest in how rovibrational modes of molecular materials interact with cavity polaritons has stimulated much theoretical work. In inorganic systems, similar processes have been studied theoretically and experimentally, where acoustic and LO phonons interact with polaritons, with anti-Stokes fluorescence (ASF) of LPB polaritons from an inorganic quantum-well strongly coupled microcavity recently reported. Here it was shown that polaritons that were optically injected at the bottom of the LPB could scatter to higher energy states along the same branch, utilising energy provided by phonons in the system.

Organic semiconducting materials used in strongly coupled microcavities are rich in rotational, vibrational and other low frequency modes, however relatively little is evident in the way of underpinning experimental evidence of phonon interaction with polaritons to support theory. Here, we provide direct experimental evidence for the interaction between cavity-polaritons with the surrounding thermal bath in a strongly coupled organic semiconductor microcavity; a process that results in anti-Stokes fluorescence.

First, we perform angular white-light reflectivity measurements to ensure that the microcavity operates in the strong coupling regime. Using temperature dependent photoluminescence measurements on control non-cavity films and on strongly coupled microcavities, we show that the excess energy needed to generate such anti-Stokes fluorescence is provided by the ground-state vibrational energy of the molecules. Time-resolved photoluminescence measurements on microcavities when excited resonantly (resulting in ASF) and non-resonantly show that both processes have similar time dynamics suggesting a very similar underlying mechanism. It is concluded that polaritons that are optically injected at the bottom of the LPB, can

pump molecules that exist in a vibrational excited ground-state creating an exciton reservoir. The exciton reservoir can then populate polariton states that are at a higher energy than the energy of the initial laser excitation.

By analyzing the angular PL distribution of the strongly coupled microcavities, we can convert PL intensity into relative polariton population. Following such analysis, we find that the relative population of cavity-polaritons corresponding to anti-Stokes fluorescence is up to 3 times higher compared to that of a comparable control film (shown in Figure 6, black and red lines). We believe this to be an important finding as the ability to generate anti-Stokes fluorescence efficiently may allow cavity structures to be created that undergo laser cooling. Indeed, it might even be possible to create an electrically pumped device that would undergo self-cooling by emitting polaritons. Work is currently planned to follow on such ideas and explore laser cooling in more detail.

## **6.2. Author contributions**

K.G. designed and fabricated the microcavities. K.G. performed the white-light reflectivity measurements. K.G., R.J. and D.M.C. measured the room-temperature photoluminescence from strongly coupled cavities and control non-cavity films. K.G. performed the temperature dependent measurements. K.G. and A.A. measured the time-resolved photoluminescence. K.G. analysed the data. K.G. wrote the manuscript with significant input from P.G.L. and D.G.L. who also supervised the project.

## **6.3. Publication**

In the following, we present the publication, as it appears online in the Journal ACS Photonics.

“Reprinted with permission from Georgiou K. et al., Generation of anti-Stokes fluorescence in a strongly coupled organic semiconductor microcavity, *ACS Photonics* 2018, 5, 11, 4343-4351. Copyright (2018) American Chemical Society.”

# Generation of Anti-Stokes Fluorescence in a Strongly Coupled Organic Semiconductor Microcavity

Kyriacos Georgiou,<sup>†</sup> Rahul Jayaprakash,<sup>†</sup> Alexis Askitopoulos,<sup>‡,§</sup> David M. Coles,<sup>†</sup> Pavlos G. Lagoudakis,<sup>\*,‡,§</sup> and David G. Lidzey<sup>\*,†</sup>

<sup>†</sup>Department of Physics and Astronomy, The University of Sheffield, Hicks Building, Hounsfield Road, Sheffield, S3 7RH, United Kingdom

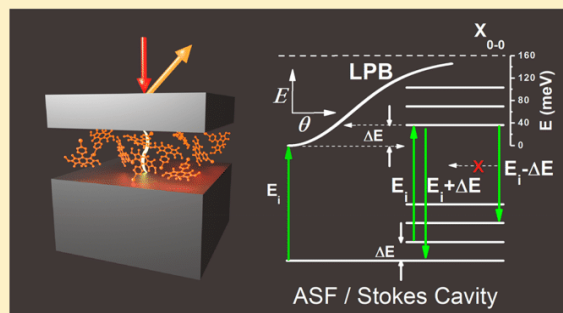
<sup>‡</sup>Department of Physics and Astronomy, University of Southampton, Southampton, SO17 1BJ, United Kingdom

<sup>§</sup>Skolkovo Institute of Science and Technology, Moscow 143026, Russia

## Supporting Information

**ABSTRACT:** We explore the generation of anti-Stokes fluorescence from strongly coupled organic dye microcavities following resonant ground-state excitation. We observe polariton emission along the lower polariton branch, with our results indicating that this process involves a return to the exciton reservoir and the absorption of thermal energy from molecules in a vibrationally excited ground-state. We speculate that the generation of a population of “hot” polaritons is enhanced by the fact that the cavity suppresses the emission of Stokes-shifted fluorescence, as it is energetically located below the cutoff frequency of the cavity.

**KEYWORDS:** exciton-polaritons, anti-Stokes fluorescence, organic semiconductor, microcavities



Over the past two decades, optical microcavities have been used to explore the physics of optical coupling between confined photons and molecular semiconductors.<sup>1–7</sup> Optical microcavities are structures that consist of two mirrors placed in close proximity that are separated by a layer of an optically active material. The mirrors confine the local electromagnetic field, and when it is resonant with the excitonic transition of the semiconductor, a reversible exchange of energy can occur between light and matter. In the strong-coupling regime, this results in the formation of quasi-particles termed cavity-polaritons that are coherent superposition of excitons and photons and have properties of both.<sup>8</sup> By coupling molecular materials with light, it is possible to engineer fascinating processes, such as polariton condensation,<sup>9–11</sup> superfluidity,<sup>6</sup> changes in the rate of chemical reactions,<sup>12,13</sup> and a modification of energy transfer pathways.<sup>14–17</sup>

The first microscopic models used to describe the strong coupling of molecules to light treated the molecules in the cavity as an ideal two-level system and neglected rotational or vibrational degrees of freedom.<sup>18</sup> Recently, however, there has been growing interest in understanding the role that the vibrational landscape plays in modifying basic processes in strongly coupled microcavities. Early experimental work on the resonant excitation of organic strongly coupled cavities demonstrated an enhancement of Stokes and anti-Stokes Raman scattering process when the energetic separation between initial and final states were degenerate with a

Raman mode of the molecular material within the cavity.<sup>19</sup> Follow-on studies established that the (Raman-active) vibrational modes of a molecule were able to assist the relaxation of uncoupled excitons from the “exciton reservoir” to polaritonic states along the lower polariton branch (LPB) by acting as a sink for excess energy.<sup>20,21</sup>

In inorganic semiconductor microcavities, a number of authors have explored the interactions between cavity-polaritons and acoustic and LO phonons.<sup>22–29</sup> For example, anti-Stokes fluorescence (ASF) was observed in strongly coupled optical microcavities containing ZnSe quantum wells<sup>30</sup> following resonant excitation of lower-branch polaritons,<sup>31</sup> with ASF used to achieve laser cooling of semiconductors.<sup>32–34</sup> In such microcavities,<sup>31</sup> the significant excitonic component of the cavity-polaritons was responsible for the interactions with thermal phonons, making them an important platform in which to study laser-cooling effects in semiconducting materials. Indeed, by exciting the LPB at  $k_{\parallel} = 0$ , the generation of fluorescence at lower energy is forbidden due to the near parabolic dispersion of cavity-polaritons.

In organic-semiconductor based microcavities, a growing interest in the interactions between cavity-polaritons and rovibrational modes of molecular materials has stimulated much theoretical research.<sup>35–41</sup> For example, it has been

Received: April 26, 2018

Published: October 19, 2018

predicted that electronic and nuclear degrees of freedom become decoupled in the strong coupling regime; an effect that reduces disorder and enhances the exciton coherence length.<sup>36</sup> Furthermore, models that include rotational and vibrational degrees of freedom indicate that dark states within a microcavity (corresponding to uncoupled excitons in a two-level system) can also be affected by strong coupling.<sup>37</sup>

In this paper, we provide evidence for the interaction between cavity-polaritons with the local thermal bath in a strongly coupled microcavity containing a film of the fluorescent molecular dye bromine-substituted boron-dipyrromethene (BODIPY-Br). We use optical spectroscopy to show that ASF can be generated by exciting the LPB around  $k_{\parallel} = 0$  and perform temperature-dependent measurements that show that by reducing the overall thermal energy available in the system, we can control the intensity of polariton ASF, suggesting a thermally assisted process. We utilize fluorescence lifetime measurements to demonstrate that the polariton ASF process involves a “return” of energy to the exciton reservoir. We find that the overall integrated population of “hot” polaritons in the resonantly excited strongly coupled cavity (corrected for the number of photons absorbed) is around  $3\times$  larger than the relative number of ASF photons generated from a control (noncavity) film of BODIPY-Br. We speculate that the cavity suppresses the emission of Stokes-shifted luminescence, as it is located energetically below the cutoff frequency of the cavity.

The chemical structure of BODIPY-Br, together with its absorption and fluorescence are shown in Figure 1a. Here, the peak in absorption and fluorescence observed at around 530 and 550 nm, respectively, corresponds to the 0–0 electronic transition of the BODIPY-Br monomer, with the 20 nm difference between the wavelength of the absorption and emission maxima occurring as a result of a Stokes shift.<sup>42</sup> The absorption shoulder at 503 nm corresponds to a 0–1 vibrational transition. The shoulder in PL emission at 586 nm has a more complex origin and corresponds to emission from the 0–1 vibrational transition, together with emission from excited state dimers (excimers).<sup>43</sup>

To fabricate microcavities, an optically inert polymer matrix (polystyrene: PS) was doped with BODIPY-Br at a dye/polymer concentration of 20%/80% by mass and spin-cast onto a 200 nm thick silver mirror forming a film having a thickness of 260 nm. A film of poly(vinyl alcohol) (PVA) was spin-cast on top of the BODIPY-Br layer to tune the cavity length, and a semitransparent silver mirror was then thermally evaporated onto the organic bilayer, having a thickness of 32 nm. The resultant  $\lambda$ -cavity had a  $Q$ -factor of  $\sim 50$ . A schematic of a typical cavity is shown in Figure 1b. We have recently shown that the BODIPY-Br 0–0 monomer excitonic transition can undergo strong coupling,<sup>44</sup> and when incorporated into higher  $Q$ -factor cavities based on two distributed Bragg reflectors (DBRs), such cavities demonstrate polariton condensation.<sup>11</sup>

Using white light reflectivity measurements, we find that the cavities we have constructed are in the strong-coupling regime. Here, all measurements were performed through the semitransparent top mirror, allowing light to be coupled into and out of the cavity. We plot the cavity reflectivity as a function of external viewing angle in Figure 1c. We find that three dispersive optical features are detected, which can be described using a three-level coupled-oscillator model, as plotted in Figure 1c. From this, we determine a Rabi splitting of 210 and

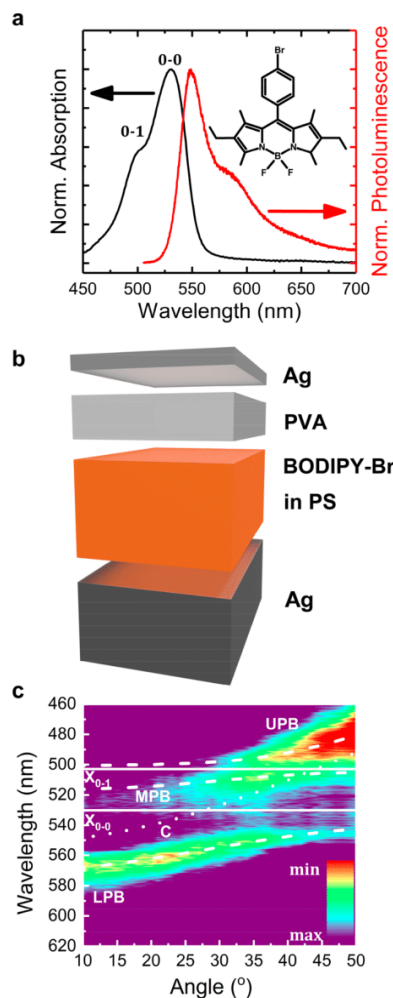


**Figure 1.** (a) Normalized absorption and photoluminescence of a control film along with the chemical structure of BODIPY-Br. (b) Schematic of the metal/metal mirror microcavities. A layer of PVA is used to protect the organic dye from the deposition of the top metal mirror and adjust the thickness of the microcavity. (c) Angular resolved white light reflectivity measurements of the microcavity recorded at room temperature. Included on the plot are the results of a three-level coupled oscillator model. LPB, MPB, and UPB: lower, middle, and upper polariton branches. C,  $X_{0-0}$ , and  $X_{0-1}$ : cavity mode, exciton from the 0–0 transition, and exciton from the 0–1 vibrational transition.

80 meV between the cavity photon and the transitions  $X_{0-0}$  and  $X_{0-1}$ , respectively. This suggests that the cavity photon (C) undergoes strong coupling with the 0–0 electronic transition of BODIPY-Br, with the 0–1 vibronic transition of BODIPY-Br remaining in an intermediate-coupling regime.<sup>45</sup> Our model also indicates that the cavity is negatively detuned, with the energetic separation between  $X_{0-0}$  and the cavity photon at  $\theta = 0^\circ$  being 85 meV. In the Supporting Information, we plot the Hopfield coefficients for the three polariton branches (see Supporting Information, Figure S1). From this analysis, we determine that the bottom of the LPB is composed of 69% cavity photon, with the remainder being a mixture of  $X_{0-0}$  and  $X_{0-1}$  (29% and 2%, respectively).

We have explored the emission of fluorescence following wavelength-dependent excitation of strongly coupled cavities and control (noncavity) films of BODIPY-Br/PS as a function of temperature. Room temperature emission from a control film of BODIPY-Br/PS performed as a function of excitation wavelength is shown in Figure 2. Here, the excitation

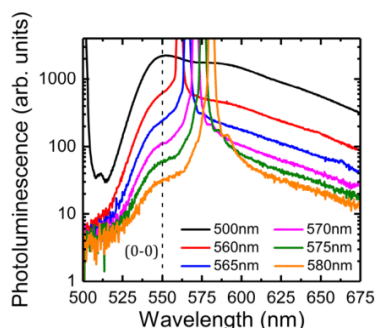


**Figure 2.** Photoluminescence and frequency up-conversion of a BODIPY-Br/PS noncavity thin film for high direct absorption (500 nm) and sub-band gap (560–580 nm) excitation wavelength. The dashed line shows the peak emission wavelength (550 nm) of the  $X_{0-0}$  electronic transition.

wavelength was varied between 500 nm (corresponding to a spectral region with high direct absorption) and 580 nm (a “sub-band gap” spectral region corresponding to very low direct absorption). The vertical dashed line at 550 nm corresponds to the peak emission wavelength of the  $X_{0-0}$  electronic transition of BODIPY-Br. It can be seen that the BODIPY-Br undergoes clear frequency up-conversion, with ASF emitted at an energy more than 160 meV above the laser excitation. This effect is enhanced at excitation wavelengths

closer to the edge of the BODIPY-Br absorption band (560 nm) with the intensity reducing with increasing excitation wavelength.

We have also characterized ASF emission from control films as a function of temperature, with excitation performed at different wavelengths. Typical data is shown in Figure 3a,b recorded at temperatures between 80 and 300 K following excitation at 548 and 558 nm, respectively. We find that as the temperature is reduced, the intensity of ASF is reduced, with its spectral distribution shifting to longer wavelengths. Figure 3c plots emission spectra recorded from a BODIPY-Br/PS control film as a function of temperature following excitation at 500 nm. Here, we again observe a redistribution of PL emission to longer wavelengths as the temperature is reduced; an effect that we have previously shown results from emission mainly originating from isolated BODIPY-Br monomers at room temperature and from intermolecular excimers at 80 K.<sup>43</sup>

Previous work has explored ASF in a number of organic materials<sup>33,34</sup> and it has been proposed that optical excitation excites a subset of molecules that are initially in a vibrationally excited ground state to a higher lying  $S_1$  state. On relaxation, the molecules return to their electronic (0–0) ground state, with the luminescence emitted having an energy greater than that of the incident photon. Following the approach outlined in refs 33 and 34, we calculate an activation energy for the ASF emission. Here, measurements were made on a control film, with emission intensity measured at 547 nm as a function of temperature ( $I(T)$ ) following photoexcitation at 568 nm. Typical data is plotted in Figure 3d, which we fit using an Arrhenius equation of the form ( $I(T) = Ce^{-E_A/k_B T}$ ), where  $E_A$  is an activation energy of around 27 meV. This activation energy has previously been associated with the energy difference between the energy of the excitation photons and the 0–0 absorption transition. However, this is clearly not the case

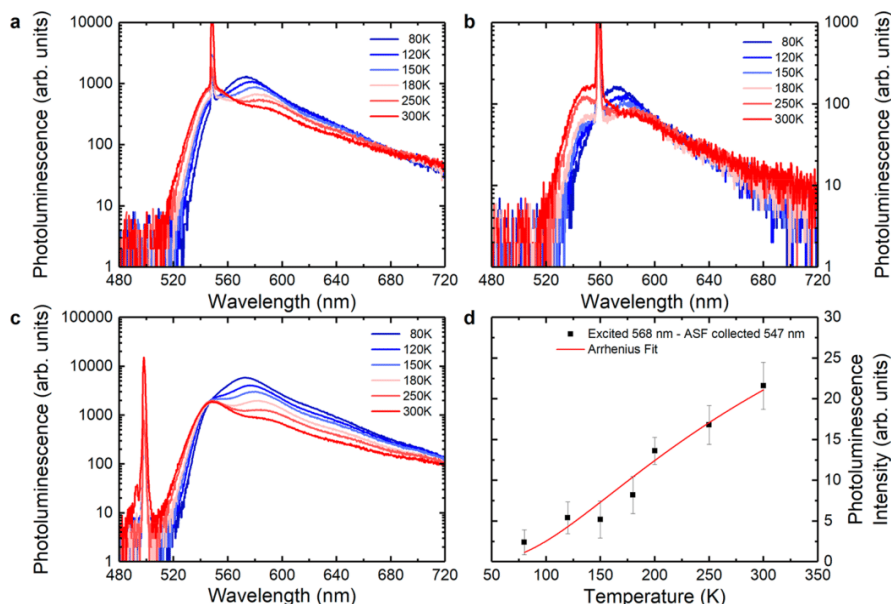


**Figure 3.** Temperature-dependent photoluminescence and frequency up-conversion of a BODIPY-Br/PS noncavity thin film following laser excitation at (a) 548, (b) 558, and (c) 500 nm. (d) Temperature dependence of ASF intensity of a noncavity BODIPY-Br/PS thin film when excited at 568 nm and collected at 547 nm, along with an Arrhenius fit with an activation energy of around 27 meV.

here, as the activation energy (27 meV) is much smaller than the energy separation between the 0–0 transition and the laser excitation energy (in this case 156 meV). Indeed, even when we excite the film at shorter wavelengths, we only observe a small change in the activation energy (see Supporting Information, Figure S3). We note that, in experiments on Rhodamine 101 in solution,<sup>34</sup> the activation energy and the calculated energy difference between the excitation and the 0–0 transition were found to be in good agreement. However, measurements on Rhodamine B dispersed into a solid film<sup>33</sup> indicated that the activation energy was 62 meV (500 cm<sup>-1</sup>) smaller than its expected value, with this discrepancy ascribed to solvent effects. In our work on BODIPY-Br, we find a clear discrepancy of around 120 meV between the measured activation energy and the energy difference between excitation and the 0–0 transition energy. The reason for this discrepancy is not clear; however, we suspect it may result from the fact that BODIPY-Br emission spectra has a significant temperature dependence that results from migration of energy to intermolecular excimer states (see temperature-dependent PL spectra shown in Figure 3a–c). Nevertheless, the similarity between our findings and those in ref 33 suggests that the ASF emission generated in BODIPY-Br/PS control films also results from the direct photoexcitation of molecules that are in a vibrationally excited ground-state.

In the following section, we analyze ASF emission from microcavities containing strongly coupled BODIPY-Br. Figure 4 shows typical data from a microcavity in which the LPB was excited resonantly at 572 nm; a wavelength corresponding to the bottom of the LPB, with temperature progressively tuned between 77 and 292 K. Here, a small blue-shift of the polariton dispersion by around 1 nm is observed over this temperature range; an effect that most likely results from a small thermally induced contraction of the cavity optical path length. The

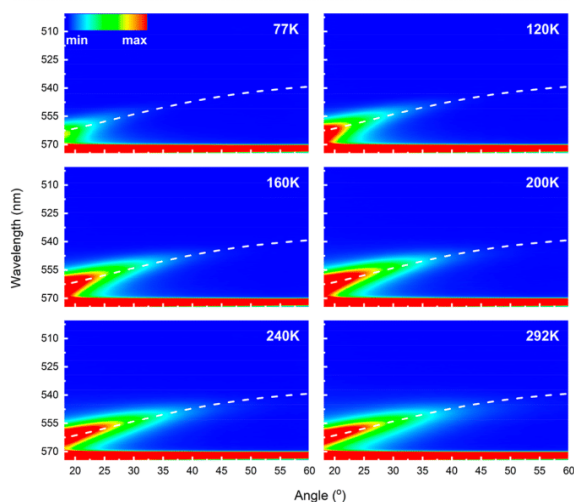


**Figure 4.** Temperature-dependent photoluminescence of the lower polariton branch following resonant excitation at 572 nm showing the anti-Stokes fluorescence vs emission angle. The dashed lines indicate the energy of the lower polariton branch as derived from the white light reflectivity measurements of the microcavity using a three-level coupled oscillator model. The normalized false color scale was saturated at around 0.7 to improve the visibility of the lower polariton branch emission.

dashed line in Figure 4 shows the dispersion of the LPB, as fitted using the measured white light reflectivity (Figure 1c), with the color scale quantifying the intensity of polariton emission. It can be seen that, at 292 K, significant luminescence emission is observed along the LPB at energies up to 95 meV above that of the laser excitation (which can be identified by the horizontal “red” band), a result consistent with ASF. We find that as the cavity temperature is progressively decreased, emission is still observed along the LPB, however, the intensity of ASF reduces with temperature and at low temperatures emission is concentrated around the bottom of the LPB. Note that while it was possible to observe ASF that extended 160 meV above the energy of the laser in the noncavity control films, it was not possible to observe ASF at such large energies above the excitation laser in the strongly coupled cavity shown in Figure 1c. The reason for this is that the dispersion of the LPB flattens considerably as it approaches the energy of the exciton, and thus, such large energy separations are inaccessible. We have, however, observed polariton ASF in cavities having a larger negative detuning, permitting a greater energy separation (~135 meV) to be achieved between excitation and ASF emission (see Figure S5 in Supporting Information). It is clear, however, that the initially excited states in such negatively detuned cavities are highly photon-like in character (having a total photon fraction of 97%).

To understand the ASF process in more detail, Figure 5a plots the intensity of polariton ASF at an angle of 30° (corresponding to a wavelength of 555 nm) as a function of

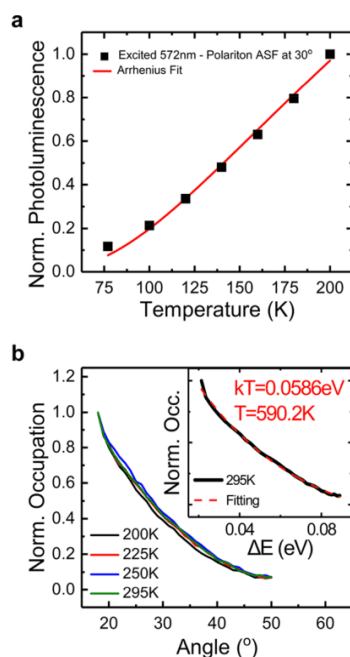


**Figure 5.** (a) Normalized intensity of the lower polariton branch emission following resonant excitation at 572 nm, recorded at an angle of 30° (555 nm), for temperatures between 77 and 200 K along with an Arrhenius fit. (b) Normalized occupation of the lower polariton branch following resonant (572 nm) excitation for four different temperatures. The inset shows the Boltzmann fitting of the room temperature lower polariton branch occupation.

temperature, following excitation at 572 nm. We again use an Arrhenius fit to describe the temperature-dependent intensity and extract an activation energy of around 27 meV; a result in close agreement with that determined from the noncavity BODIPY/PS control film (see Figure 3d).

In Figure 5b we plot the normalized polariton population along the LPB as a function of external angle. Here, polariton population ( $P_{\text{LPB}}$ ) is calculated using  $P_{\text{LPB}}(\theta) = I(\theta)/|\alpha_c(\theta)|^2$ , where  $I$  is the intensity of luminescence and  $|\alpha_c|^2$  is the photon fraction of the LPB at angle  $\theta$  (calculated using a 3-level coupled oscillator model, see Supporting Information). It can be seen in Figure 5a that, while the intensity of ASF along the LPB reduces as a function of temperature, the relative distribution of polariton population along the LPB does not change (see Figure 5b). We can, in fact, determine an effective temperature of the polaritons along the LPB by performing a Boltzmann fit, as shown in the inset of Figure 5b. We find that the effective temperature of the polaritons to be around 590 K. The fact that this effective temperature is approximately constant as a function of cavity temperature suggests that the polariton population does not reach thermal equilibrium, a result consistent with the very fast radiative lifetime of polaritons in a low  $Q$ -factor cavity.

Our measurements demonstrate therefore that following excitation of polaritons at the bottom of the LPB, a process occurs in which states at higher energy along the LPB are populated. The apparent similarity between the activation energy for ASF emission in both the cavity and control films indicates that we should expect a similar underlying mechanism. To explore this in more detail, we have measured the dynamics of polariton emission from states along the LPB using a streak camera following both resonant and nonresonant excitation. Typical data is shown in Figure 6a; photoluminescence is recorded from the cavity at around 556 nm (corresponding to an angle  $\theta = 28^\circ$ ), where the cavity is either excited resonantly at 570 nm or nonresonantly at 400 nm. We find the decay dynamics are in both cases biexponential, with polaritons excited resonantly decaying with a lifetime of 57 and 286 ps and relative amplitudes of 0.645 and 0.355, respectively (fit to the data having an adjusted  $R$ -squared value of 0.999). Polaritons excited nonresonantly instead decay with a lifetime of 71 and 518 ps and relative amplitudes of 0.59 and 0.41, respectively (adjusted  $R$ -squared fit value of 0.997). Our results indicate therefore that the ASF polariton decay lifetime is a factor of approximately 2 shorter than emission generated following nonresonant excitation (where the initial photo-generated states are excitons). We believe that the relative similarity between the recorded lifetimes indicates that the ASF process must involve interaction with states in the exciton reservoir (the radiative lifetime of polaritons in this low  $Q$ -factor cavity is estimated to be around 30 fs). The reason for this apparent reduction of lifetime most likely indicates that the ASF process is subject to additional nonradiative losses, a conclusion consistent with the higher intensity of luminescence emitted when the cavity is pumped nonresonantly compared to resonantly generated ASF emission.

We can further evidence the importance of uncoupled excitons in mediating the polariton ASF process by modifying the energetic distribution of states within the exciton reservoir. Here, a molecular “acceptor” species was introduced at low concentration into a BODIPY-Br/PS film, with the acceptor positioned at an energy below that of the LPB. The acceptor molecules used were based on a related molecular dye

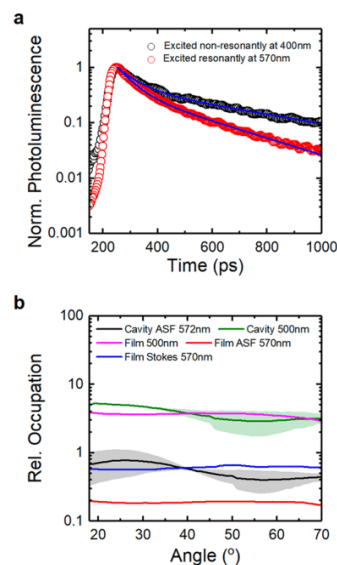


**Figure 6.** (a) Transient dynamics of the lower polariton branch emission at an angle of  $28^\circ$  following resonant (570 nm) and nonresonant (400 nm) excitation. (b) Lower polariton branch relative occupation following resonant (572 nm, black line) and nonresonant (500 nm, green line) excitation as a function of emission angle. Angular-resolved anti-Stokes (red line) and Stokes (blue line) fluorescence from a control film excited at 570 nm, as well as angular-resolved fluorescence (magenta line) excited at 500 nm. The colored shaded areas indicate the uncertainty of the measurement.

BODIPY-R that has a reduced electronic energy gap as a result of chemical modification. This molecule acts as a low-energy acceptor, with control measurements on blends of BODIPY-Br/BODIPY-R (20%/0.75% by mass) dispersed in polystyrene indicating almost complete energy transfer (>99%) from BODIPY-Br to BODIPY-R by dipole–dipole coupling. This efficient dipole–dipole energy transfer can be seen in Supporting Information, Figure S6a, where we plot absorption and PL emission from a blend BODIPY-Br/BODIPY-R/PS film, with excitation performed at 473 nm. Here, PL is dominated by emission from BODIPY-R, with emission from BODIPY-Br being almost totally absent. In Figure S6b, we show emission from the same blend, where excitation was performed at 575 nm. Again, emission is dominated by BODIPY-R, with no ASF from BODIPY-Br detected.

We have explored the photophysics of such BODIPY-Br/BODIPY-R/PS films placed within a microcavity (with the cavity having a very similar mode structure as the BODIPY-Br microcavity described above). Here, the BODIPY-Br was strongly coupled, however, by using the BODIPY-R acceptor at low concentration, we ensured that it could not undergo strong coupling. We find that when such a BODIPY-Br/BODIPY-R/PS blend was used as the active layer in a microcavity, no detectable ASF was emitted from the cavity on resonant excitation of the LPB at 572 nm. This indicates that any polaritons that return to the exciton reservoir undergo energy transfer to weakly coupled BODIPY-R exciton states positioned at lower energy rather than scattering back to higher energy polariton states. We conclude, therefore, that the ASF process evidenced in strongly coupled BODIPY-Br microcavities is mediated by an exchange with the exciton

reservoir and does not involve a direct polariton to polariton scattering mechanism along the lower polariton branch.

We can gain additional insight into the ASF process, through a quantitative comparison of the angular dependence of ASF emission detected from a cavity and a noncavity control film. This is shown in Figure 6b, where we plot the relative population of cavity polaritons ( $P_{\text{LPB}}(\theta)$ ) as a function of angle along the LPB at room temperature, with data shown for either resonant (572 nm) or nonresonant (500 nm) excitation. On the same figure, we plot the intensity of Stokes and anti-Stokes emission as a function of angle recorded from a control (noncavity) BODIPY-Br film on excitation at 570 nm (corresponding to sub-band gap excitation). Note that we do not apply any correction to the control film emission intensity and assume there is a one-to-one correspondence between photoluminescence intensity and the exciton population. However, we have measured the relative number of excitation photons that were absorbed by both the cavity and the control film following resonant and nonresonant excitation and applied an appropriate correction in both cases to allow us to compare relative populations. For completeness, we also plot the intensity of emission as a function of angle generated from the control film following excitation at 500 nm.

It can be seen that when the cavity and the control film are excited at 500 nm (green and magenta lines, respectively), we find that a very similar population of states are created. This indicates that, in both the cavity and the control film, the initially generated “hot” excitons undergo a similar relaxation process. In the cavity, such relaxed excitons form a reservoir of states that then populate states along the LPB by radiatively pumping its photonic component with high efficiency; a result in accord with our previous findings.<sup>44</sup> It can be also seen that the angular emission from the cavity, when excited at 500 nm (green line) is much higher than that following excitation at 572 nm (black line). This indicates that the ASF process in a cavity is subject to additional unknown nonradiative losses as opposed to a cavity when excited at significantly shorter wavelengths; a result consistent with the enhanced decay rate of ASF emission shown in Figure 6a.

When instead the cavity and control film are excited at 572 and 570 nm (corresponding to the bottom of the LPB and a sub-band gap region of BODIPY-Br, respectively), we find that the total angle-integrated polariton population that results in ASF emission from the cavity is 3× larger than the relative number of ASF photons emitted by the film (black and red lines, respectively). When, however, we also include Stokes shifted emission (blue line) from the control film (i.e., emission at wavelengths greater than the excitation laser at 570 nm), we find that the angle-integrated ASF polariton population from the LPB and the overall angle-integrated fluorescence from the control film (Stokes and anti-Stokes) are quantitatively similar.

We offer the following picture to explain this effect (see schematic shown in Figure 7a-c). On excitation of the noncavity control film at an energy  $E_i$  below the energy-gap (i.e., at 570 nm), we select molecules in a vibrationally excited ground-state ( $\Delta E$ ) and raise such molecules to the zero-phonon (1–0) excited state. On return to their ground state, the luminescence from such molecules includes the initial ground-state vibrational energy ( $E_i + \Delta E$ ), and thus, part of the emitted luminescence occurs at shorter wavelengths (corresponding to ASF, see Figure 7a). Note that Stokes emission is

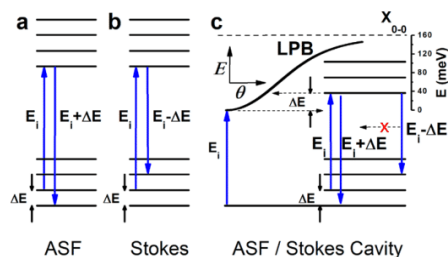


**Figure 7.** Schematic of (a) anti-Stokes fluorescence (ASF) and (b) Stokes fluorescence in a control film as well as (c) in a microcavity. Here, part (c) indicates the proposed mechanism in which anti-Stokes fluorescence is generated following resonant excitation of the bottom of the lower polariton branch in a strongly coupled organic microcavity.

also possible, where the molecule returns to a vibrationally excited ground-state ( $E_i - \Delta E$ ; see Figure 7b).

On resonant excitation of the cavity at the bottom of the LPB, polaritons are created that we speculate can exchange energy with weakly coupled electronic states in the exciton reservoir. Here, such weakly coupled states most likely correspond to molecules in a vibrationally excited ground-state ( $\Delta E$ ), with this excitation process probably involving the direct absorption of the photon component of the polariton. This process then creates a weakly coupled reservoir exciton. Again, we assume the initially excited polariton state has an energy  $E_i$  (see Figure 7c), with the reservoir exciton thus created having an energy of ( $E_i + \Delta E$ ). This exciton is then able to radiatively pump polaritons along the LPB<sup>44</sup> having an energy ( $E_i + \Delta E$ ).

This simple model can also qualitatively explain the relative enhancement of “hot” polariton population corresponding to ASF emission observed when resonantly exciting the cavity as compared to the control film. If the weakly coupled exciton created in the reservoir instead undergoes Stokes emission, the photon emitted will have an energy ( $E_i - \Delta E$ ) and will thus be below the cutoff frequency of the cavity (see Figure 7c). For this reason, we expect Stokes-shifted emission to be relatively suppressed (via the Fermi’s Golden Rule) through the relatively low density of optical states at such energies. This results in a redistribution of emission, where anti-Stokes emission becomes the dominant decay mechanism. Note, however, that this simple picture ignores the fact that there may as well be a high density of waveguided modes that exist at high wavevector into which Stokes shifted emission could couple. At the moment, the relative importance of such waveguide modes is not understood, and further detailed modeling is required to produce a more complete picture of the total density of optical states into which molecules could emit Stokes or anti-Stokes radiation.

To conclude, we have provided direct experimental evidence of anti-Stokes fluorescence (ASF) from a strongly coupled organic-semiconductor microcavity that is resonantly excited at the bottom of the lower polariton branch (LPB). We have characterized the ASF as a function of temperature, and have compared it with that emitted by a control (noncavity) film composed of the same organic semiconductor that is excited at a very similar wavelength. We find that the angle-integrated “hot” polariton population from the cavity LPB is around 3 times larger than that corresponding to ASF emission by the control film. By measurement of the dynamics of ASF

emission, we conclude that this process involves a return of the photogenerated polaritons to a weakly coupled exciton reservoir. We propose a picture in which the polariton states return to the reservoir by exciting molecules that are in a vibrationally excited ground-state. The excitons created are then able to optically pump polariton states above the bottom of the LPB, with the excess energy provided by the initial ground-state vibrational energy of the molecule. The relative enhancement of ASF states results from the fact that Stokes-shifted fluorescence is suppressed as its energy is below the cutoff frequency of the cavity.

Our measurements contribute to the growing understanding of the importance of the role played by vibrational modes in underpinning basic processes in strongly coupled organic semiconductor microcavities,<sup>20,21,35–40,46–49</sup> and it will clearly be important to include such processes when constructing a full model of organic exciton-polariton condensation. We also expect that structures similar to those explored may permit a study of the physics of laser cooling. Critically, the ability to undergo laser cooling at room temperature distinguishes organic-based systems from inorganic-semiconductor based microcavities that (in many cases) only demonstrate polaritonic effects at cryogenic temperatures. Note however that we have not yet evidenced laser cooling in the cavities or films studied. Clearly, to create a cooling effect, the energy flux entering the cavity must be smaller than that leaving the cavity, however this is unlikely to be the case at present. Indeed, the BODIPY-Br films used have a relatively low (~5%) photoluminescence quantum efficiency (PLQE) as a result of molecular aggregation,<sup>43</sup> and thus, a significant quantity of the absorbed laser is expected to be dissipated as heat. Nevertheless, we expect that strongly coupled cavities containing molecular dyes having a significantly higher PLQE may allow laser cooling effects to be explored at room temperature.

## METHODS

**Sample Preparation.** Polystyrene (PS) having an average molecular weight ( $M_w$ ) of ~192000 was dissolved in toluene at a concentration of 35 mg mL<sup>-1</sup>. Poly vinyl alcohol (PVA) was dissolved in DI water at a concentration of 35 mg mL<sup>-1</sup>. BODIPY-Br was added into the PS/toluene solution at a concentration of 20% by mass. Thin control films were spin-cast on quartz-coated glass substrates. To fabricate a microcavity, a 200 nm thick silver mirror was thermally evaporated on a quartz-coated glass substrate using an Auto 360 Edwards thermal evaporator. BODIPY-Br/PS and PVA layers were then spin-cast on top of the silver mirror. The thickness of the organic layers was measured using a Bruker DektakXT profilometer and the spin-speed of the spin coater was adjusted to achieve the desired thickness. The top semitransparent silver mirror was then thermally evaporated to have a thickness of 32 nm.

**Angular White Light Reflectivity.** White light reflectivity measurements were performed through the top semitransparent mirror using light from a fiber-coupled Halogen-Deuterium lamp that was imaged using two lenses onto the cavity surface, with the reflected light collected using a second pair of lenses and imaged into an Andor Shamrock CCD spectrometer. Both pairs of lenses were mounted on motorized optical rails fixed to a common rotation stage, with reflectivity measurements performed as a function of angle in steps of 1°.

**Fluorescence Measurements.** The microcavities and control film were mounted in a liquid N<sub>2</sub> cryostat, with excitation performed using a Fianium supercontinuum white light laser emitting 6 ps pulses at a repetition rate of 40 MHz. Laser light was first filtered using a SPEX 270 M monochromator having a bandwidth of 1.7 nm, allowing the excitation wavelength to be tuned over the range of 500 to 600 nm. The filtered laser light was then coupled into an optical fiber and imaged onto the sample surface. The resultant emission was collected at external angles between 18° and 70° using the same optical rail setup used in reflectivity measurements. All data is corrected for the Lambertian response of the system. All microcavities were excited at normal incidence ( $k_{||} = 0$ ).

**Streak Camera Measurements.** For nonresonant excitation measurements (400 nm) a frequency-doubled Ti:sapphire regenerative amplifier was used with a 180 fs pulse length, while for the quasi resonant excitation (570 nm) an optical parametric oscillator was used with a spectrally filtered bandwidth of 2 nm and 550 fs pulse length. Both measurements were performed with a 100 kHz repetition rate, with the transient emission dynamics recorded using a streak camera with a temporal resolution of 2 ps.

## ASSOCIATED CONTENT

### Supporting Information

The Supporting Information is available free of charge on the ACS Publications website at DOI: 10.1021/acsp Photonics.8b00552.

Three-level coupled oscillator model and additional optical characterization of control films (PDF).

## AUTHOR INFORMATION

### Corresponding Authors

\*E-mail: d.g.lidzey@sheffield.ac.uk.

\*E-mail: pavlos.lagoudakis@soton.ac.uk.

### ORCID

Kyriacos Georgiou: 0000-0001-5744-7127

David M. Coles: 0000-0003-4808-6395

Pavlos G. Lagoudakis: 0000-0002-3557-5299

David G. Lidzey: 0000-0002-8558-1160

### Author Contributions

K.G., P.G.L., and D.G.L. designed the experiments. K.G. fabricated the samples. K.G., R.J., and D.M.C. performed the reflectivity and steady state fluorescence measurements. K.G. and A.A. performed the transient emission measurements. K.G., R.J., A.A., and D.M.C. analyzed the data. K.G., P.G.L., and D.G.L. wrote the manuscript. All authors discussed the results and contributed to the manuscript.

### Notes

The authors declare no competing financial interest.

## ACKNOWLEDGMENTS

We thank Marco Cavazzini and Francesco Galleotti (Milano) for the synthesis of the BODIPY-Br used in these experiments. We thank Zhen Shen and Lizhi Gai (Nanjing University) for the synthesis of the BODIPY-R. We are grateful to Paolo Michetti (Dresden University), Jenny Clark, and Andrew J. Musser (University of Sheffield) for fruitful discussions. We thank the U.K. EPSRC for funding this work via the Programme Grant “Hybrid Polaritonics” (EP/M025330/1)

and for funding a Ph.D. scholarship for K.G. through a DTG allocation.

## REFERENCES

- (1) Lidzey, D. G.; Bradley, D. D. C.; Skolnick, M. S.; Virgili, T.; Walker, S.; Whittaker, D. M. Strong Exciton-Photon Coupling in an Organic Semiconductor Microcavity. *Nature* **1998**, *395*, 53–55.
- (2) Lidzey, D. G.; Bradley, D. D. C.; Virgili, T.; Armitage, a.; Skolnick, M. S.; Walker, S. Room Temperature Polariton Emission from Strongly Coupled Organic Semiconductor Microcavities. *Phys. Rev. Lett.* **1999**, *82* (16), 3316–3319.
- (3) Lidzey, D. G.; Bradley, D. D. C.; Armitage, A.; Walker, S.; Skolnick, M. S. Photon-Mediated Hybridization of Frenkel Excitons in Organic Semiconductor Microcavities. *Science* **2000**, *288* (5471), 1620–1623.
- (4) Kéna-cohen, S.; Forrest, S. R. Room-Temperature Polariton Lasing in an Organic Single-Crystal Microcavity. *Nat. Photonics* **2010**, *4*, 371–375.
- (5) Lerario, G.; Ballarini, D.; Fieramosca, A.; Cannavale, A.; Genco, A.; Mangione, F.; Gambino, S.; Dominici, L.; De Giorgi, M.; Gigli, G.; Sanvitto, D. High-Speed Flow of Interacting Organic Polaritons. *Light: Sci. Appl.* **2017**, *6*, e16212.
- (6) Lerario, G.; Fieramosca, A.; Barachati, F.; Ballarini, D.; Daskalakis, K. S.; Dominici, L.; De Giorgi, M.; Maier, S. A.; Gigli, G.; Kéna-Cohen, S.; Sanvitto, D. Room-Temperature Superfluidity in a Polariton Condensate. *Nat. Phys.* **2017**, *13*, 837–841.
- (7) Coles, D.; Flatten, L. C.; Sydney, T.; Hounslow, E.; Saikin, S. K.; Aspuru-Guzik, A.; Vedral, V.; Tang, J. K. H.; Taylor, R. A.; Smith, J. M.; Lidzey, D. G. A Nanophotonic Structure Containing Living Photosynthetic Bacteria. *Small* **2017**, *13*, 1701777.
- (8) Weisbuch, C.; Nishioka, M.; Ishikawa, A.; Arakawa, Y. Observation of the Coupled Exciton-Photon Mode Splitting in a Semiconductor Quantum Microcavity. *Phys. Rev. Lett.* **1992**, *69* (23), 3314–3317.
- (9) Plumhof, J. D.; Stoeferle, T.; Mai, L.; Scherf, U.; Mahrt, R. F. Room-Temperature Bose–Einstein Condensation of Cavity Exciton-Polariton in a Polymer. *Nat. Mater.* **2014**, *13*, 247–252.
- (10) Daskalakis, K. S.; Maier, S. a.; Murray, R.; Kéna-cohen, S. Nonlinear Interactions in an Organic Polariton Condensate. *Nat. Mater.* **2014**, *13*, 271–278.
- (11) Cookson, T.; Georgiou, K.; Zasedatelev, A.; Grant, R. T.; Virgili, T.; Cavazzini, M.; Galeotti, F.; Clark, C.; Berloff, N. G.; Lidzey, D. G.; Lagoudakis, P. G. A Yellow Polariton Condensate in a Dye Filled Microcavity. *Adv. Opt. Mater.* **2017**, *5* (18), 1700203.
- (12) Hutchison, J. A.; Schwartz, T.; Genet, C.; Devaux, E.; Ebbesen, T. W. Modifying Chemical Landscapes by Coupling to Vacuum Fields. *Angew. Chem., Int. Ed.* **2012**, *51*, 1592–1596.
- (13) Hutchison, J. A.; Liscio, A.; Schwartz, T.; Canaguier-Durand, A.; Genet, C.; Palermo, V.; Samori, P.; Ebbesen, T. W. Tuning the Work-Function via Strong Coupling. *Adv. Mater.* **2013**, *25*, 2481–2485.
- (14) Coles, D. M.; Somaschi, N.; Michetti, P.; Clark, C.; Lagoudakis, P. G.; Savvidis, P. G.; Lidzey, D. G. Polariton-Mediated Energy Transfer between Organic Dyes in a Strongly Coupled Optical Microcavity. *Nat. Mater.* **2014**, *13*, 712–719.
- (15) Zhong, X.; Chervy, T.; Wang, S.; George, J.; Thomas, A.; Hutchison, J. A.; Devaux, E.; Genet, C.; Ebbesen, T. W. Non-Radiative Energy Transfer Mediated by Hybrid Light-Matter States. *Angew. Chem., Int. Ed.* **2016**, *55*, 6202–6206.
- (16) Zhong, X.; Chervy, T.; Zhang, L.; Thomas, A.; George, J.; Genet, C.; Hutchison, J.; Ebbesen, T. W. Energy Transfer between Spatially Separated Entangled Molecules. *Angew. Chem., Int. Ed.* **2017**, *56*, 9034–9038.
- (17) Georgiou, K.; Michetti, P.; Gai, L.; Cavazzini, M.; Shen, Z.; Lidzey, D. G. Control over Energy Transfer between Fluorescent BODIPY Dyes in a Strongly-Coupled Microcavity. *ACS Photonics* **2018**, *5* (1), 258–266.
- (18) Michetti, P.; Mazza, L.; La Rocca, G. C.. Strongly Coupled Organic Microcavities. In *Organic Nanophotonics, Nano-Optics and Nanophotonics*; Sheng, Y., Ed.; Springer: Berlin, 2015; pp 39–68.
- (19) Tartakovskii, A.; Emam-Ismael, M.; Lidzey, D. G.; Skolnick, M. S.; Bradley, D. D. C.; Walker, S.; Agranovich, V. M. Raman Scattering in Strongly Coupled Organic Semiconductor Microcavities. *Phys. Rev. B: Condens. Matter Mater. Phys.* **2001**, *63* (12), 121302.
- (20) Coles, D. M.; Michetti, P.; Clark, C.; Tsoi, W. C.; Adawi, A. M.; Kim, J. S.; Lidzey, D. G. Vibrationally Assisted Polariton-Relaxation Processes in Strongly Coupled Organic-Semiconductor Microcavities. *Adv. Funct. Mater.* **2011**, *21* (19), 3691–3696.
- (21) Mazza, L.; Kéna-Cohen, S.; Michetti, P.; La Rocca, G. C. Microscopic Theory of Polariton Lasing via Vibronically Assisted Scattering. *Phys. Rev. B: Condens. Matter Mater. Phys.* **2013**, *88* (7), 075321.
- (22) Li, W.; Gao, M.; Zhang, X.; Liu, D.; Peng, L. M.; Xie, S. Microphotoluminescence Study of Exciton Polaritons Guided in ZnO Nanorods. *Appl. Phys. Lett.* **2009**, *95* (17), 173109.
- (23) Bœuf, F.; André, R.; Romestain, R.; Dang, L. S.; Péronne, E.; Lampin, J. F.; Hulin, D.; Alexandrou, A. Evidence of Polariton Stimulation in Semiconductor Microcavities. *Phys. Rev. B: Condens. Matter Mater. Phys.* **2000**, *62* (4), R2279–R2282.
- (24) Delteil, A.; Vasanelli, A.; Jouy, P.; Barate, D.; Moreno, J. C.; Teissier, R.; Baranov, A. N.; Sirtori, C. Optical Phonon Scattering of Cavity Polaritons in an Electroluminescent Device. *Phys. Rev. B: Condens. Matter Mater. Phys.* **2011**, *83* (8), 081404.
- (25) Müller, M.; Bleuse, J.; Andre, R.; Ulmer-Tuffigo, H. Observation of Bottleneck Effects on the Photoluminescence from Polaritons in II–VI Microcavities. *Phys. B* **1999**, *272*, 476–479.
- (26) Senellart, P.; Bloch, J. Nonlinear Emission of Microcavity Polaritons in the Low Density Regime. *Phys. Rev. Lett.* **1999**, *82* (6), 1233–1236.
- (27) Pau, S.; Cao, H.; Jacobson, J.; Björk, G.; Yamamoto, Y.; Imamoğlu, A. Observation of a Laserlike Transition in a Microcavity Exciton Polariton System. *Phys. Rev. A: At., Mol., Opt. Phys.* **1996**, *54* (3), R1789–R1792.
- (28) Imamoğlu, A.; Ram, R.; Pau, S.; Yamamoto, Y. Nonequilibrium Condensates and Lasers without Inversion: Exciton-Polariton Lasers. *Phys. Rev. A: At., Mol., Opt. Phys.* **1996**, *53* (6), 4250–4253.
- (29) Maragkou, M.; Grundy, A. J. D.; Ostatnick, T.; Lagoudakis, P. G. Longitudinal Optical Phonon Assisted Polariton Laser. *Appl. Phys. Lett.* **2010**, *97* (11), 111110.
- (30) Sebald, K.; Seyfried, M.; Klemmt, S.; Bley, S.; Rosenauer, A.; Hommel, D.; Kruse, C. Strong Coupling in Monolithic Microcavities with ZnSe Quantum Wells. *Appl. Phys. Lett.* **2012**, *100* (16), 161104.
- (31) Klemmt, S.; Durupt, E.; Datta, S.; Klein, T.; Baas, A.; Léger, Y.; Kruse, C.; Hommel, D.; Minguzzi, A.; Richard, M. Exciton-Polariton Gas as a Nonequilibrium Coolant. *Phys. Rev. Lett.* **2015**, *114* (18), 186403.
- (32) Zhang, J.; Li, D.; Chen, R.; Xiong, Q. Laser Cooling of a Semiconductor by 40 K. *Nature* **2013**, *493* (7433), 504–508.
- (33) Bloor, D.; Cross, G.; Sharma, P. K.; Elliott, J. A.; Rumbles, G. Frequency Up-Conversion in Fluid and Solid Solutions of the Oxazine Dye, Rhodamine B. *J. Chem. Soc., Faraday Trans.* **1993**, *89* (22), 4013–4015.
- (34) Clark, J. L.; Rumbles, G. Laser Cooling in the Condensed Phase by Frequency Up-Conversion. *Phys. Rev. Lett.* **1996**, *76* (12), 2037–2040.
- (35) Herrera, F.; Spano, F. C. Cavity-Controlled Chemistry in Molecular Ensembles. *Phys. Rev. Lett.* **2016**, *116* (23), 238301.
- (36) Spano, F. C. Optical Microcavities Enhance the Exciton Coherence Length and Eliminate Vibronic Coupling in J-Aggregates. *J. Chem. Phys.* **2015**, *142*, 184707.
- (37) Galego, J.; Garcia-vidal, F. J.; Feist, J. Cavity-Induced Modifications of Molecular Structure in the Strong-Coupling Regime. *Phys. Rev. X* **2015**, *5* (4), 041022.
- (38) Cwik, J. A.; Reja, S.; Littlewood, P. B.; Keeling, J. Polariton Condensation with Saturable Molecules Dressed by Vibrational Modes. *EPL* **2014**, *105*, 47009.

- (39) Zeb, M. A.; Kirton, P. G.; Keeling, J. Exact States and Spectra of Vibrationally Dressed Polaritons. *ACS Photonics* **2018**, *5* (1), 249–257.
- (40) Herrera, F.; Spano, F. C. Dark Vibronic Polaritons and the Spectroscopy of Organic Microcavities. *Phys. Rev. Lett.* **2017**, *118* (22), 223601.
- (41) Cortese, E.; Lagoudakis, P. G.; De Liberato, S. Collective Optomechanical Effects in Cavity Quantum Electrodynamics. *Phys. Rev. Lett.* **2017**, *119* (4), 043604.
- (42) Chen, Y.; Zhao, J.; Guo, H.; Xie, L. Geometry Relaxation-Induced Large Stokes Shift in Red-Emitting Borondipyrromethenes (BODIPY) and Applications in Fluorescent Thiol Probes. *J. Org. Chem.* **2012**, *77* (5), 2192–2206.
- (43) Musser, A. J.; Rajendran, S. K.; Georgiou, K.; Gai, L.; Grant, R. T.; Shen, Z.; Cavazzini, M.; Ruseckas, A.; Turnbull, G. A.; Samuel, I. D. W.; Clark, J.; Lidzey, D. G. Intermolecular States in Organic Dye Dispersions: Excimers vs. Aggregates. *J. Mater. Chem. C* **2017**, *5* (33), 8380–8389.
- (44) Grant, R. T.; Michetti, P.; Musser, A. J.; Gregoire, P.; Virgili, T.; Vella, E.; Cavazzini, M.; Georgiou, K.; Galeotti, F.; Clark, C.; Clark, J.; Silva, C.; Lidzey, D. G. Efficient Radiative Pumping of Polaritons in a Strongly Coupled Microcavity by a Fluorescent Molecular Dye. *Adv. Opt. Mater.* **2016**, *4* (10), 1615–1623.
- (45) Savona, V.; Andreani, L. C.; Schwendimann, P.; Quattropani, A. Quantum Well Excitons in Semiconductor Microcavities: Unified Treatment of Weak and Strong Coupling Regimes. *Solid State Commun.* **1995**, *93* (9), 733–739.
- (46) Shalabney, A.; George, J.; Hutchison, J.; Pupillo, G.; Genet, C.; Ebbesen, T. W. Coherent Coupling of Molecular Resonators with a Microcavity Mode. *Nat. Commun.* **2015**, *6*, 5981.
- (47) George, J.; Shalabney, A.; Hutchison, J. A.; Genet, C.; Ebbesen, T. W. Liquid-Phase Vibrational Strong Coupling. *J. Phys. Chem. Lett.* **2015**, *6* (6), 1027–1031.
- (48) Long, J. P.; Simpkins, B. S. Coherent Coupling between a Molecular Vibration and Fabry-Perot Optical Cavity to Give Hybridized States in the Strong Coupling Limit. *ACS Photonics* **2015**, *2* (1), 130–136.
- (49) del Pino, J.; Feist, J.; Garcia-Vidal, F. J. Quantum Theory of Collective Strong Coupling of Molecular Vibrations with a Microcavity Mode. *New J. Phys.* **2015**, *17*, 053040.

## 6.4. Supporting Information

### Supporting Information

#### Generation of Anti-Stokes Fluorescence in a Strongly Coupled Organic Semiconductor Microcavity

Kyriacos Georgiou<sup>1</sup>, Rahul Jayaprakash<sup>1</sup>, Alexis Askitopoulos<sup>2,3</sup>, David M. Coles<sup>1</sup>, Pavlos G. Lagoudakis<sup>2,3\*</sup> and David G. Lidzey<sup>1\*</sup>

<sup>1</sup>Department of Physics and Astronomy, The University of Sheffield, Hicks Building, Hounsfield Road, Sheffield, S3 7RH, United Kingdom.

<sup>2</sup>Department of Physics and Astronomy, University of Southampton, Southampton, SO17 1BJ, United Kingdom.

<sup>3</sup>Skolkovo Institute of Science and Technology, Moscow 143026, Russia.

\*Authors for correspondence: [d.g.lidzey@sheffield.ac.uk](mailto:d.g.lidzey@sheffield.ac.uk) and [pavlos.lagoudakis@soton.ac.uk](mailto:pavlos.lagoudakis@soton.ac.uk)

Number of pages: 7

Number of figures: 6

### Three-level coupled oscillator model

A three-level coupled oscillator model was used to describe the photon-exciton coupling. Eq.S1 was diagonalised and solved to extract the LPB, MPB and UPB energy. The eigenvectors calculated from the Eq.S1 gave the Hopfield coefficients (Figure S1) for the mixing fractions of photon and the two excitons for the three polariton branches.

$$\begin{pmatrix} E_C(\theta) & \hbar\Omega_{0-0}/2 & \hbar\Omega_{0-1}/2 \\ \hbar\Omega_{0-0}/2 & E_{X_{0-0}} & 0 \\ \hbar\Omega_{0-1}/2 & 0 & E_{X_{0-1}} \end{pmatrix} \begin{pmatrix} \alpha_C \\ \alpha_{X_{0-0}} \\ \alpha_{X_{0-1}} \end{pmatrix} = E_{pol}(\theta) \begin{pmatrix} \alpha_C \\ \alpha_{X_{0-0}} \\ \alpha_{X_{0-1}} \end{pmatrix} \quad (\text{Eq.S1})$$

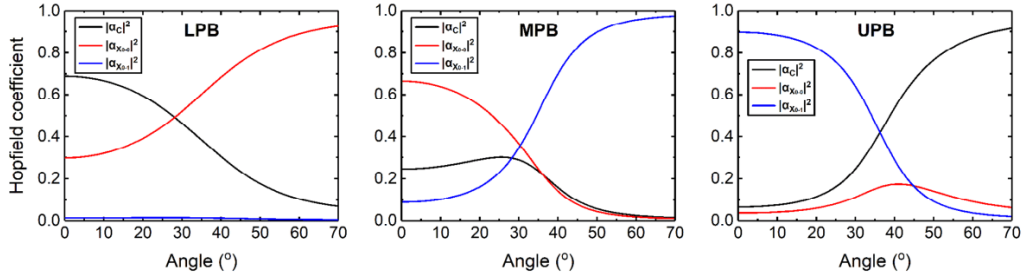


**Figure S1.** Hopfield coefficients for the three polariton branches extracted from a three-level coupled oscillator model. LPB, MPB and UPB: Lower, Middle and Upper polariton branch.

## Optical characterisation

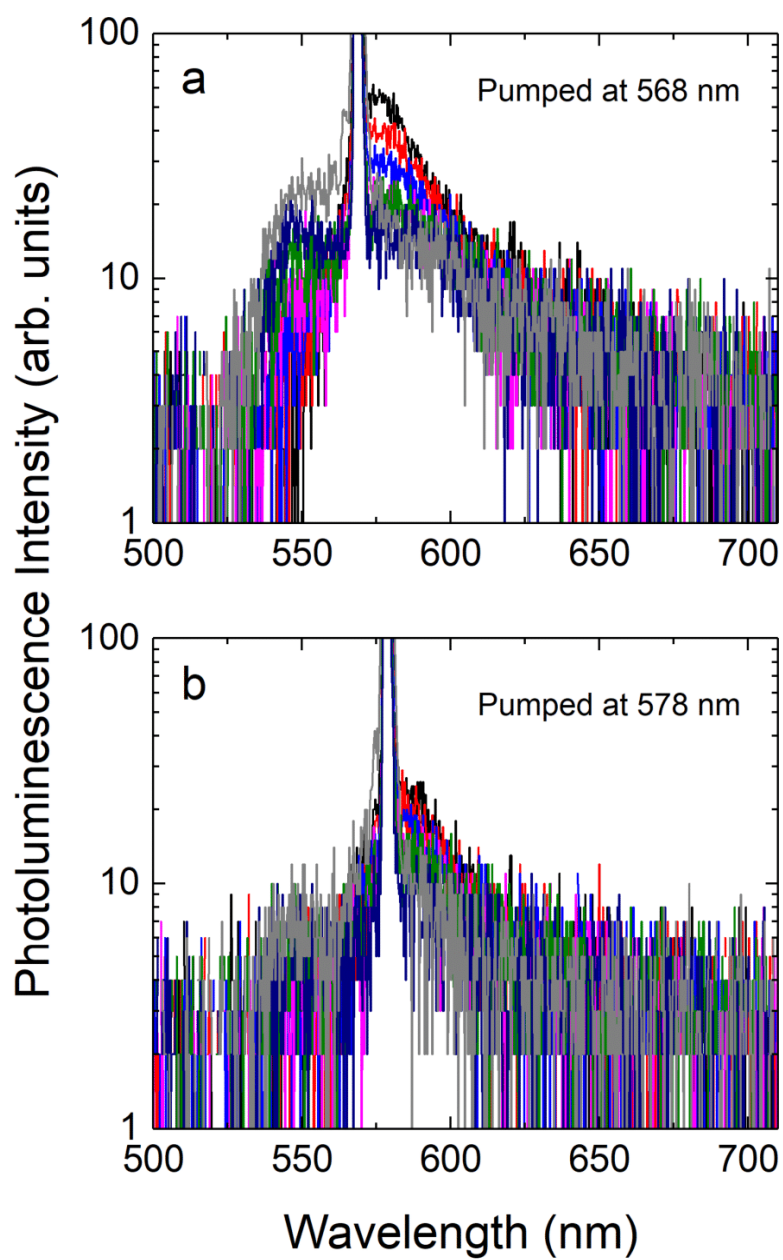


**Figure S2.** Temperature dependent frequency up-conversion of a BODIPY-Br / PS non-cavity thin film excited at (a) 568 nm and (b) 578 nm.

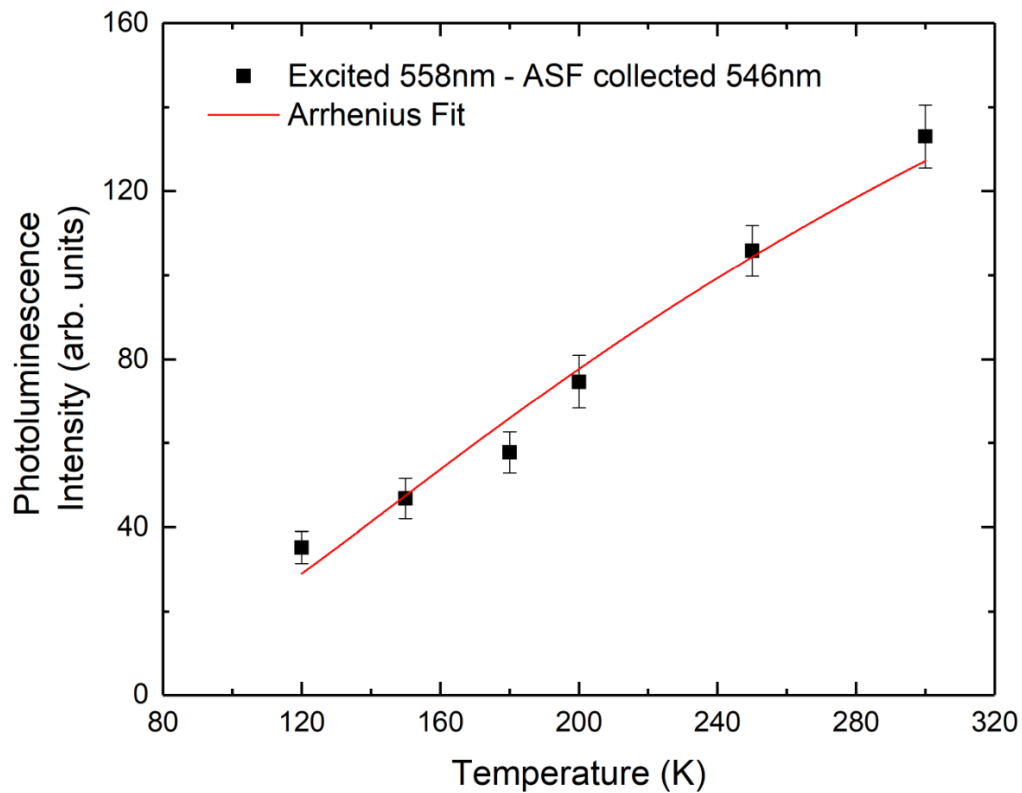


**Figure S3.** Temperature dependence of ASF intensity of a non-cavity BODIPY-Br / PS thin film when excited at 558 nm and collected at 546 nm along with an Arrhenius fit with an activation energy of around 23 meV.

In Figure S4, we demonstrate that both the intensity of ASF and the total emission intensity is directly proportional to the extinction coefficient of the BODIPY-Br/PS film at the excitation wavelength.

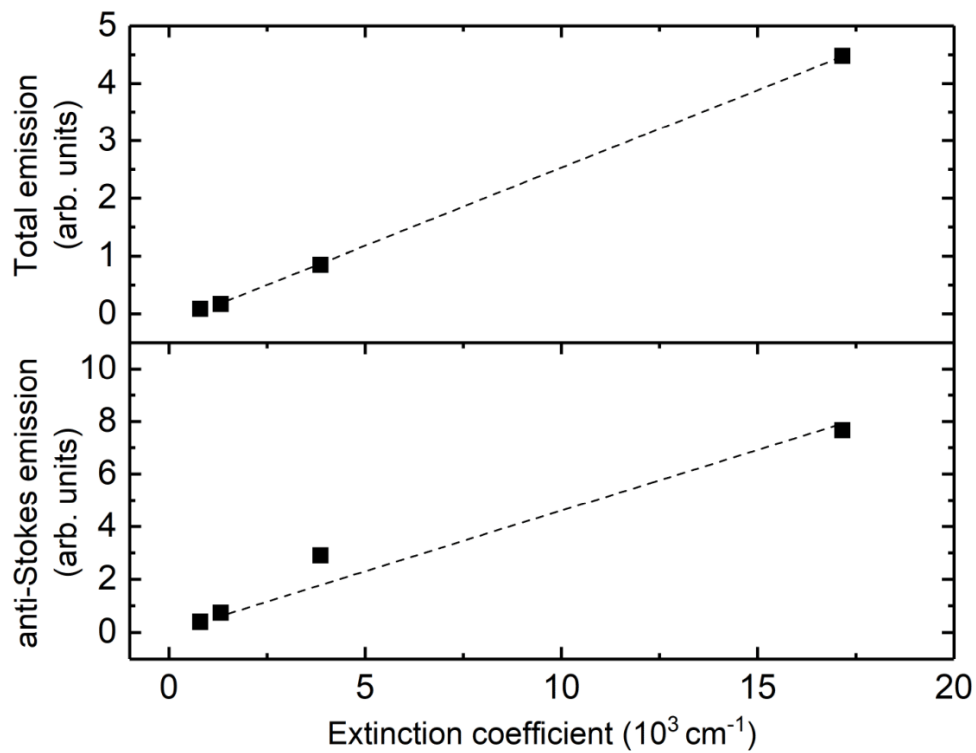


**Figure S4.** Integrated intensity of the total PL (top) and the ASF (bottom) with extinction coefficient of the BODIPY-Br / PS film at the wavelength of excitation.

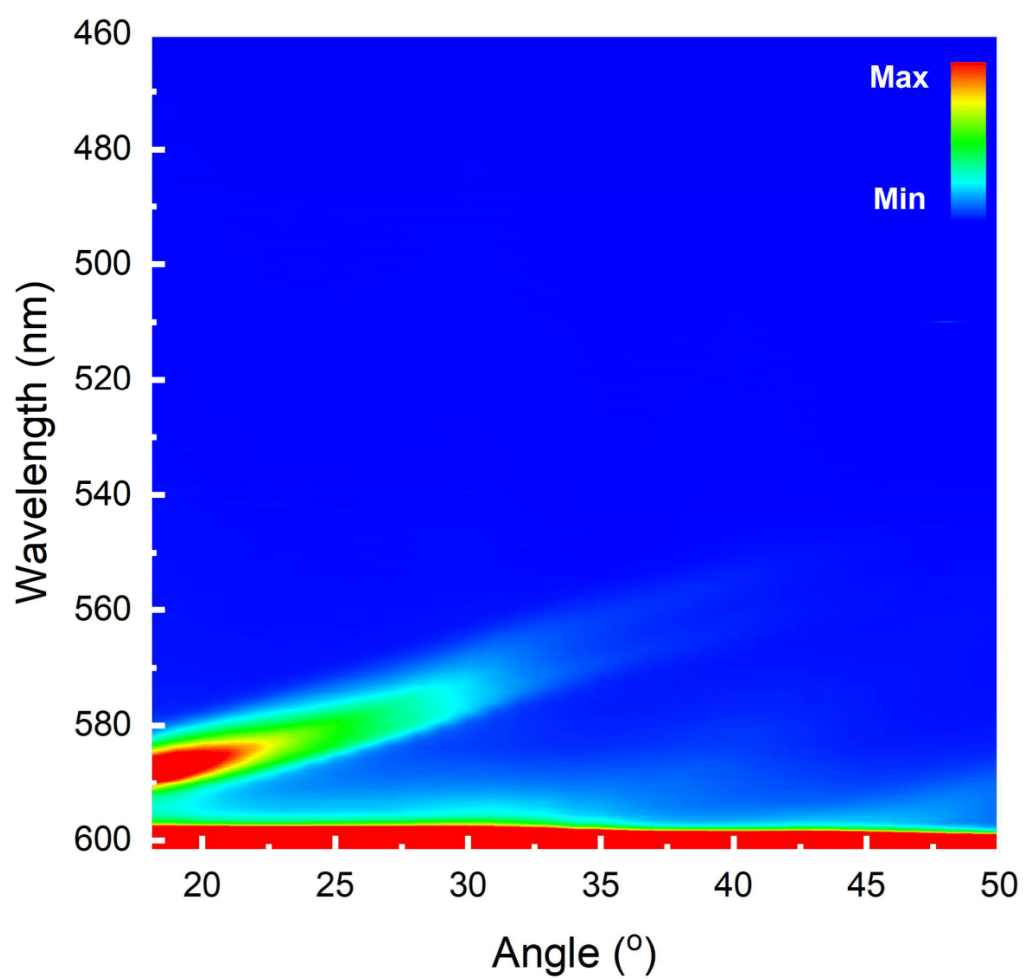


**Figure S5.** Temperature dependent photoluminescence of the lower polariton branch following resonant excitation at 600 nm showing the anti-Stokes fluorescence vs emission angle.

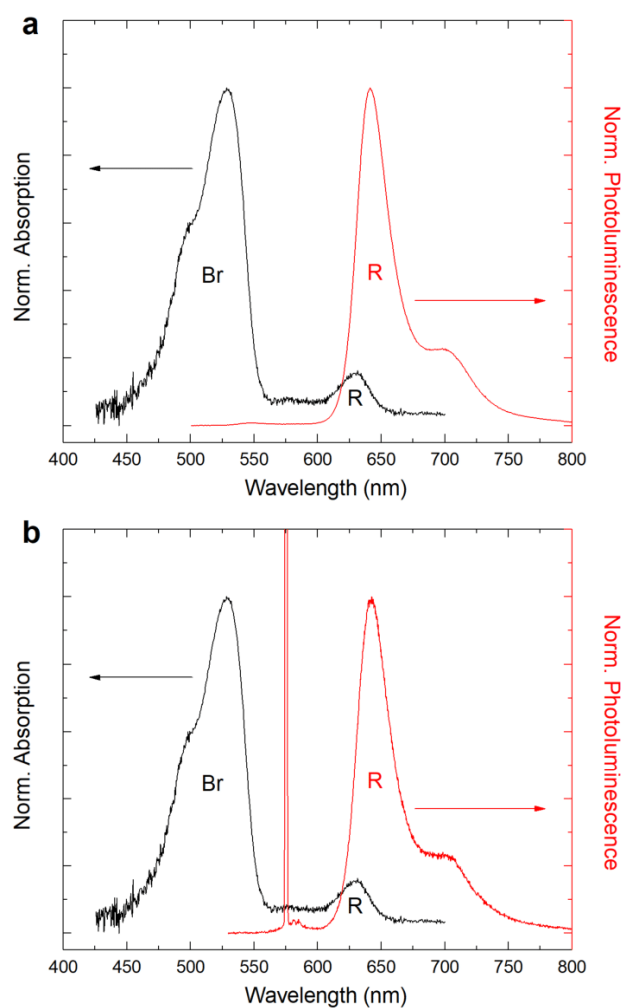


**Figure S6.** Absorption and photoluminescence emission of a film containing a blend between BODIPY-Br (donor) and BODIPY-R (acceptor) in PS at 20% / 0.75% concentration by mass. Photoluminescence emission is recorded when the film is excited (a) at 473 nm and (b) at 575 nm. The photoluminescence measurements indicate almost complete energy transfer (>99%) from the donor to the acceptor dye by dipole-dipole coupling.

## Chapter 7. Conclusions and future work

### 7.1. Conclusions

Organic semiconductors have been established as good material systems for use as the active layer in strongly coupled microcavities. This is due to their high binding energy, which allows the realisation of strong coupling at room temperature and also their large oscillator strength allowing for Rabi splitting energies on the order of 0.1-1 eV. Additionally, the ease with which these materials can be processed and deposited in microcavity structures is an advantage compared to inorganic semiconductors, whose growth requires difficult, expensive and time-consuming techniques. In this thesis, we have explored the fabrication and room-temperature optical characterisation of strongly coupled microcavities containing different fluorescent molecular dyes dispersed in a polymer matrix at relatively low concentrations.

In Chapter 3, we introduced a series of BODIPY fluorescent molecular dyes. The photophysical properties of these different BODIPY derivatives were investigated using different spectroscopic experiments. We concluded that BODIPY dyes are good candidates to use as the active material in strongly coupled microcavities. Next, we fabricated a series of high Q-factor microcavities and showed using white-light reflectivity measurements that all the cavities can enter the strong coupling regime at room temperature. Following non-resonant laser excitation, room-temperature photoluminescence was emitted from such structures and from its analysis, the polariton population distribution along the lower branch was deduced. A simple model was then used to describe the population distribution considering the formation of an exciton reservoir of states that remain weakly coupled to the confined optical mode.

In addition to the study of microcavities operating in the linear regime, non-linear effects from a strongly coupled microcavity containing a fluorescent BODIPY dye were discussed in Chapter 4. This structure utilised two distributed Bragg reflectors, which resulted in a high Q-factor microcavity. White light reflectivity and low laser excitation density measurements showed that the cavity operated in the strong coupling regime at room temperature. Following high-density laser excitation, the occupation of the bottom of the lower polariton branch exceeded unity and a phase

transition occurred. A room-temperature polariton condensate in the yellow region of the spectrum was realised. Power dependent measurements showed that above an excitation threshold there was a non-linear increase of the luminescence intensity accompanied with a drop in the linewidth of emission. A continuous energy blueshift of the emission was also observed with interferometry measurements confirming a high degree of spatial coherence.

Chapter 5 described the hybridisation of the excitonic transitions of two BODIPY dyes by coupling them to the same confined optical mode of a metallic mirror microcavity. Two structural microcavity configurations were used: (1) A microcavity which incorporated a spacer layer to separate the two molecular dye layers, and (2) a microcavity which contained a film of the same dye molecules that had been blended together in a polymer matrix. The first configuration allowed for long-range energy transfer to take place while in the latter, direct dipole-dipole coupling was achieved which led to short-range Förster resonance energy transfer. Using different spectroscopic experiments, we showed that the emission patterns from microcavities containing the spacer layer were depended on the exciton-photon detuning. In cavities containing the blend, fluorescence was emitted only from the lower polariton branch indicating almost complete energy transfer from the donor to the acceptor molecules within the exciton reservoir.

In Chapter 6, polariton anti-Stokes fluorescence in a BODIPY-filled metallic mirror microcavity was demonstrated. Using temperature dependent measurements, we observed a reduction in the intensity of the anti-Stokes fluorescence at low temperatures indicating a thermally activated process. The polariton emission dynamics were investigated using a streak camera and found to be very similar to those following non-resonant excitation. Therefore, we concluded that polaritons that were injected at the bottom of the lower polariton branch interacted with an exciton reservoir before scattering back to ‘hot’ polariton states. We have proposed a picture to describe this process: Polaritons are generated at the bottom of the lower polariton branch when the microcavity is resonantly excited. Decay of these photo-generated polaritons pumps molecules that exist in a vibrationally excited ground-state forming an exciton reservoir. This reservoir is then able to optically pump and populate polariton states that have a higher energy than that of the initial laser excitation, leading to anti-Stokes fluorescence. The angle-integrated population of cavity-

polaritons responsible for anti-Stokes fluorescence was found to be 3 times larger than that of ‘hot’ excitons in a non-cavity film. This enhancement of anti-Stokes fluorescence in a microcavity resulted from the fact that Stokes emission was suppressed as its energy was below the cut-off frequency of the cavity. Therefore, it was suggested that anti-Stokes polariton fluorescence could be used to explore laser cooling in solid-state systems.

## 7.2. Future work

In previous studies, polariton condensation has been achieved using pure films of organic fluorophores placed between two highly reflective mirrors. Here, we demonstrated that diluted molecular dyes can also undergo polariton condensation. This opens the possibility to use a range of molecular materials at relatively low concentrations that emit light at different wavelengths of the visible and near-IR spectrum. For example, we have very recently observed laser emission from the lower energy state of a strongly coupled microcavity containing a perylene-based molecule (Lumogen-F orange) dispersed in a polymer matrix. This material is more photostable compared to BODIPY dyes as was shown in Chapter 3. It would be interesting to create different patterns in such structures that will allow confinement of light to be achieved in more than one dimension. This might reduce condensation thresholds as well as allow different quantized optical modes to interact with molecular excitations.

In the linear regime, it would be interesting to study multilayer microcavities, where the separation distance between the strongly coupled dyes is tuned. This will allow us to determine at which extent long-range energy transfer can be achieved in such structures and whether the separation distance can affect the efficiency of this process. Apart from traditional monolithic microcavities, a different approach to achieving this is by using an open cavity configuration where each of the two molecular materials is deposited on one mirror. Then air between the mirrors will act as the spacer between the two molecular materials. In addition, using monolithic microcavities, by increasing the thickness of the spacer layer while reducing that of the dye layers (i.e. a transition from the strong to the weak coupling regime), may also allow us to identify how the coupling strength between excitons and photons could affect the long-range energy transfer.

In the future, it would be very interesting to explore anti-Stokes fluorescence in microcavities containing different types of organic semiconductors. Examples would include, cavities filled with J-aggregates that are characterized by a single sharp and narrow transition, or cavities containing molecules like Lumogen-F Orange or anthracene, which have a strong vibronic progression. Particular focus should be given to materials with very high PLQY which may allow us to demonstrate laser cooling of organic microcavities. The advantage here is that the polariton near-parabolic dispersion favours the population of polariton states associated with ASF emission rather than states associated with Stokes emission. The latter exist below the cut off energy of the cavity where the density of states is near zero. We are already planning to perform such experiments using a controlled environment and probing the temperature of the sample using different techniques, i.e. thermal camera with 20 mK resolution.